DETERMINATION OF THE BENDING TWISTING COUPLING POTENTIAL OF COMPOSITE MATERIALS VIA DIGITAL IMAGE CORRELATION AND ITS IMPLEMENTATION IN WIND TURBINE BLADES

A THESIS SUBMITTED TO
THE GRADUATE SCHOOL OF NATURAL AND APPLIED SCIENCES
OF
MIDDLE EAST TECHNICAL UNIVERSITY

BY

ÖZGÜN ŞENER

IN PARTIAL FULFILLMENT OF THE REQUIREMENTS
FOR
THE DEGREE OF MASTER OF SCIENCE
IN
AEROSPACE ENGINEERING

SEPTEMBER 2017

Approval of the thesis:

DETERMINATION OF THE BENDING TWISTING COUPLING POTENTIAL OF COMPOSITE MATERIALS VIA DIGITAL IMAGE CORRELATION AND ITS IMPLEMENTATION IN WIND TURBINE BLADES

submitted by **ÖZGÜN ŞENER** in partial fulfillment of the requirements for the degree of **Master of Science in Aerospace Engineering Department, Middle East Technical University** by,

Prof. Dr. Gülbin Dural Ünver
Dean, Graduate School of **Natural and Applied Sciences** _____

Prof. Dr. Ozan Tekinalp
Head of Department, **Aerospace Engineering** _____

Prof. Dr. Altan Kayran
Supervisor, **Aerospace Engineering Dept., METU** _____

Examining Committee Members:

Assoc. Prof. Dr. Demirkan Çöker
Aerospace Engineering Dept., METU _____

Prof. Dr. Altan Kayran
Aerospace Engineering Dept., METU _____

Assoc. Prof. Dr. Ercan Gürses
Aerospace Engineering Dept., METU _____

Prof. Dr. Ozan Tekinalp
Aerospace Engineering Dept., METU _____

Asst. Prof. Dr. Mustafa Kaya
Aeronautical Engineering Dept.,
Ankara Yıldırım Beyazıt University _____

Date: 08.09.2017

I hereby declare that all information in this document has been obtained and presented in accordance with academic rules and ethical conduct. I also declare that, as required by these rules and conduct, I have fully cited and referenced all material and results that are not original to this work.

Name, Last name : ÖZGÜN ŞENER

Signature :

ABSTRACT

DETERMINATION OF THE BENDING TWISTING COUPLING POTENTIAL OF COMPOSITE MATERIALS VIA DIGITAL IMAGE CORRELATION AND ITS IMPLEMENTATION IN WIND TURBINE BLADES

Şener, Özgün
M.S., Department of Aerospace Engineering
Supervisor : Prof. Dr. Altan Kayran

September 2017, 151 pages

In this thesis study, the main objective is to investigate the effect of bending-twisting coupling in composite wind turbine blades on the load alleviation, power generation and structural performance of the wind turbine system. For this purpose, experimental and numerical study is initially conducted to determine the bend-twist coupling potentials of composite materials. Bending-twisting behavior of composite materials are determined through a comparative study via the Digital Image Correlation (DIC) system and the finite element analysis, and the outcome of the numerical and experimental study is utilized to form a basis on the selection of material and fiber angle configuration for wind turbine blade designs with the purpose of load alleviation in the whole wind turbine system. Experimental and numerical study of the bending twisting coupling behavior of composite materials is performed on composite plates and box beams which simulate the flange region in wind turbine blades in much smaller scale. In order to validate the results of the finite element analyses, orthotropic properties of E-Glass and Carbon materials are determined through following several international tensile test procedures via DIC system and strain gage application. Bend-twist coupling potentials determined by the DIC system and the finite element analyses

are compared, and a reliable database for the effect of bend-twist coupling due to different materials and different fiber angle orientations is generated. Based on this study, material selection and off-axis fiber angle range to be utilized in the bend-twist coupled turbine blade designs are determined. Wind turbine models with designed bend-twist coupled blades are set up in a multi-body dynamic code with the aim of investigating and comparing the effect of bend-twist coupling on the load reduction in subcomponents of turbine system and on the power generation and structural performance of the wind turbine system. The effect of bend-twist coupling due to different composite materials and fiber angle orientations in turbine blades is examined under realistic working scenarios with six different turbulent wind profiles. In overall, results show that the bending twisting coupling effect in the wind turbine blades contribute to the reduction in loads at the critical points in the whole turbine system without significant disadvantages.

Keywords: Bend-twist coupling, Digital image correlation, Wind turbine, Composite blades, Load alleviation

ÖZ

KOMPOZİT MALZEMELERDE EĞİLME BURULMA ETKİLEŞİMİNİN SAYISAL GÖRÜNTÜ BAĞINTI İLE BELİRLENMESİ VE RÜZGAR TÜRBİN KANATLARINDA UYGULANMASI

Şener, Özgün
Yüksek Lisans, Havacılık ve Uzay Mühendisliği Bölümü
Tez Yöneticisi : Prof. Dr. Altan Kayran

Eylül 2017, 151 sayfa

Bu tez çalışmasında, rüzgar türbin kanatlarındaki eğilme-burulma etkileşiminin rüzgar türbin sisteminde yük azaltımı, güç üretimi ve yapısal performansa olan etkisinin incelenmesi hedeflenmiştir. Bu amaçla, kompozit malzemelerdeki eğilme burulma etkileşimi potansiyellerinin Sayısal Görüntü Bağıntı (SGB) ve sonlu elemanlar modelleriyle karşılaştırmalı analizleri ile belirlenmesi ve elde edilen nümerik ve deneysel çalışmanın rüzgar türbin kanatlarında malzeme seçimi ve fiber açı konfigürasyonlarının bütün rüzgar türbin sisteminde yük azalımı sağlanması amacıyla güvenilir bir veri tabanı oluşturulması hedeflenmiştir. Nümerik ve deneysel çalışmalarda, kompozit malzemelerdeki eğilme burulma etkisi, rüzgar türbin kanatlarındaki flanş bölgesine benzerlik gösteren kompozit plaka ve kutu kirişler kullanılarak incelenmiştir. Sonlu elemanlar analizlerinde doğrulanmış sonuçlar elde etme amacıyla, cam-elyaf ve karbon-elyaf ortotropik malzeme özellikleri SGB sistemi ve gerinim ölçerlerin kullanılması ile uluslararası test prosedürleri takip edilerek saptanmıştır. SGB sistemi ve sonlu elemanlar modeli kullanılarak elde edilen sonuçlar kıyaslanmış ve malzeme ve fiber açı konfigürasyonu seçiminin eğilme burulma etkileşimleri üzerindeki etkisini yansıtan bir veri tabanı yaratılmıştır. Bu çalışma neticesinde, tasarlanan eğilme burulma etkileşimli kanatlarda kullanılan malzeme ve

fiber açı aralığı belirlenmiştir. Rüzgar türbin elemanlarında eğilme burulma etkileşimi etkisi nedeniyle meydana gelen yük azalımı, güç üretimi ve yapısal performansı incelemek için, tasarlanan eğilme burulma etkileşimli kanatlara sahip rüzgar türbin modelleri çok kütleli dinamik kodda yaratılmıştır. Farklı malzeme ve fibar açı seçimlerinden ötürü oluşan eğilme burulma etkileşimi, rüzgar türbininin gerçek çalışma koşullarında, 6 farklı türbülanslı rüzgar altında incelenmiştir. Bu çalışma sonucunda, eksendışı yerleştirilen katmanlar ile kanatlarda oluşturulan eğilme burulma etkileşiminin rüzgar türbininin kritik noktalarında yük azalımına kayda değer aleyhte durum oluşturmadan katkı yaptığı saptanmıştır.

Anahtar Kelimeler: Eğilme burulma etkileşimi, Sayısal görüntü bağıntı, Rüzgar türbini, Kompozit kanat, Yük azalımı

To My Family

ACKNOWLEDGMENTS

First and foremost, I would like to thank my supervisor Prof. Dr. Altan Kayran for his constant support, guidance, and patience for the last three years. With his lead and cooperation, I have been able to improve my academic and engineering point of view besides with the humanitarian values. A lot of people helped me through this thesis without whom this work would have never been completed. My colleagues Oğuz Atalay and Yunus Tansu Aksoy helped me a lot through experiments and analyses.

I would also like to thank my office mates from METUWind: Touraj Farsadi, Gökhan Gürün and Başak Zeka for their companionship and understanding throughout the time we have shared together. Moreover, I would also like to acknowledge Çağdaş Sarıcı and Sadık Gökhan Keçeci, who have motivated me with their most valuable friendship.

I would like to thank all of my professors from Aerospace Engineering Department in METU. Professor Demirkan Çöker assisted me in this work that I truly appreciate.

Lastly but most importantly, I want to express my gratitude for the dearest people who made me who I am. I am deeply indebted to my beloved mother, father and my best friend for life Ilgım Doğan for their continuous support and positive attitude in my time of life.

TABLE OF CONTENTS

LIST OF TABLES

TABLES

LIST OF FIGURES

FIGURES

CHAPTER 1

INTRODUCTION

1.1 Renewable Energy and Wind Energy

Conventional energy sources derived from fossils, oils and coals have proven that they are highly effective over the centuries. They have been used as main energy source since the Industrial Revolution changing every aspect of the modern world. Nevertheless, non-renewable energy sources are limited and harmful to the environment. Increment in global warming and the climate change are expected to occur due to usage of fossil fuels with the today's consumption rate [1]. As the dependency of non-renewable energy increases, the cost of the energy grows higher. The governments all over the world have started to invest on renewable energy in order to deprive the dependency on these sources.

Renewable energies are any sources that are naturally regenerated from the sun (such as thermal, photochemical, and photoelectric), indirectly from the sun (such as wind, hydropower, and photosynthetic energy stored in biomass), or from other natural movements and mechanisms of the environment (such as geothermal and tidal energy) [2]. Renewable energy sources started to draw attention from governments and officials in the last decades as an alternative mainly due to increasing cost, gas emission and pollution, and depletion rate of non-renewable energy sources. Thanks to the developments in technology, there are vast amount of ways to extract energy from renewable energy sources. Figure 1.1 shows the different forms of renewable energy sources and technologies.

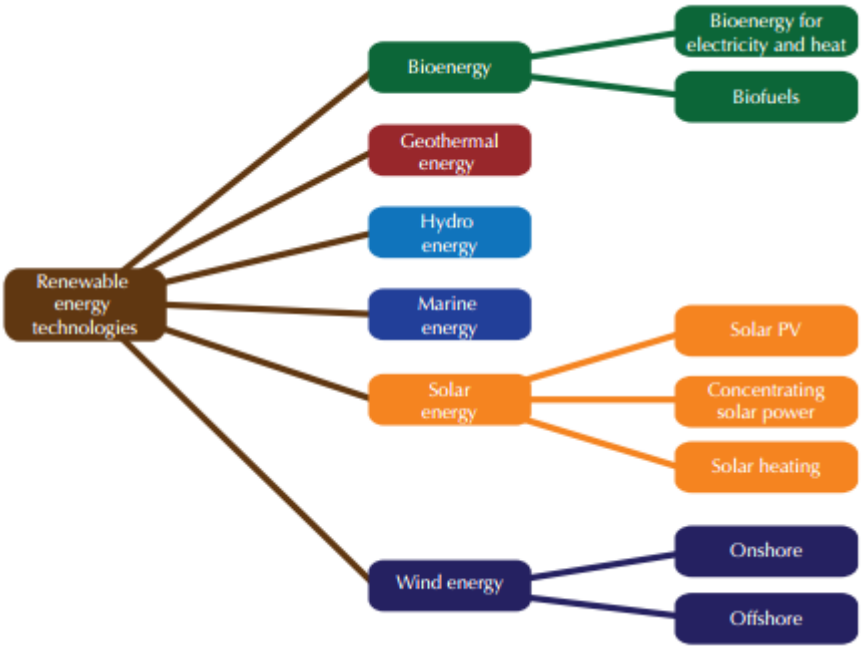

Figure 1.1 Types of renewable energy sources and technologies [3]

The world's energy resources are more than sufficient to continue our lives. In fact, Figure 1.2 shows that available renewable energy sources are more than 3000 times the today's global energy consumption.

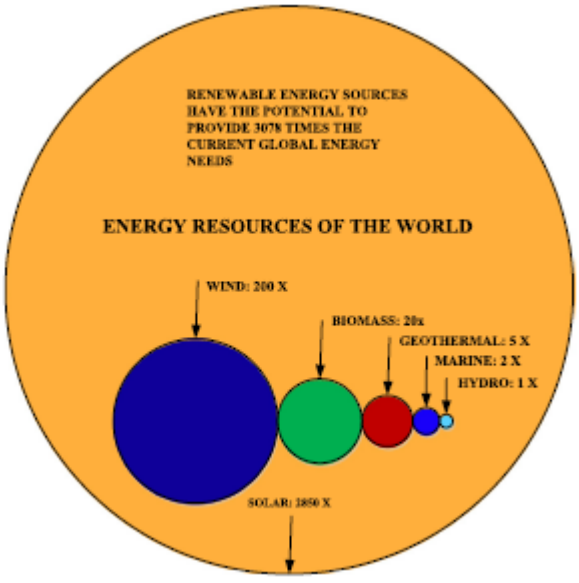

Figure 1.2 Energy resources of the world [4]

The use of renewable energy continually increases and wind power holds great share among the above-mentioned resources. Today, more than two hundred thousand wind turbines are active and producing electricity. In 2010, the cumulative installed wind capacity was slightly above 17,000 MW whereas, in 2015, it has reached 432,000 MW, more than 25 times increase in capacity in 15-year time period [5]. This statistics shows the importance given to wind energy. As an example, Denmark produces 40% of its electricity from wind only. In USA, more than 20% of the electricity is extracted from wind. With the developments in the wind turbine technology, greater achievements in the wind turbine industry are expected.

1.2 Wind Turbines

Wind turbines are machines that convert wind's kinetic energy to rotary mechanical energy, resulting in the production of electricity. The first wind turbines were windmills that were used for the purpose of grinding in ancient Persia around 900 A.D. At the end of the 19^{th} century, people started to generate electricity from the wind turbines and today, 4% of the total electricity in the world is generated from wind turbines. Small wind turbines are used to recharge batteries and illuminate lamps where the larger ones in the industry are used to supply electricity.

There are two types of wind turbines which are commonly used, vertical axis wind turbine (VAWT) whose rotor shaft is arranged vertically, and horizontal axis wind turbine (HAWT) whose rotor shaft is pointing the direction of the wind, the latter being more common. Figure 1.3 shows schematic of horizontal and vertical axis wind turbines.

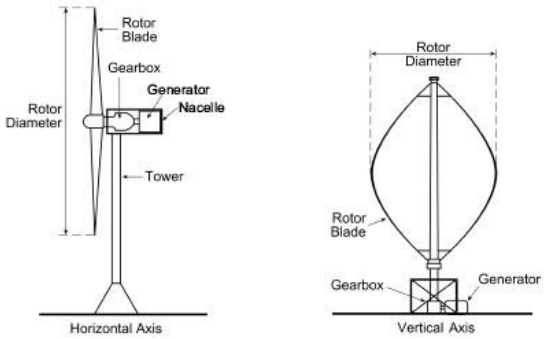

Figure 1.3 Horizontal and vertical axis wind turbines [6]

Figure 1.4 shows the main components of a wind turbine. Basically, due to wind, the aerodynamic torque causes the blades to rotate which in turn causes the main shaft to spin. The gearbox increases the rotational speed of the shaft about 35 to 110 times, which is the required rotational speed for most generators to produce electricity. The produced electricity is either saved by batteries or transferred to houses or companies to be used readily.

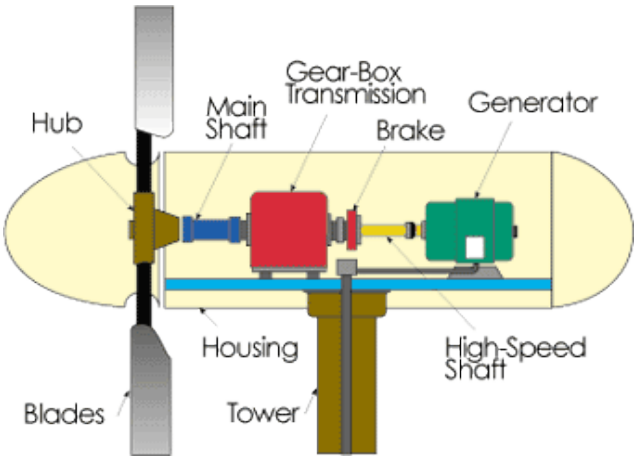

Figure 1.4 Main components of a wind turbine [7]

Whilst both configurations have certain advantages, HAWTs dominate the industry today as they can produce more electricity for the given amount of wind. VAWTs are generally used in small scales to supply power to small appliances and they are more efficient than HAWTs in turbulent winds. With the variable blade pitch, HAWTs' blades can reach the optimum angle of attack for the turbine to produce the maximum

power available. Another reason why HAWTs are preferred is that with the yaw control, the blades are always perpendicular to the wind and the HAWT receives the wind for the whole complete rotation of the blades. Today, more and more research is done on HAWTs to increase their life, efficiency, and power output. In this thesis, the term *wind turbine* is used for horizontal axis wind turbine.

1.3 Literature Survey

In the wind turbine industry, the energy required from wind turbines has risen due to the increased demand for renewable energy. Blades are one of the main components responsible for the power produced. In order to obtain higher power from the turbines, the necessity of optimum control of the pitch angle and the increase in the length of the blades have boosted. The newly designed wind turbine blades have already reached the 100 meter border. Due to the increase in the length, the weight of the blades increase. Moreover, active control mechanism for the pitch angle requires feedback system and mechanical parts to be installed on the blades which result in additional cost and weight. Longer blades necessitate better optimized blade structures which bring about challenges to the design process to develop innovative design solutions.

Higher energy extraction from wind turbine systems requires larger turbines, with blades in the border of 100 m, and associated optimized structural and mechanical components to accomplish improved stiffness, increased fatigue life, and reliability. To attain these goals, loads that occur due to the aeroelastic effects on the wind turbine blades must be reduced. This can also be achieved passively by utilizing anisotropy of composite materials. Due to the anisotropic behavior of composite materials, aeroelastic tailoring of the rotor blades as a passive control mechanism can be succeeded. Induced twist due to bending on the blades which occurs as a result of anisotropic behavior of composite materials as a passive control mechanism may reduce the loads in the whole wind turbine system.

In wind turbine systems, internal load cycles may exceed 10^8 and reduction of fatigue loads incurred on structural and mechanical components is of utmost importance to

keep wind turbine systems operational for longer periods. Fatigue damage equivalent load (*DEL*) is a sign of the degradation of the elements of the sub-structures of the wind turbine system due to material fatigue incurred under cyclic loading and reduction in the damage equivalent loads implies increased fatigue life of the structural elements.

The use of bend-twist coupling in composite blades is considered as an alternative to the active load control strategies. The proposition of exploiting bending-twisting coupling as a passive load control mechanism in wind turbine systems was first made by Karaolis [8]. De Goeij et al. suggested utilizing a single-box or double-box spar scheme in order to overcome strain incompatibilities even though the induced twist due to bending reduced because of increased stiffness [9]. Kooijman [10] recommended utilizing off-axis plies at the outer blade for enhancement in energy yield for pitch-controlled blades. The work of Lobitz and Veers [11] showed that the fatigue damage load decreases with different wind speeds without noticeable reduction in average power for variable speed pitch controlled rotors. With this work, they were able to explore the effect of wind speed, control strategies (stall or pitch control), and turbulence on the damage load of wind turbine systems with bend-twist coupled blades. Nevertheless, there were yet to be explored about the potential of bend-twist coupling in terms of use of materials. Locke and Valencia [12] investigated the usage of carbon-epoxy material in the main spar caps of the wind turbine blades. They demonstrated that with the use of off-axis carbon plies in the spar caps of an experimental 9.2 m long blade made by TPI Composites, similar structural behavior as that of baseline E-Glass blades can be obtained. Moreover, they found that blades with carbon plies in the spar caps are more advantageous than the ones with E-Glass in terms of weight. In this study, comparisons are also made with the base E-Glass blade in terms of bending and buckling loads as well as strain distribution. Lin and Lai [13] performed a similar study. They investigated a 5 meter long blade model to observe the effect of bend-twist coupling. They found that hybrid carbon and glass fiber usage provided better bend-twist coupling properties than full carbon and full glass fiber arrangements. Moreover, they suggested to blade developers that off-axis

fibers should be adapted in such a way that they adapt to operating conditions to acquire better performance.

In the work of Zhou et al. [14], blade of NREL's 5MW wind turbine system [15] is used to show that bend-twist coupling characteristics of the blade changes tremendously by using different composite material with different fiber orientations by finite element analysis. Luczak et al. investigated the deformation behavior of bend-twist coupled wind turbine blades [16]. In their study, they used a modified version of Vestas wind turbine blade which has off-axis plies on the upper and lower skin to compare static and dynamic characteristics of the blade with the finite element results. Capellaro investigated the change in the internal loads due to bend-twist coupling [17]. In his work, he showed that as a result of bend-twist coupling, reduction in the fatigue damage equivalent blade root moments could be achieved. A similar study is conducted by Ashwill [18]. He concluded that utilizing off-axis carbon plies in the blade skin induces twist and alleviates loads. Gözcü inspected the bend-twist coupled superelement blades on the load alleviation at several monitor points on a wind turbine system [19]. Fedorov and Berggreen [20] investigated the bend-twist coupling potential along with the change in bending stiffness with the usage of GFRP and CFRP materials used in blade spar flanges of bend-twist coupled blades. For this purpose, they used a wind turbine blade section given by Vestas Wind Systems A/S. They concluded that, with the usage of CFRP material instead of GFRP in the spar caps, it is possible to achieve higher bend-twist coupling potential whilst keeping bending stiffness the same as the baseline blade configuration. A similar outcome is produced from the work of Aziz et al. [21]. In their work, they showed that, in normal wind conditions, by using CFRP off-axis plies in the spar cap plies, a greater twist angle is achieved with the overall weight advantage in the hub. Furthermore, in the case of gust wind, carbon-hybrid blade has greater twist which in turn, prevents blade to go through aerodynamic stall. Fedorov et al. investigated and compared the structural behavior of wind turbine blades due to bend-twist coupling through experiments and finite element analyses [22]. They came up with the result that the difference of induced twist due to bending between experimental and finite element results is less than 9%.

1.4 Scope of the Thesis

Because of the multidisciplinary nature of wind energy technology, it comprises many topics in the sub-system level which are open to research and development. Due to the fact that turbine blades provide the power production and the loads generated on the blades are transmitted to the rest of the turbine system, aerodynamic and structural optimization of the blades is very crucial. Blades must have low weight as much as possible, and loads incurred due to the flexing of the blades must be controlled, in other words loads must be alleviated. In the aforementioned studies, most of the work is dedicated to load reduction on the blades only. Different from most of the work in the literature, in this thesis study, the effect of bend-twist coupling that is generated by the use of glass fiber reinforced plastic (GFRP) and carbon fiber reinforced plastic (CFRP) materials, with different fiber angle configurations, in the flange regions between the spars of the turbine blade on the internal load alleviation in the whole wind turbine system is investigated both theoretically and experimentally. The main result to be reached is to achieve certain level of internal load alleviation in the critical monitor points in the wind turbine system by exploiting bend-twist coupling and validate the bend-twist coupling effect in plate and box-beam structures, which simulate the flange region between the spars in a wind turbine blade, through experimental and finite element analyses. Due to off-axis unidirectional laminae placement in the flange area between the spars, decrease in angle of attack is aimed that yields to load alleviation in the elements in the wind turbine system. Angle of attack is directly related to aerodynamic loads and the blade twists due to the bending under these loads that increase the angle of attack. With the utilization of the bend-twist coupling, induced twist in the opposite direction which prevents the increase in angle of attack with the purpose of load mitigation on the subcomponents of the wind turbine system is aimed.

Throughout the thesis, it is intended to measure the bend-twist coupling in composite structures by Digital Image Correlation (DIC) [23] system and to make comparisons with the finite element analysis results to evaluate the bending twisting coupling potential of E-Glass and Carbon composites. Bend-twist coupling determined by

means of finite element analysis and the digital image correlation system are compared mutually, and a reliable database is prepared for the bend-twist coupling effect for different composite material and for different off-axis fiber angle configurations. Since the bend-twist coupling has to be measured for different composite material and fiber angle configurations, instead of actual turbine blades, experimental study that is conducted with the DIC system is implemented on composite plate and box beam structures which simulate the flange regions between the spars of wind turbine blades. In order to have substantiated results for finite element analyses, determination of elastic properties of glass fiber reinforced plastic and carbon fiber reinforced plastic materials are done by following orthotropic material testing procedures [24] [25] [26]. Bend-twist coupling information that is obtained by the DIC system and finite element analyses is evaluated qualitatively rather than quantitatively; in other words, relative differences of the bend-twist coupling effect that is generated due to different composite material and fiber angle configurations are determined. The outcome of the experimental and numerical study provided information on how the bend-twist coupling potential of different composite materials, such as E-Glass and Carbon composites, vary with the off axis fiber angle. Based on this study, off-axis fiber angle range to be used in the bend-twist coupled blade designs is decided.

For the purpose of the investigation of load alleviation due to bend-twist coupling, transient flexible multi-body aeroelastic analyses of the whole wind turbine system are conducted for different blade configurations utilizing the wind turbine working scenarios and wind conditions that exist in the wind turbine design standard IEC 61400-1 [27]. In the model of the wind turbine system, except for the blade, standard sub-structures are used. Sub-structures that are used comprise of the rotor structure (blades and rotor hub), gear box and drive train, generator system, controller, and the tower structure. Blades with different material configurations created by the off-axis placement of the unidirectional composite layers are transferred to the multi body model of the wind turbine system, and for every material configuration of the blade, a different turbine model are created. Then, transient aeroelastic analyses of the turbine models are performed utilizing the real working scenarios and wind conditions defined

in the wind turbine design standard IEC 61400-1. The results of the transient aeroelastic analyses are processed, and for each design load case fatigue damage equivalent internal loads and extreme internal loads are calculated at the monitor points selected in the turbine system. Internal loads are compared and the effect of bend-twist coupling generated in the turbine blades on the internal load alleviation in the turbine system is investigated.

Since this thesis comprises of variety of work, they are divided into subdivisions. Chapter 2 is devoted to investigation of bend-twist coupling on composite plate and box-beam structures with different fiber orientations and materials, which simulate the skin and flange regions between the spars of wind turbine blade, via the DIC system. In Chapter 3, orthotropic material properties of GFRP and CFRP materials are determined by tensile testing by using international test standards. In Chapter 4, finite element analyses of composite plate and box-beam structures are performed under the same conditions as the experimental testing with DIC system so as to validate the test results. In these analyses, orthotropic material properties determined from material tests of GFRP and CFRP are utilized in order to have accurate results. The results of finite element analyses and experiments are compared in contemplation of validation and reliableness. Acquired information on the bend-twist coupling potential for different materials and different fiber orientations from experiments and finite element analyses performed for plates and box-beam structures form a basis for designing the bend-twist coupled wind turbine blades with the purpose of load reduction in the whole wind turbine system. As it is mentioned before, based on this study, off-axis fiber angle range to be used in the bend-twist coupled blade designs is decided. Multi-body dynamic wind turbine models with different blade designs are set up in Samcef Wind Turbines (SWT) [28] in order to investigate and compare the effect of bend-twist coupling on the load alleviation in the wind turbine system in Chapter 5. The effect of off-axis fiber orientation and usage of different materials on the potential of bend-twist coupling inspected under working scenarios for six different turbulent wind profiles created by the turbulent wind generator TurbSim [29]. Damage equivalent loads are calculated for the operation of the wind turbine system under six different randomly

generated turbulent wind profiles to provide a statistical average, as recommended by IEC 61400-1 [27]. In overall, results show that bend-twist coupled blades aid to mitigate loads in the critical monitor points at the components of the wind turbine system and have no major drawbacks in terms of power generation, maximum stresses in the blades, and tower clearance.

CHAPTER 2

EVALUATION OF THE BENDING-TWISTING COUPLING POTENTIAL OF COMPOSITE PLATES AND BOX-BEAMS VIA DIC MEASUREMENT METHOD

In wind turbine systems, the load alleviation at the monitor points is achieved by placing off-axis plies at the region between the spars on the wind turbine blades. Since the aim of the experiments is to determine bend-twist coupling potential in composite structures which have different fiber orientations and different materials via DIC measurement method, the experiments are done by using composite plates and torque-box structures that resemble the flanges and the flange regions between the spars. Figure 2.1 shows the upper and lower flanges and the flange area between the webs on an airfoil section. The flange area between the spars is actually a torque-box which is enclosed by dotted line in Figure 2.1. Box-beam structures that resemble to flange area between webs are produced with the purpose of determining bend-twist coupling potentials for these structures experimentally. Likewise, composite plate structures are manufactured that resemble the upper and lower flanges shown in Figure 2.1.

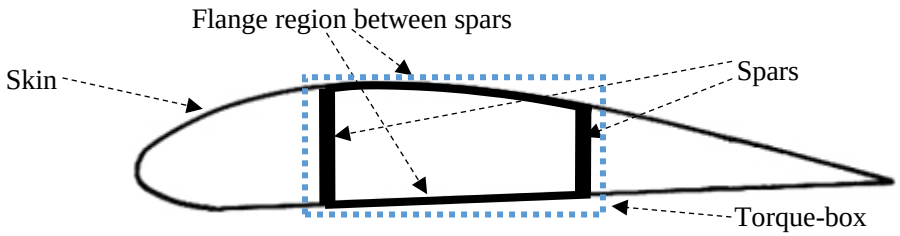

Figure 2.1 Flange area between the webs shown in an airfoil section

The main objective of this study presented in this chapter is to measure the effect of bend-twist coupling potential of different composite materials and different off-axis fiber angles. Throughout the experiments, a database is created to be used in the design of the wind turbine blades that are utilized in flexible multi-body wind turbine system models set up in SWT. The effectiveness of bend-twist coupling due to the material and fiber orientation acquired from the experiments sets a ground for deciding on the material selection and fiber orientation of the plies in the spar cap region between the spars of the wind turbine blades. The outputs of these tests are evaluated qualitatively; relative differences of bend-twist coupling potential of plates and torque-boxes with different fiber orientations and materials are compared. The acquired bend-twist potential data gives an idea about how effective the fiber orientation/material selection of the off-axis spar cap plies is on the load reduction in the wind turbine system.

2.1 DIC Methodology

The experiments are performed with the DIC method using the ARAMIS software which is a 3D contactless deformation measurement system [30]. It is used for analyzing, calculating and documenting deformations. The software perceives the surface of the object which is being experimented and places coordinates to the pixel images. If the surface of the object lacks surface characteristics, a stochastic spray paint pattern is applied on the surface of the object. Figure 2.2 shows such a pattern. The first photo image taken is the undeformed state of the object. During the deformation measurement process, further images are taken and recorded. Having recorded sufficient photo images of the deformed and the undeformed state of the object, ARAMIS compares and calculates displacements and deformations using the digital images. ARAMIS system is applicable for measuring three-dimensional displacements and strains of the objects under static or dynamic loads.

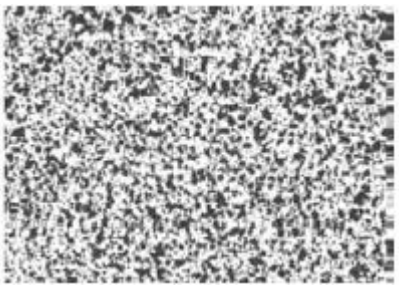

Figure 2.2 Stochastic spray pattern on the surface

Digital Image Correlation method has very important and distinctive features compared to conventional deformation measurement techniques. These can be listed as such:

- 2D or 3D measurements
- Full-field graphical 3D representation of the results
- Various geometries with different dimensions (from 1 mm to 2000 mm) can be measured
- Mobility of the system
- Both small and large deformations can be measured with the same sensors
- Variation in lighting system and conditions automatically compensated
- Transformation of the coordinate system

For a 3D measurement, two cameras are used in order to have a calibrated 3D resulting measurement volume. Deformations are then calculated by using rectangular image details called *facets* by comparing digital images taken by two cameras. Figure 2.3 shows 15x15 pixel facets that have 2 pixel overlapping scheme of the initial stage.

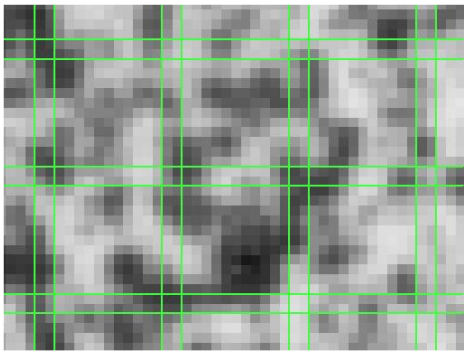

Figure 2.3 15x15 pixel facets with 2 pixels overlapping (6 facets in total)

Deformations on the body are determined by comparing left and right camera images with the undeformed original state of the body using photogrammetric methods. The both 2D images of left and right camera result in common 3D view. Figure 2.4 shows the deformed and undeformed facet states that are seen by left and right cameras. In these images, white dashed line shows the undeformed state and the green line shows the deformed state of the specific facet which is being investigated. Having done the successful computation process, the requested measurement results become available in the ARAMIS program interface.

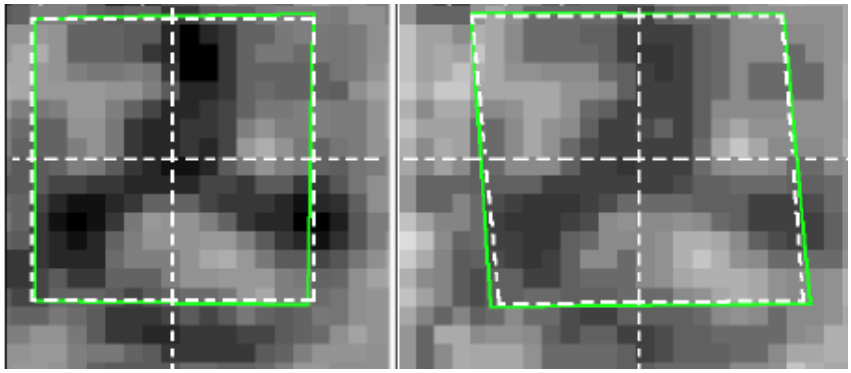

(a) (b)

Figure 2.4 Deformed and undeformed images of the body seen by (a) left and (b) right cameras

Region of interest (ROI) should be specified in the undeformed state image and divided into evenly spaced virtual grids (facets). The strains or displacements are calculated at each point of the facets to obtain full-field strain or deformation field for

the paint area on the body. For the precise tracking of the motion of each point of interest, a reference subset of $(2n+1)$x$(2n+1)$ pixels centered at the reference point $P(x_0,y_0)$ from the image of undeformed state is selected and utilized to track its conforming location in the target image. The tracking process in the DIC method is practiced by searching the position of extremity of a pre-defined similarity criterion-called *correlation criterion*. Displacement and strain components of the undeformed and target deformed subset centers are determined once the maximum similarity is obtained in the target subset of the deformed image [31]. The same procedure is repeated for the remaining deformed images to obtain full-field displacement and/or strain of the region of interest. It is worth to note that, for the trade-off of spatial resolution and computational time, it is customary to select the facet size to overlap each other.

2.2 DIC Configuration

Displacements of composite plates and box-beam structures with different materials and different fiber orientations are evaluated by DIC method. The tests are done in Middle East Technical University Center for Wind Energy (METUWIND) Composite Materials Characterization Laboratory using GOM ARAMIS 4M with adjustable base DIC sensor system. The system basically consists of two cameras, a base, and a slider. Figure 2.5 visualizes the top view of ARAMIS 4M DIC system sensor unit. Calibration process should be followed before the measurement. The measuring height, length, and depth depend on how the calibration is made. The calibration is done by configuring the base and the slider distance, camera angle, focus and aperture of the camera. For the DIC tests of composite plates and box-beam structures, 20 mm Titanar camera lenses are used for measuring height of 150 mm, length of 200 mm, and depth of 170 mm. The measuring distance is set to be 365 mm and the calibration is made accordingly.

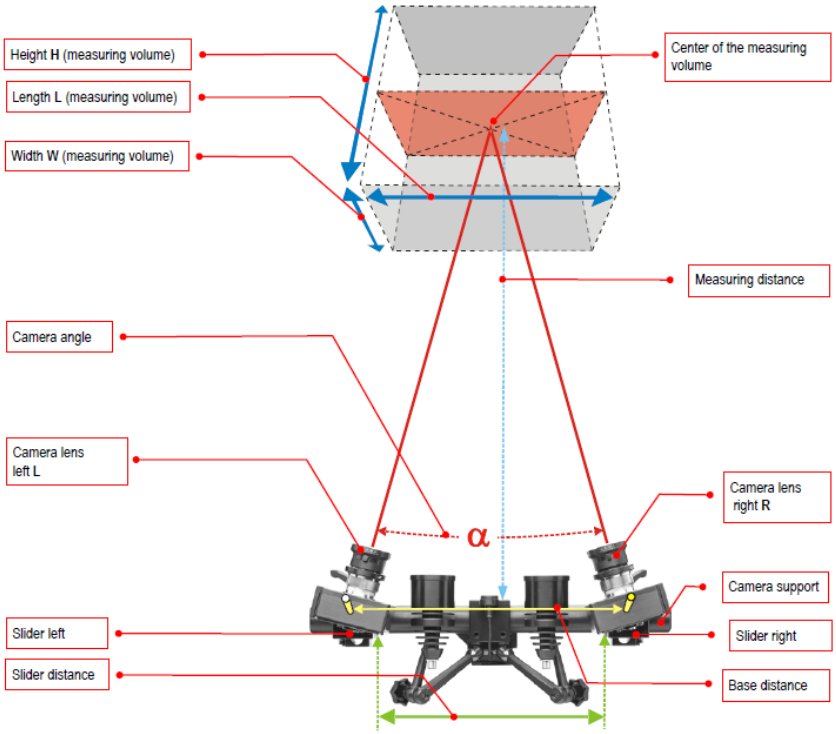

Figure 2.5 Top view of ARAMIS 4M sensor unit [32]

2.3 Test Specimens

The composite plates and box-beam structures which are made of GFRP and CFRP materials are produced by Yüksel Composite Technologies Inc. The composite plates have fiber angles of 0°, 10°, 15°, 20°, and 25° with respect to the plate axis and are made from unidirectional GFRP and CFRP composite layers. In total, 10 plates are produced, 5 using GFRP and 5 using CFRP material. The box-beam structures have fiber angles of 0°, 15°, and 25° and are made from unidirectional GFRP and CFRP composite layers. Thus, in total 6 torque-boxes are tested. The fiber angle configuration of plates and box-beam structures are visualized in Figure 2.6 and fiber angle is denoted by letter φ. The constituents of the composite plates and the box-beams are presented in Table 2.1.

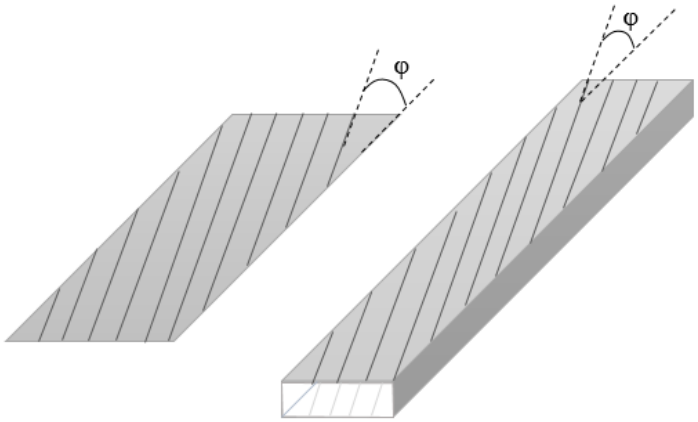

(a) (b)

Figure 2.6 Fiber angle configuration of composite (a) plates and (b) box-beam structures

Table 2.1 The constituents of GFRP and CFRP composite plates and box-beams

Constituent	**Material Name**
Resin	Biresin CH80-2 [33]
UD Carbon Fiber Fabric	UC200TFX [34]
UD Glass Fiber Fabric	Interglas 92145 [35]

Figure 2.7 and Figure 2.8 show the room temperature cured composite plates and box-beam structures that are made of GFRP and CFRP materials with different fiber angles produced by Yüksel Composite Technologies Inc. The composite plates are made of 10 layers and have the dimensions of 50 cm x 15 cm. Fiber volume fraction is 45% for both plates and box-beam structures. Thicknesses of GFRP plates are determined to be 1.58 mm for all fiber angle configurations. However, because of the thicker yarn structure of the UD carbon fiber, thicknesses of CFRP plates vary considerably. For the fiber orientation angles 0°, 10°, 15°, 20°, and 25°, the thicknesses of the plates are 2.77 mm, 2.86 mm, 2.92 mm, 2.94 mm, and 3.02 mm, respectively.

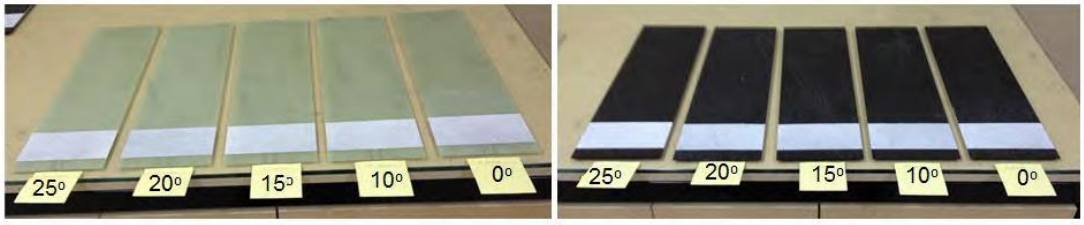

(a) GFRP plates (b) CFRP plates

Figure 2.7 GFRP and CFRP plates with off-axis unidirectional layers / Fiber angles = 0°, 10°, 15°, 20°, 25°

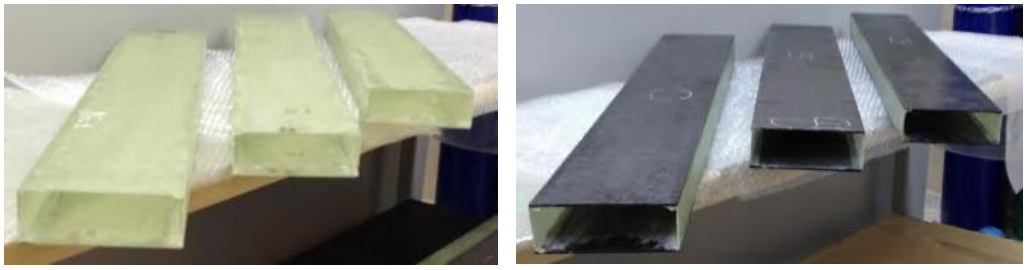

(a) GFRP box-beam structures (b) Hybrid box-beam structures

Figure 2.8 GFRP and CFRP box-beam structures with off-axis unidirectional layers in the top and the bottom flanges / Fiber angles = 0°, 15°, 25°

The box-beam structures having the fiber orientations of 0°, 15°, and 25° with the dimensions of 100 cm x 15 cm x 5 cm are made of GFRP and CFRP materials. The upper and lower flanges of the GFRP box-beam structures are made of 8 plies of unidirectional glass fiber layers having the total thickness of 1.264 mm, whilst hybrid GFRP-CFRP ones are made of 8 plies of unidirectional carbon fiber layers having the total thickness of 2.32 mm. For all fiber angle configurations, the webs of the box-beam structures are made of 8-ply symmetric layup ($[0/90/0/90]_s$) of GFRP material in order to assess the bend-twist coupling potential of flange material due to the off-axis fiber angles.

It should again be noted that box-beam structures resemble to the flange region between the spars of the wind turbine blade, and in the present study evaluation of

bend-twist coupling effect due to different fiber orientations and different materials on the spar caps is also studied on box beam structures, besides composite laminates.

In composite materials with off-axis unidirectional plies, flapwise bending moment (M_y), and torsional moment (M_z) are related to bending curvature (κ_y) and rate of twist (ϕ_z) by Equation 1 [36],

$$\begin{Bmatrix} M_y \\ M_z \end{Bmatrix} = \begin{bmatrix} EI & -g \\ -g & GJ \end{bmatrix} \begin{Bmatrix} \kappa_y \\ \phi_z \end{Bmatrix} \tag{1}$$

where, EI and GJ are bending and torsional stiffness, respectively, and g is the parameter of coupling which is zero for beams with on-axis ply placement or isotropic materials where no coupling is involved between bending and twist. Parameter of coupling (g) is defined as in Eq. 2:

$$g = \alpha\sqrt{EIGJ}, \qquad -1 < \alpha < 1 \tag{2}$$

where, α varies between -1 and 1 based on fiber angle orientation. If composite plies are oriented towards leading edge (*feather*) value of the coefficient α varies between -1 and 0, and if plies are directed towards trailing edge (*stall*), α varies between 0 and 1. If composite plies are placed towards leading edge, the body twists in the opposite direction of increasing angle of attack due to bending. If the plies are oriented towards trailing edge, the body twists in the same direction of increasing angle of attack, thus increases effective angle of attack and reduces stall speed.

2.4 Experimental Evaluation of the Potential of Bend-Twist Coupling via DIC System

2.4.1 Bend-Twist Coupling Tests of Composite Plates

In order to measure the displacements of composite plates and box-beams using the ARAMIS 4M DIC system, the measurement field is painted with stochastic color spray pattern. With the DIC system, the measurement of vertical displacement of paint field

is possible. The plates and box-beams are clamped using vice jaw and joiner's clamps for a distance of 10 centimeters from the root. Boundary conditions, load application region, and the locations that the displacements are measured on composite plates via DIC cameras are presented in a schematic diagram in Figure 2.9. The load is applied through steel blocks that have surface dimensions of 30.3 mm and 14.8 mm at the center of the tip location. The displacement measurements are performed 5 centimeters from the tip of the plates so as to eliminate the local effects due to the load applied. Stochastic paint field is applied 2.5 cm away from the tip for an area of 10 cm x 15 cm which encloses the measurement points. Figure 2.10 shows the left and right vertical displacement measurement points on the stochastic paint pattern applied on the composite CFRP plate with fiber orientation angle of 25°. As the static load is applied, the twist due to bending occurs as a result of anisotropic behavior of composite material.

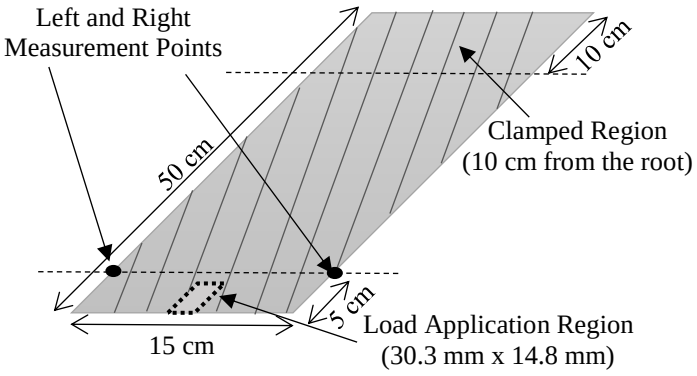

Figure 2.9 Test configuration of composite plates

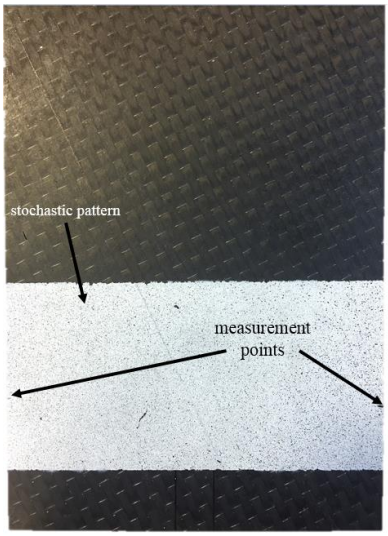

Figure 2.10 Measurement points on the CFRP plate with fiber orientation angle of 25°

The load on the composite plate is applied using a steel block weighing 105.95 gr for GFRP plates and 432.08 gr for CFRP plates which is placed between the marks shown in Figure 2.11. Since the CFRP material is much stiffer than the GFRP material, approximately four times more weight is used for the deformation experiments of CFRP plates. Note that it is vital to place the weight symmetrically in order to observe the twist due to the bending under the load applied.

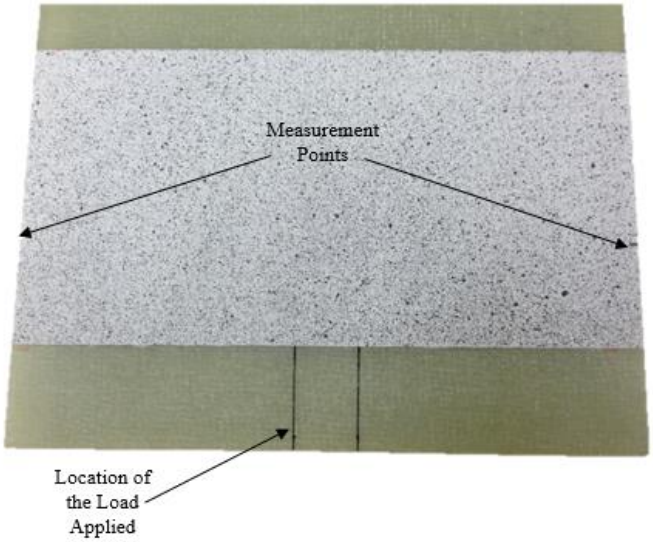

Figure 2.11 Measurement points and the location of the load applied on a GFRP plate

In this work, the effect of fiber orientation on the bend-twist coupling potential is determined by the resulting twist angle, at the section of the plate where measurements are taken, due to the bending load applied. The twist angle (θ) can be determined by dividing the difference of lateral displacements of the left and the right measurement points to the plate width for each plate. The calculation of twist angle can be visualized in Figure 2.12.

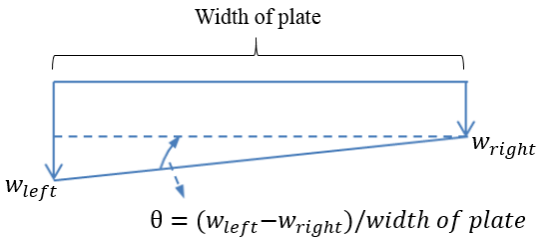

Figure 2.12 Twist angle calculation of plates and box-beams

With small angle approximation, Eq. 3 holds.

$$\tan\theta \approx \theta \tag{3}$$

As mentioned previously, the magnitude of the applied load is different for GFRP and CFRP plates. Moreover, material properties, especially bending stiffness of GFRP and CFRP materials are quite different. As depicted in Figure 2.12, lateral displacement (*w)*, and so twist angle *(*θ) are directly related to bending stiffness and magnitude of the applied load. Therefore, unit twist angle concept is anticipated in order to eliminate the effects of the magnitude of the applied load and the indifferences of bending stiffness of GFRP and CFRP materials. Main idea of this proposition is to divide the twist angle by the lateral deformation of the central location so as to eliminate aforementioned effects. Nevertheless, preliminary experiments and finite element analyses showed that the central location is in the vicinity of the local effects produced by the applied load, especially for the torque-boxes. Figure 2.13 shows the local effects occurred at the central location on an on-axis hybrid GFRP-CFRP box-beam due to the load applied calculated by ARAMIS software and finite element analysis. Consequently, it is proposed to calculate the bend-twist coupling potential through the

twist angle per unit lateral displacement by dividing the twist angle with the mean of the left and right displacements, as presented in Figure 2.12.

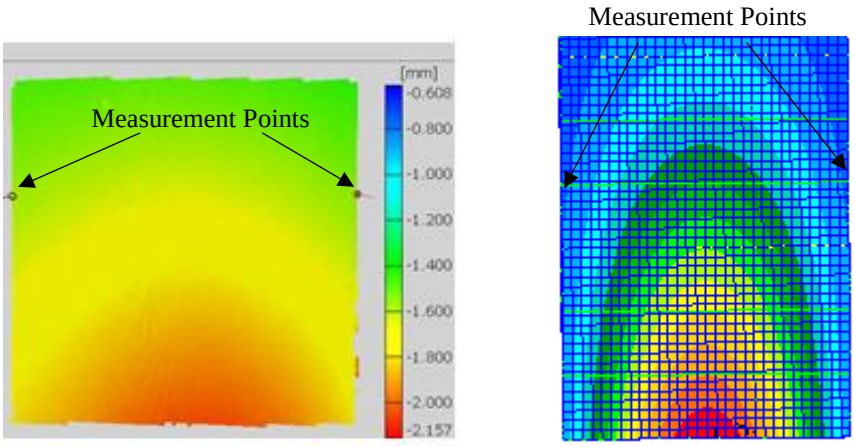

(a) (b)

Figure 2.13 Local effect occurrence on 0° hybrid GFRP-CFRP box beam calculated by (a) ARAMIS software and (b) finite element analysis

$$\hat{\theta} = \frac{\theta}{\frac{1}{2}(w_{left}+w_{right})} \tag{4}$$

Figure 2.14 shows the test setup for the measurement of the lateral displacements of CFRP plates with the DIC system. Ten centimeter of the plate is clamped from the root of the plate and the weight is placed at the tip of the plate symmetrically. The cameras are placed at a distance of 365 millimeters from the plate via the aid of a tripod in order to have a correct full-field measurement. The measurement area is 150 mm in height and 200 mm in width; therefore, DIC system covers the stochastic paint area fully. LED light sources are used in order to eliminate the image capture loss due to shading.

For the DIC tests of composite plates and box-beam structures, 20 mm Titanar camera lenses are used for measuring height of 150 mm, length of 200 mm, and depth of 170 mm (Figure 2.5). The measuring distance is set to be 365 mm and the calibration is made accordingly.

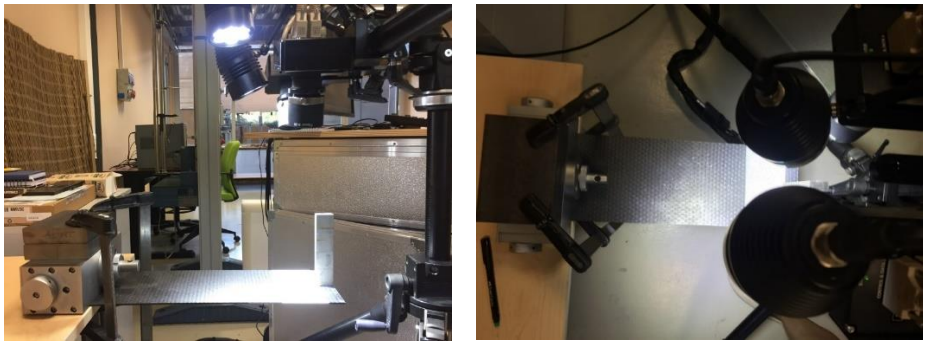

(a) (b)

Figure 2.14 (a) DIC system test setup for CFRP plates (b) Top view of the setup

Figure 2.15 shows the DIC system test setup for a GFRP plate. Since the load applied on GFRP plate is much lower than that of CFRP plate, the weight used for clamping the GFRP plate is sufficient.

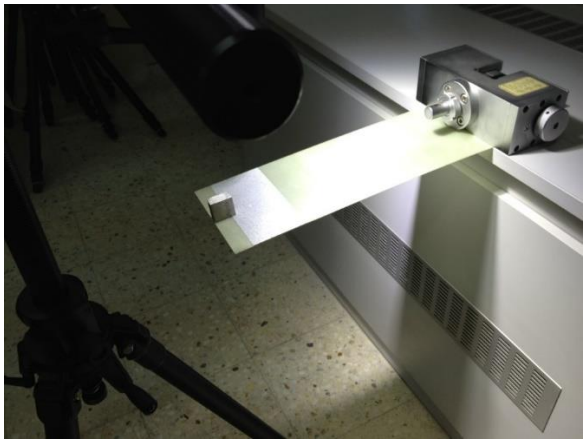

Figure 2.15 DIC system test setup for GFRP plates

In the experiments, ARAMIS software is used in order to calculate the deformations of the plates and the torque-boxes by processing on the images captured by the DIC system. During the test process, two images are captured. The first image is a reference image, and it is taken for the unloaded state. The second image is taken for the loaded state and the deformations are calculated with respect to the initial image. Figure 2.16 shows the ARAMIS software interface which gives the deformation of the GFRP plate with 0° fiber orientation under the 105.95 gr weight applied symmetrically at the tip.

The local coordinate system is placed on the reference image within the paint field and +z direction is out of the page. Therefore, in the loaded state, the lateral displacements that occur due to the application of the load are indicated with minus sign. In Figure 2.16, the displacements measured at the left and the right measurement points with respect to the initial unloaded state are presented in tables. The color scale indicates the lateral displacements due to the applied load within the paint field that DIC system detects. Specifically for this fiber orientation angle, there is a slight difference between left and right measurement points (about 0.2 millimeters). Ideally, for 0° fiber orientation angle, the lateral displacements of left and right measurement points should be the same since there is no bend-twist coupling for unidirectional on-axis 0° layup configuration. A reason for such a difference in displacements at measurement points is misalignment of fibers during the vacuum infusion process. Another reason is that the thickness of paint. Since the DIC system performs measurements very precisely, the difference in the thickness of paint can also be detected by DIC system. All these effects together with the slightest unsymmetrical loading that would have been caused during the placement of the weight at the tip of the plate are deemed to be the reason for the discrepancy between the displacements measured at the left and right measurement points.

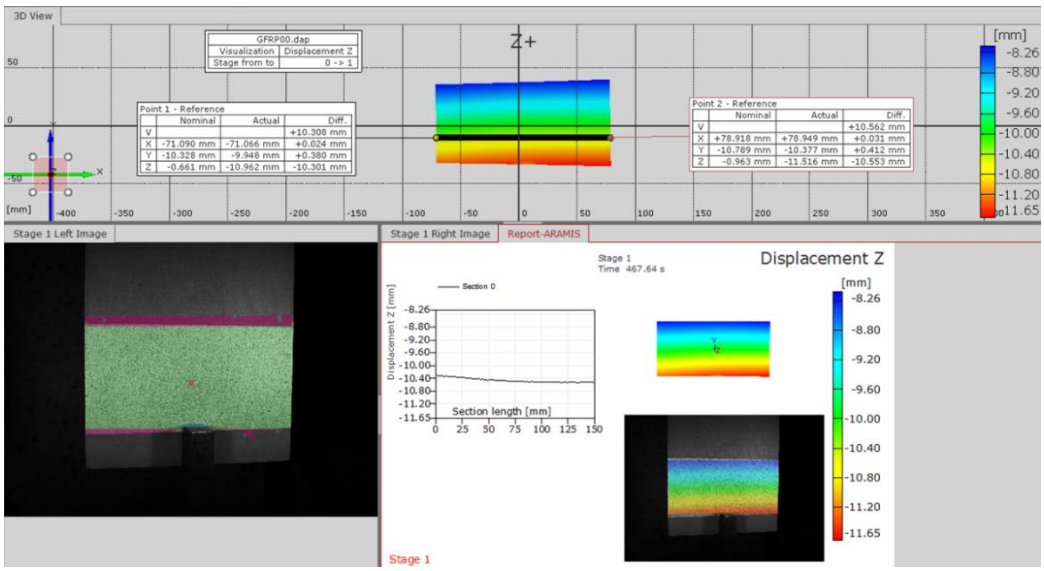

Figure 2.16 Deformation of the GFRP plate with 0° fiber angle– ARAMIS software interface

Figure 2.17 shows the ARAMIS software interface which gives the deformation of the GFRP plate with 25° fiber orientation under the 105.95 gr weight applied symmetrically at the tip. In this case, because the plate is composed of layer with ply angle of 25°, the plate twists as it bends due to the anisotropic behavior of the composite material. As a result of the bend-twist coupling, the lateral displacement at the left measurement point is observed to be 16.420 millimeters whilst the lateral displacement at the right measurement point is detected to be 13.625 millimeters.

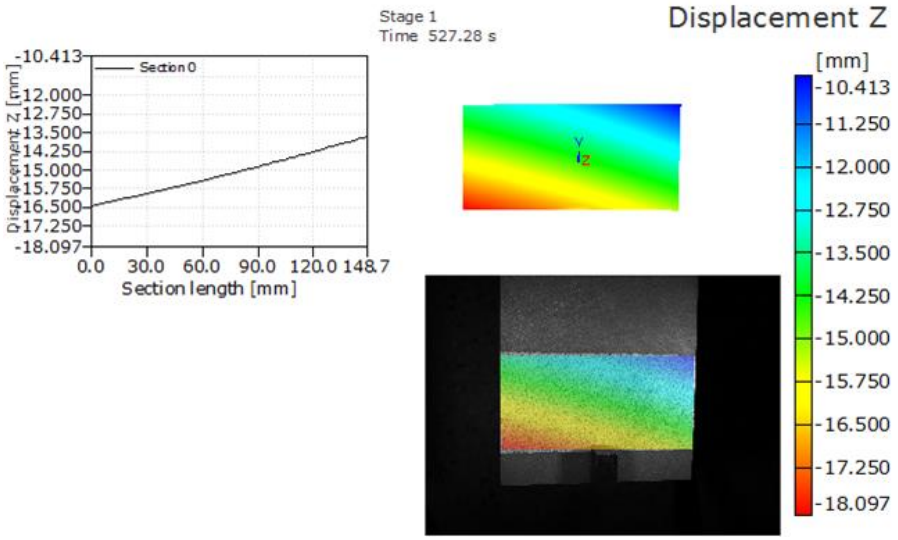

Figure 2.17 Deformation of the GFRP plate with 25° fiber angle – ARAMIS software interface

Figure 2.18 presents the lateral displacements at the left and right measurement points in the tables and the lateral displacement contours for GFRP plates having 10°, 15°, 20°, and 25° fiber orientation angles with 105.95 gr weight applied symmetrically at the tip of the plates. It is noted that as fiber orientation angle increases, the lateral displacements at the measurement points increase due to the reduced bending stiffness due to increased fiber angle. Moreover, bend-twist coupling effect can be observed better with increasing fiber angle as the difference in lateral displacements at the left and right measurement points becomes higher.

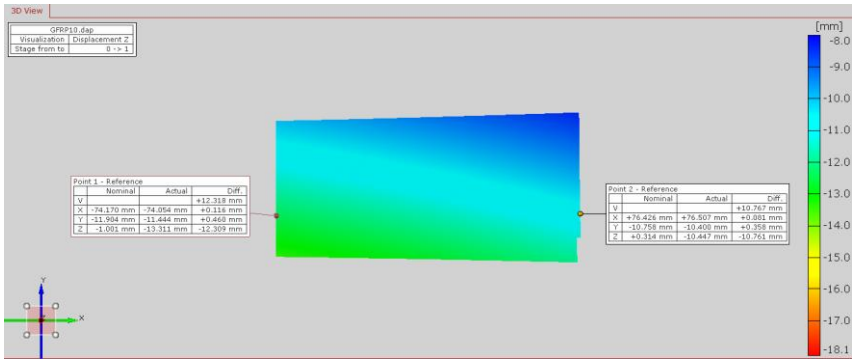

(a)

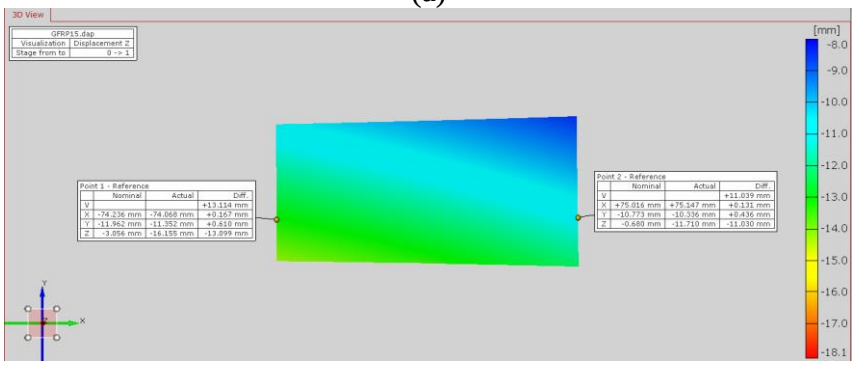

(b)

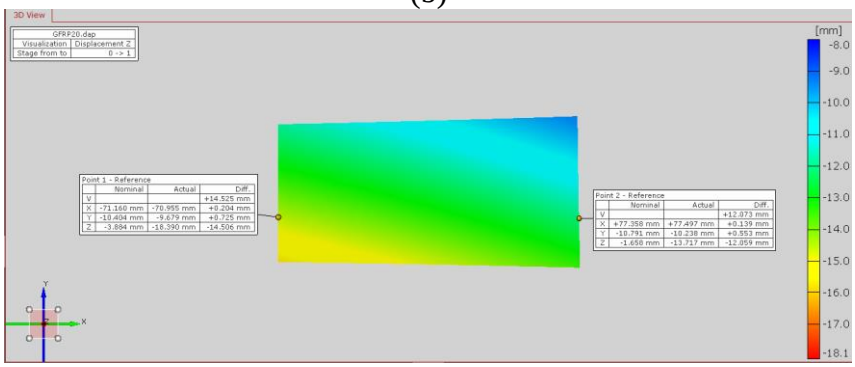

(c)

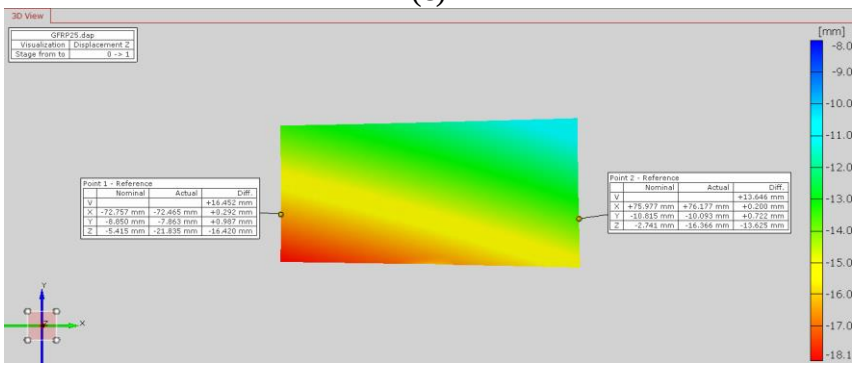

(d)

Figure 2.18 Lateral displacement contours calculated by the ARAMIS software interface of GFRP plates having fiber angle orientations of (a) 10° (b) 15° (c) 20° (d) 25°

Table 2.2 presents the twist angles per unit lateral displacement of the GFRP plates having 0°, 10°, 15°, 20°, and 25° fiber angle orientations. As discussed before, twist angle per unit lateral displacement is a measure of the bend-twist coupling potential of the composite material since the effects of bending stiffness of the plate and the magnitude of the load applied are eliminated by dividing the twist angle by the lateral displacement. Twist angle (θ) and unit twist angle $(\hat{\theta})$ values are calculated using Figure 2.12 and Eq. 4, respectively. As the fiber angle increases, bending stiffness of the plate reduces. Thus, unit twist angle concept is the correct metric in order to investigate the bend-twist coupling potential of the composite material which is free of the effect of bending stiffness of the plates. Lateral displacements of the left and the right points are measured 5 cm away from the tip in order to suppress the local effects of the load applied. As it is seen in Table 2.2, unit twist angle, along with the twist angle, increases with increasing fiber angle for GFRP plates.

Table 2.2 Bend-twist coupling potentials of GFRP plates for different fiber orientation angles

Fiber Orientation Angle (°)	**Displacement of Left Measurement Point (mm)**	**Displacement of Right Measurement Point (mm)**	**Twist Angle (°)**	**Unit Twist Angle (°/mm)**
0	10.30	10.55	-0.094	-0.0090
10	12.31	10.76	0.591	0.0512
15	13.10	11.04	0.789	0.0654
20	14.52	12.07	0.935	0.0704
25	16.46	13.64	1.077	0.0716

Figure 2.19 illustrates the variation of unit twist angle with respect to fiber orientation angle of GFRP plates. It is seen that unit twist angle increases significantly with the fiber orientation angle in the range 0°-15°. Beyond the 15^{o} fiber angle, the growth of the unit twist angle slows down. Investigating the figure, one can conclude that further increasing the fiber angle will not be advantageous in terms of increasing the bending twisting coupling potential for the GFRP composite material.

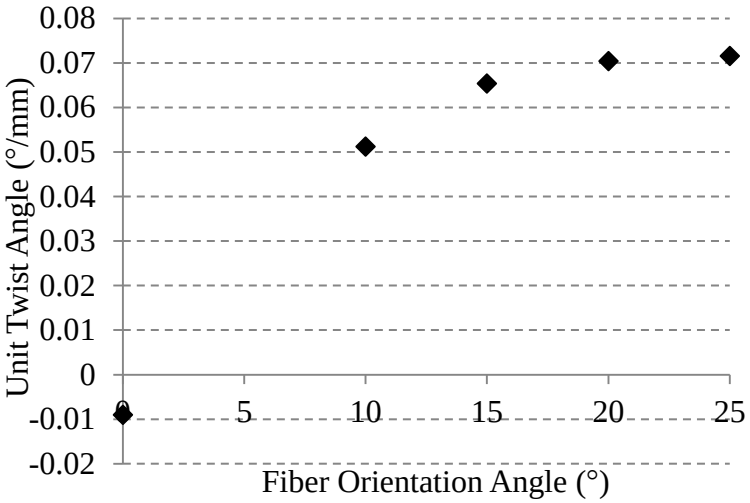

Figure 2.19 Variation of the unit twist angle with the fiber orientation angle for GFRP plates

Since the bending stiffness of CFRP plates are higher than that of GFRP plates, a steel block weighing 432.08 gr is used for the evaluation of bend-twist coupling of CFRP plates. Figure 2.20 shows the ARAMIS software interface which gives the deformation of the CFRP plate with 0° fiber orientation under 432.08 gr weight applied symmetrically at the tip of the plate. In Figure 2.20, the displacements measured at the left and the right measurement points with respect to the initial unloaded state are presented in tables. For this fiber orientation configuration, there is about 3 mm displacement (2.829 mm and 2.988 mm lateral displacements for the left and the right measurement points, respectively) occurs at the section where the bend-twist coupling is investigated.

Figure 2.21 shows the ARAMIS software interface which gives the deformation of the CFRP plate with 25° fiber orientation under the 432.08 gr weight applied symmetrically at the tip of the plate. Because of the 25° of fiber angle, the plate twists as it bends due to anisotropy. As a result of bend-twist coupling, the lateral displacement at the left measurement point is measured as 10.321 millimeters whilst the lateral displacement at the right measurement point is measured as 6.164 millimeters. Left measurement point deflects approximately 67% more when compared to the right measurement point.

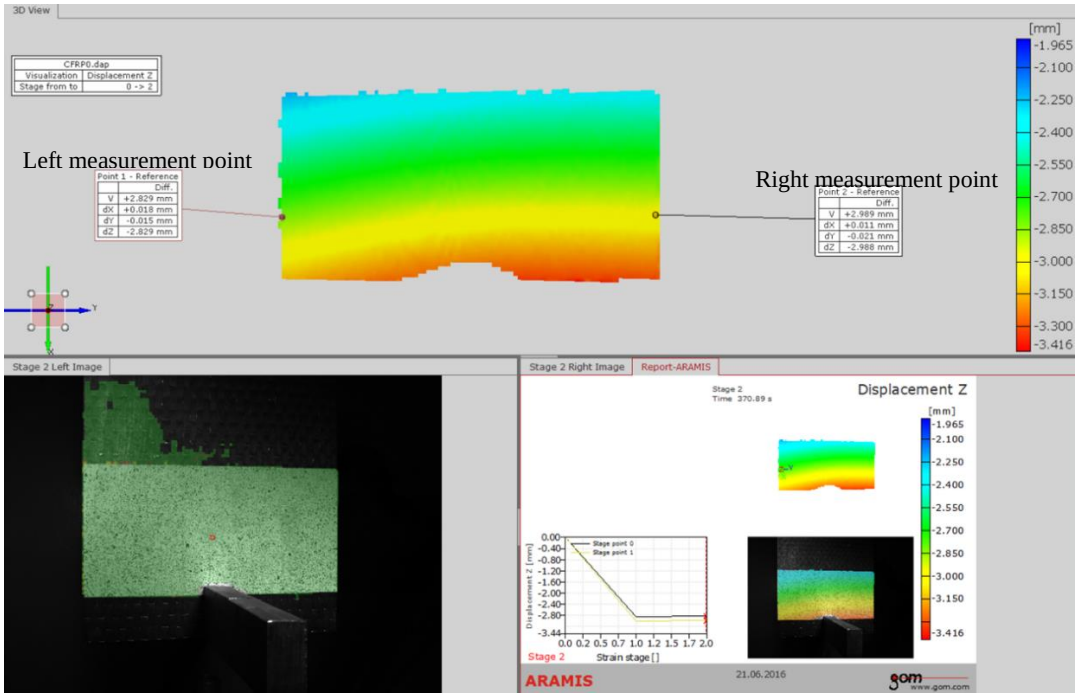

Figure 2.20 Deformation of the CFRP plate with 0° fiber angle – ARAMIS software interface

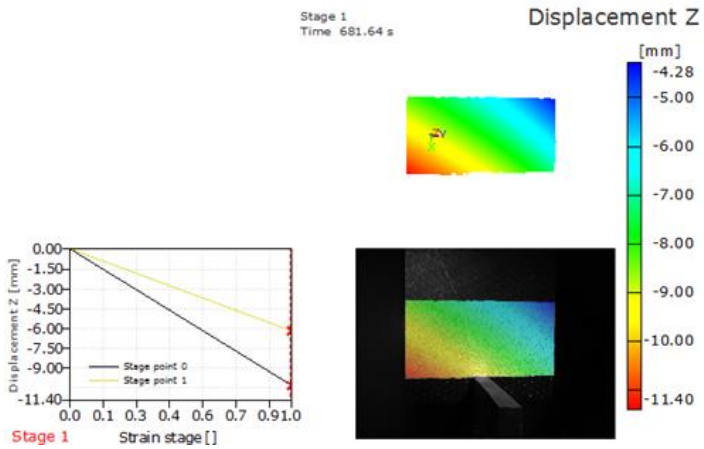

Figure 2.21 Deformation of the CFRP plate with 25° fiber angle – ARAMIS software interface

Figure 2.22 presents the lateral displacements at the left and right measurement points in the tables and the lateral displacement contours for CFRP plates having 10°, 15°, 20°, and 25° fiber orientation angles with 432.08 gr weight applied symmetrically at the tip of the plates.

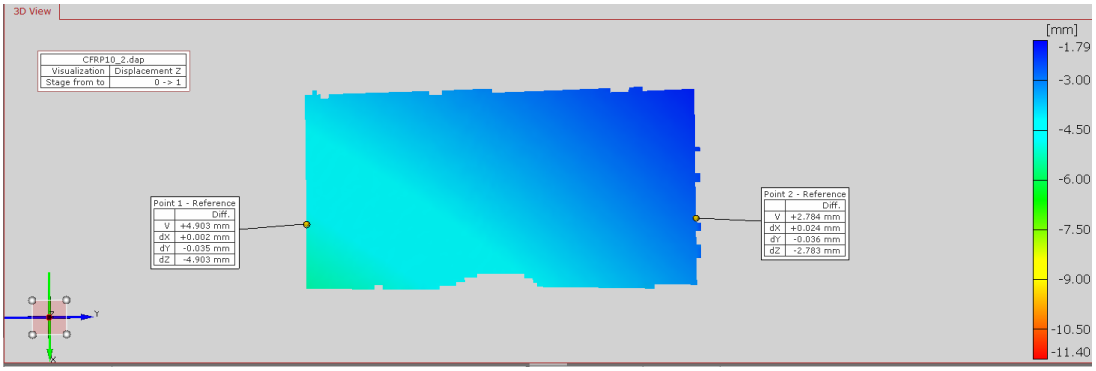

(a)

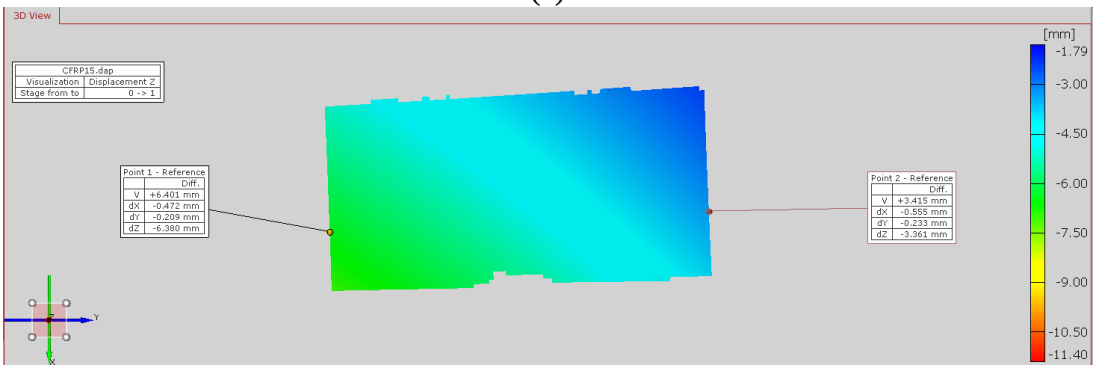

(b)

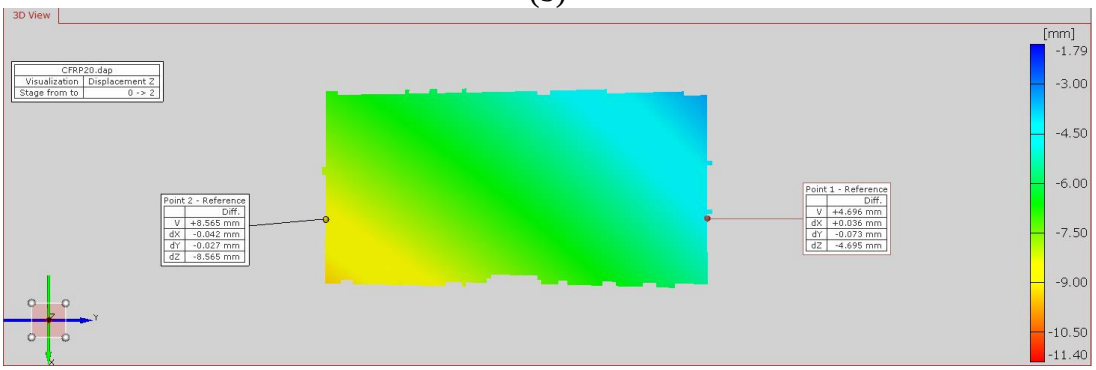

(c)

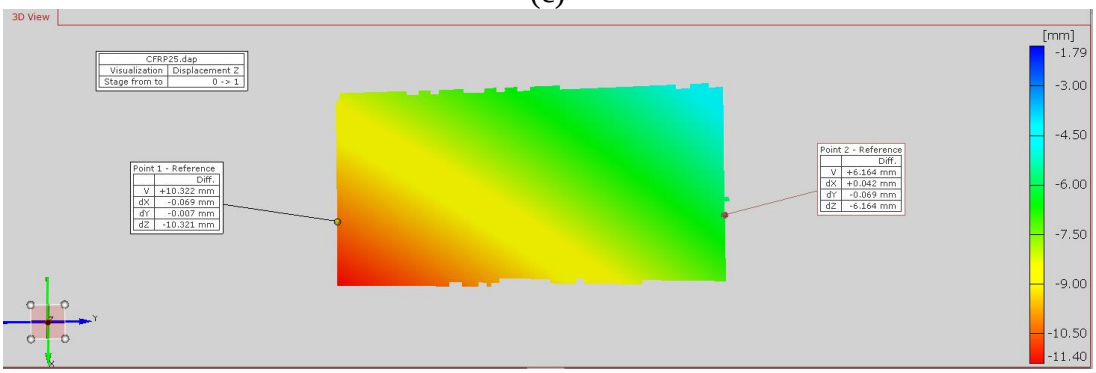

(d)

Figure 2.22 Lateral displacement contours calculated by the ARAMIS software for CFRP plates having fiber angle orientations of (a) 10° (b) 15° (c) 20° (d) 25°

As for the GFRP plates, the lateral displacements at the measurement points of CFRP plates increase when the fiber angle is increased due to the associated reduced bending stiffness. Similar to the GFRP plates, as the off-axis fiber angle is increased, the difference between the lateral displacements on the left and the right sides of the plates increase which is clearly identified from the color scale whose range is fixed for all plates.

Table 2.3 gives the bend-twist coupling potentials of CFRP plates having 0°, 10°, 15°, 20°, and 25° fiber angle orientations. Comparison of Table 2.2 and Table 2.3 reveals that the displacements at the left and the right measurement points for the CFRP plates with varying fiber orientation angles are less than that of GFRP plates. One of the reasons for lower displacements at these monitor points is that the average thickness of CFRP plates is determined to be 2.9 mm whilst the average thickness of GFRP plates is 1.58 mm. Moreover, it is a known fact that the modulus of elasticity in the fiber direction (E_{11}) of the CFRP material is far superior to that of the GFRP material. The twist angle, along with the displacements of the monitor points, increases with the increase in the fiber angle of CFRP plates. Figure 2.23 illustrates the variation of the unit twist angle with respect to fiber orientation angle for the CFRP plates. For the CFRP plates it is noticed that although the twist angle increases with the fiber angle, unit twist angle, calculated using Eq. 4 which is the pure indicator of bend-twist coupling potential of CFRP plates, reaches its highest value at approximately 15° fiber orientation angle.

Table 2.3 Bend-twist coupling potentials of CFRP plates for different fiber orientation angles

Fiber Orientation Angle (°)	**Displacement of Left Measurement Point (mm)**	**Displacement of Right Measurement Point (mm)**	**Twist Angle (°)**	**Unit Twist Angle (°/mm)**
0	2.83	2.99	-0.061	-0.0209
10	4.88	2.86	0.770	0.1988
15	6.40	3.42	1.140	0.2324
20	8.57	4.70	1.478	0.2229
25	10.32	6.16	1.588	0.1926

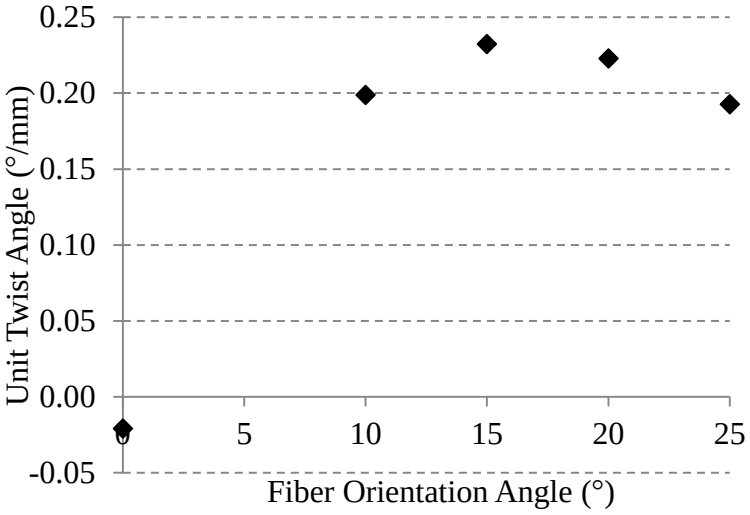

Figure 2.23 Variation of the unit twist angle with the fiber orientation angle for CFRP plates

Table 2.4 presents the comparison of bend-twist coupling potentials of GFRP and CFRP plates having fiber angle orientation of 0°, 10°, 15°, 20°, and 25°. Despite of the fact that thicknesses of the plates and the magnitude of the load applied differ for the GFRP and the CFRP plates, these effects are eliminated by using unit twist angle concept. The ratio of bend-twist coupling potential is examined by ratio of unit twist angles of CFRP and GFRP plates. In Table 2.4, the ratio of the bend-twist coupling potential for the 10° fiber orientation angle is 3.88 which indicates that bend-twist coupling potential of CFRP material with 10° fiber angle has almost 4 times higher than that of GFRP material with the same fiber angle configuration. The ratio of the unit twist angles decreases as the fiber angle increases. This study has shown that bending twisting coupling potential of the CFRP material is higher than the bending twisting coupling potential of the GFRP material and CFRP can be considered to be a more effective material in the load alleviation study in wind turbine blade through the use of bend-twist coupled blades.

Table 2.4 Comparison of bend-twist coupling potentials of GFRP and CFRP plates

Fiber Orientation Angle (°)	GFRP Plates		CFRP Plates		(CFRP/GFRP) Ratio of Unit Twist Angle
	Twist Angle (°)	Unit Twist Angle (°/mm)	Twist Angle (°)	Unit Twist Angle (°/mm)	
0	-0.094	-0.009	-0.061	-0.0209	-
10	0.591	0.0512	0.770	0.1988	3.88
15	0.789	0.0654	1.140	0.2324	3.55
20	0.935	0.0704	1.478	0.2229	3.17
25	1.077	0.0716	1.588	0.1926	2.69

2.4.2 Bend-Twist Coupling Tests of Box-Beam Structures

The study of bend-twist coupling potential of the GFRP and the CFRP material yields valuable results with plate tests. In this section the same study is performed for box-beam structures which again simulate flange region between the spars of a wind turbine blade. For this purpose, the torque-boxes having the dimensions of 100 cm x 15 cm x 5 cm are produced with fiber orientations of 0°, 15°, and 25° in the upper and lower flanges in order to evaluate the bend-twist coupling potentials. As in the case of plate experiments, bend-twist coupling potentials of torque-boxes, whose flanges are made from GFRP and CFRP materials having different fiber angle orientations, are measured utilizing the lateral deflections of the left and the right measurement points. Figure 2.24 shows the measurement point locations and measurement area of a GFRP box-beam structure. The measurement points are located 20 cm away from the tip so as to discard the local effects caused by the load. The load is applied through steel blocks having dimension of 10 cm in length and 15 cm in width which is the same as the boxes' width. Box-beams are clamped using vice jaw and joiner's clamps for a distance of 10 centimeters from the root of the box beams and steel blocks having the weight of 2901 gr and 5766 gr are applied at the tip location, as shown in Figure 2.25. The displacements at the left and right measurement points are measured by the DIC

system and Figure 2.26 illustrates the test setup of GFRP and CFRP box-beam structures.

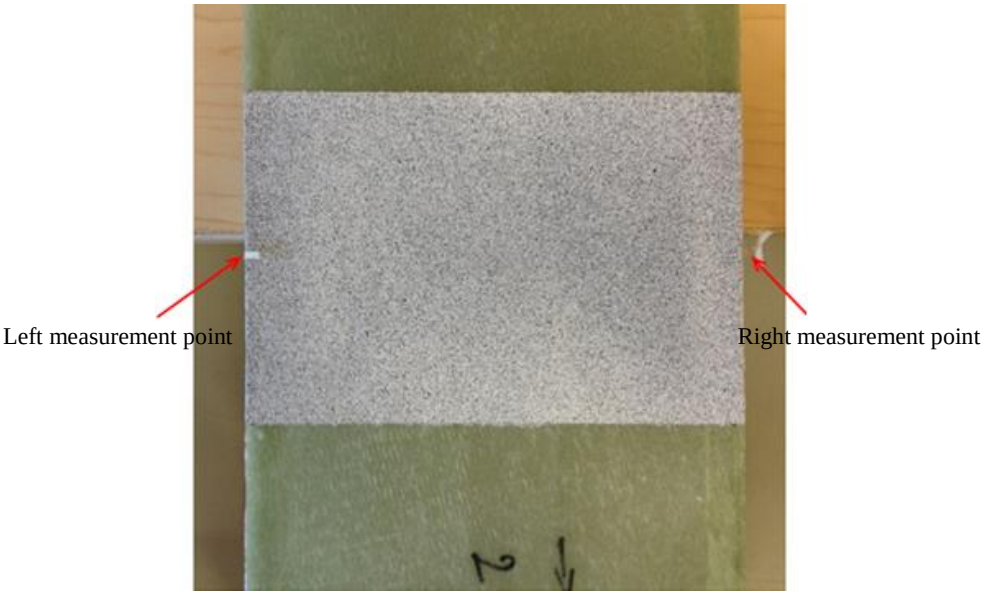

Figure 2.24 The measurement point locations and the measurement area on a GFRP box-beam structure

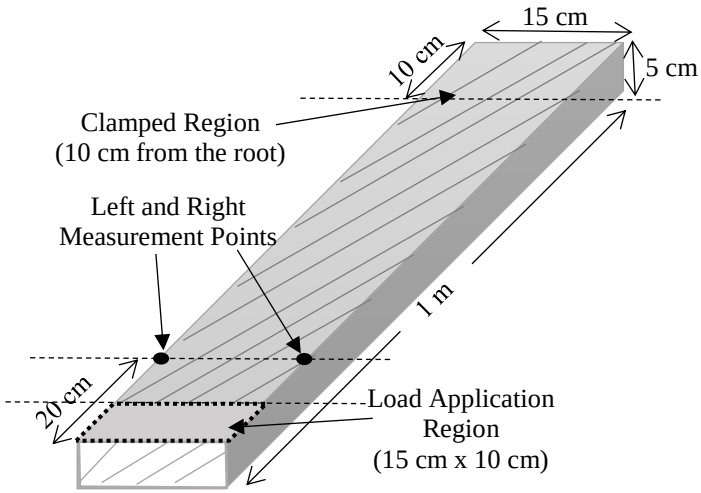

Figure 2.25 Test configuration of composite torque-boxes

Figure 2.26 DIC test setup of CFRP and GFRP box-beam structures

Before the bending twisting coupling tests, in order to check the linear dependence of the applied load and the resulting deflection and also to check accuracy of the DIC system a test procedure has been followed by applying steel blocks having 2901 gr and 5766 gr as loads on a GFRP box-beam structure with 0° fiber orientation. Figure 2.27 and Figure 2.28 show the deformation plot in the measurement area of the GFRP torque-box with 0° fiber orientation in the flanges calculated by the ARAMIS software interface under the 2901 gr and the 5766 gr weight applied at the tip of the box beams, respectively. The displacements of left and right measurement points are displayed in the tables provided in Figure 2.27 and Figure 2.28. The ratio of the applied weight is 1.99. Table 2.5 summarizes the vertical displacements of the left and the right monitor points under applied weights of 2901 gr and 5766 gr. It is seen that increasing the load by 1.987 times resulted in more or less the same the ratio of the vertical displacements of the left and the right measurement points, along with the average of the displacements of the left and right monitor. These results validate the application of the linear theory as well as the correctness of the results obtained by the DIC system.

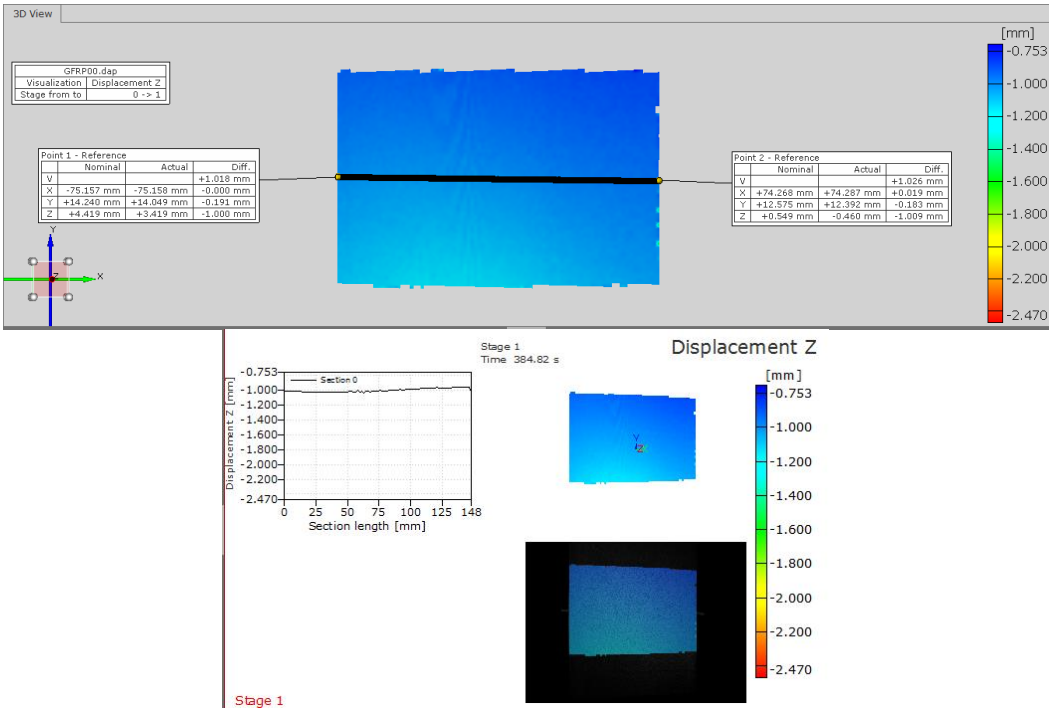

Figure 2.27 Deformation test of GFRP torque-box with 0° fiber angle in the upper and lower flanges – ARAMIS software interface (2901 gr)

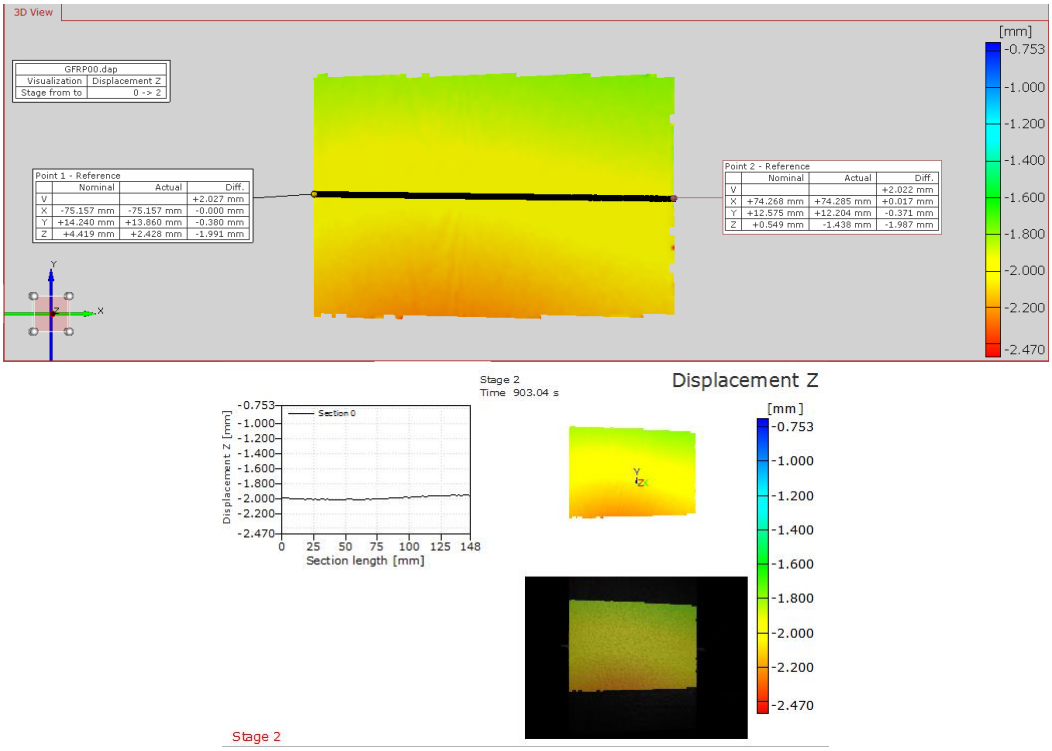

Figure 2.28 Deformation test of GFRP torque-box with 0° fiber angle in the upper and lower flanges – ARAMIS software interface (5766 gr)

Table 2.5 Vertical displacements values of the left and the right monitor points of the GFRP torque-box with 0° fiber orientation under the applied weights of 2901 gr and 5766 gr

Applied Weight (gr)	Displacement of Left Measurement Point (mm)	Displacement of Right Measurement Point (mm)	Average of Displacements of Left and Right Measurement Points (mm)
2901	1.000	1.009	1.005
5766	1.991	1.987	1.989

For the experiments of evaluation of bend-twist coupling potential of box-beam structures, distributed weight of 5766 gr is utilized. Unit twist angle is taken as metric for the assessment of bend-twist coupling potential of torque-boxes. Figure 2.29 displays the lateral displacements at the measurement points given in tables and lateral displacement contours for the GFRP box-beam structures having 15° and 25° fiber orientation angles in the upper and lower flanges for the 5766 gr distributed weight applied symmetrically at the tip location. The local effects due to applied distributed weight are visible in the contour plots. It should be noted that side walls of the box-beam structures that resemble to webs in an actual wind turbine blade act as simple supports which limit the displacements of edges of the structure. Hence, the vicinity of the distributed load application region is more prone to local effect of the applied load in box-beam structures compared to the composite plates. Since the box-beam structures have closed sections, they have much higher stiffness when compared to open section structures yielding less lateral displacement under the load.

Table 2.6 exemplifies the bend-twist coupling potentials of GFRP box-beams having 0°, 15°, and 25° fiber angle orientations in the upper and lower flanges of the box beams. As in the case of plate structures, displacements of the monitor points, twist angle, and the unit twist angle, which is the twist angle per unit lateral displacement of the box beam, increase with increasing fiber angle orientation. In the calculation of the unit twist angle, by using the average value of the displacements of the left and right monitor points, the local effect due to the load application on the unit twist angle calculations is eliminated. According to results, one can conclude that utilizing the 25° fiber orientation angle in the upper and lower flanges of the box-beam structure made

of full GFRP material is more advantageous in terms of acquiring higher bend-twist coupling potential compared to the 15° fiber orientation configuration. It should be noted that for the GFRP plates unit twist angle is also maximized for the fiber angle of 25°.

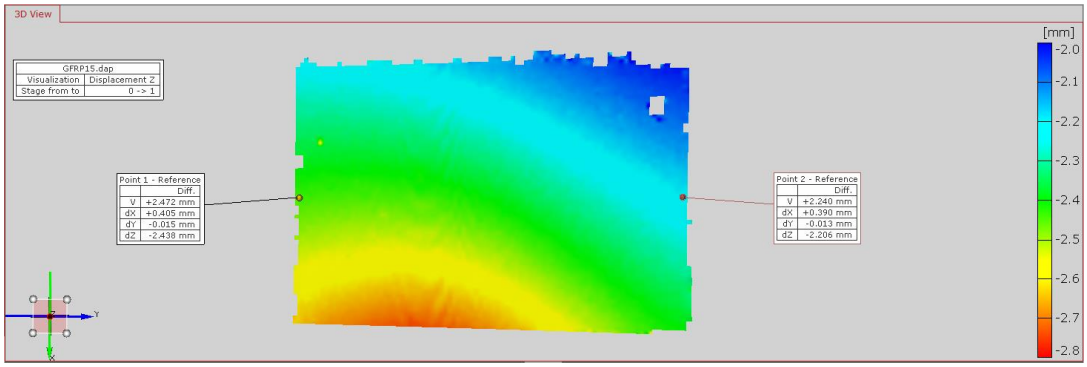

(a)

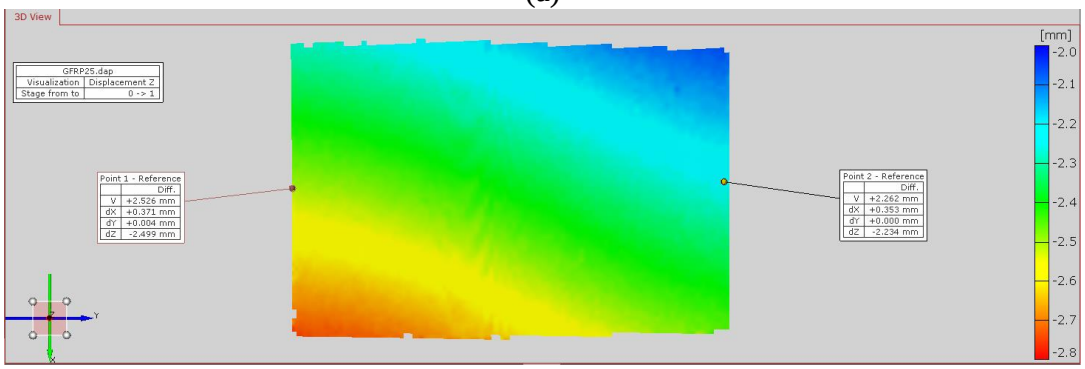

(b)

Figure 2.29 Lateral displacement contours of GFRP box beams calculated by the ARAMIS software / Fiber angle orientations of the upper and lower flanges: (a) 15° and (b) 25°

Table 2.6 Bend-twist coupling potentials of GFRP box-beam structures for different fiber orientation angles

Fiber Orientation Angle (°)	Displacement of Left Measurement Point (mm)	Displacement of Right Measurement Point (mm)	Twist Angle (°)	Unit Twist Angle (°/mm)
0	1.991	1.987	0.002	0.0008
15	2.438	2.206	0.089	0.0382
25	2.499	2.234	0.101	0.0428

The same test setup is configured for the box-beam structures whose upper and lower flanges are made from off-axis unidirectional CFRP layers and side walls are produced from 8-ply symmetric GFRP layup ($[0/90/0/90]_s$). These hybrid structures are named as *CFRP box-beams* in order to distinguish them from full-GFRP torque-boxes. GFRP/CFRP hybrid box-beam structure which has CFRP upper and lower flanges with 25° fiber angle is given in Figure 2.30. In the experiments, a steel block having the weight of 5766 gr is used as the distributed load applied in the same manner as for the GFRP box beams. Figure 2.31 displays the measurement area and the displacements of the left and the right measurement points of CFRP torque-box with 0° fiber orientation calculated by the ARAMIS software under the 5766 gr distributed weight applied at the tip of the box beam. In Figure 2.26, the local effect caused by the applied load can again be observed clearly. For the 0° fiber orientation case, the displacement distribution is symmetric with respect to the beam axis which substantiates the experiment's credibility. However, there is a slight difference between the left and the right measurement points which may have been caused by the misalignment of fibers during the vacuum infusion process, thickness of the paint or slight asymmetry caused during the placement of the weight on the box beam.

Figure 2.30 GFRP/CFRP hybrid box-beam structure having 25° fiber orientation angle in the upper and lower CFRP flanges

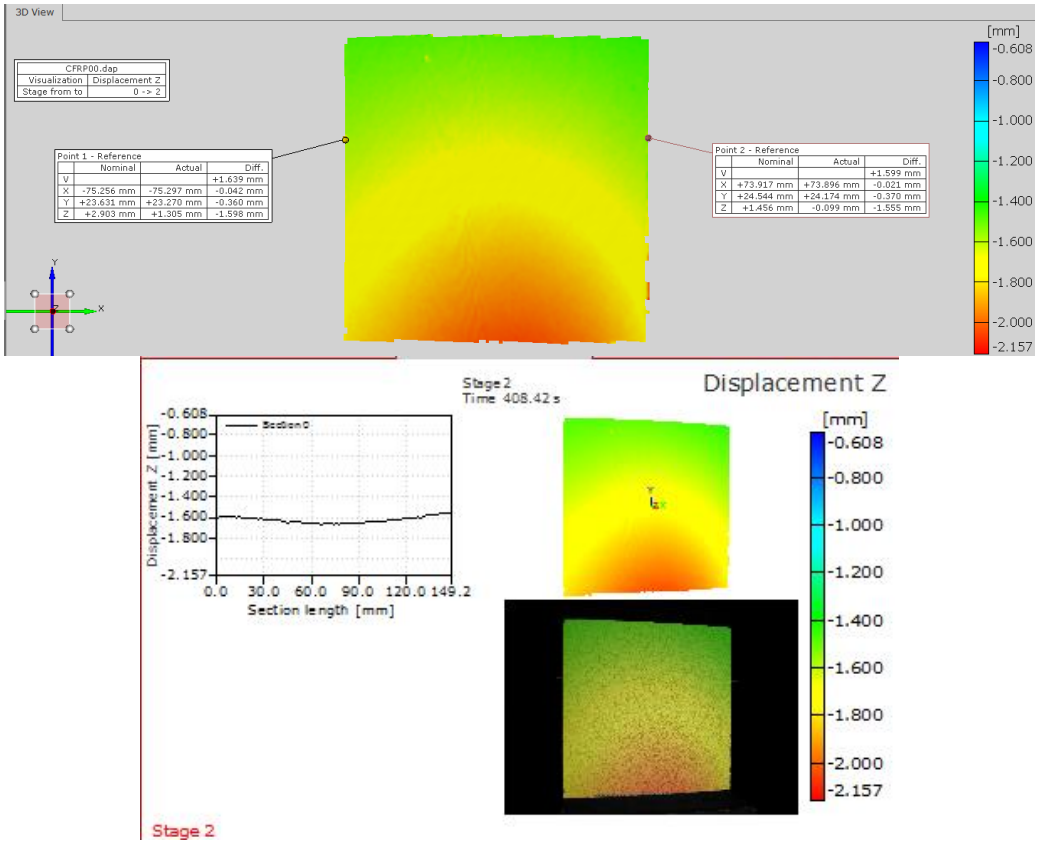

Figure 2.31 Deformation test of the CFRP torque-box with 0° fiber orientation in the upper and lower flanges / ARAMIS software interface

Figure 2.32 presents the lateral displacements at the measurement points in tables and lateral displacement contours for CFRP box-beam structures having 15° and 25° fiber orientation angles with 5766 gr distributed weight applied symmetrically at the tip location. Again, local effects due to the load applied are noticeable in the figures. In the calculations of the unit twist angle, average values of the displacements of left and right monitor points are utilized in order to eliminate the local effects caused by the load and the effect of bending stiffness on the displacements.

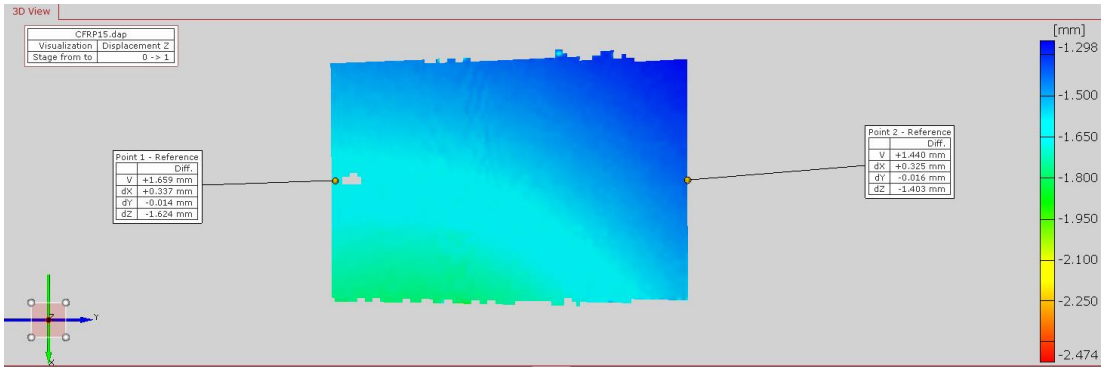

(a)

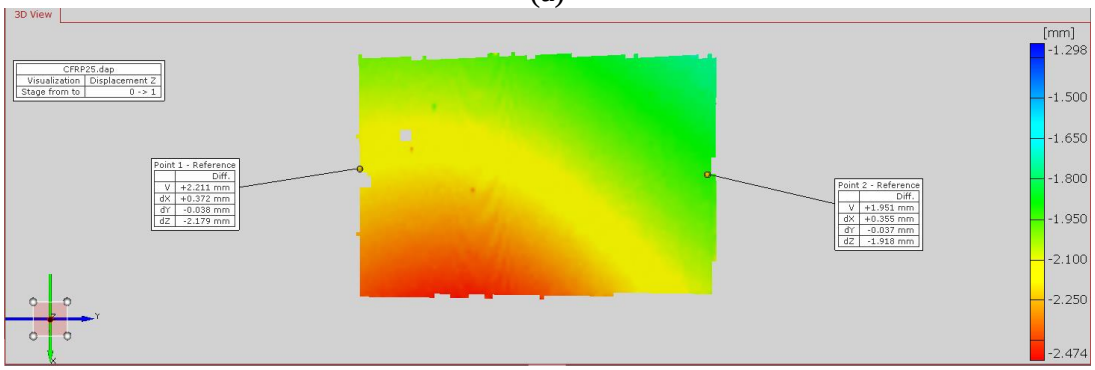

(b)

Figure 2.32 Lateral displacement contours of hybrid GFRP/CFRP box beams calculated by the ARAMIS software / Fiber angle orientations of the upper and lower flanges: (a) 15° and (b) 25°

Table 2.7 gives the bend-twist coupling potentials of CFRP torque-box structures having 0°, 15°, and 25° fiber angle orientations. Although the twist angle increases with increasing fiber orientation angle, the unit twist angle for the CFRP box-beam with 25° fiber angle configuration is about 12.7% lower than that of 15° fiber angle configuration. Again this result is in accordance with the variation of the unit twist angle with the fiber angle for the CFRP plates. The hybrid GFRP-CFRP torque-box produces the optimal bend-twist coupling potential for approximately 15° fiber orientation angle configuration.

Table 2.7 Bend-twist coupling potentials of CFRP box-beam structures for different fiber orientation angles

Fiber Orientation Angle (°)	Displacement of Left Measurement Point (mm)	Displacement of Right Measurement Point (mm)	Twist Angle (°)	Unit Twist Angle (°/mm)
0	1.598	1.553	0.017	0.0109
15	1.624	1.403	0.084	0.0558
25	2.179	1.918	0.100	0.0487

Table 2.8 presents the comparison of bend-twist coupling potentials of GFRP and hybrid GFRP/CFRP torque-boxes having fiber angle orientations of 15° and 25°. The ratio of bend-twist coupling potential is examined by the ratio of unit twist angle of the GFRP and hybrid GFRP/CFRP box-beams. The acquired results show that CFRP box-beam structures have higher bend-twist coupling potential compared to GFRP box-beam structures, however not as high as the CFRP plates. The experimental results obtained on the comparison of the bend-twist coupling potential of GFRP and CFRP materials revealed that CFRP material has higher bend-twist coupling potential than the GFRP material and this could be exploited in load alleviation in wind turbine systems. Superior material properties of CFRP provide sufficient blade stiffness with less number of plies for long blades of larger wind turbines. Furthermore, with its higher bend-twist coupling potential, higher load reductions in the sub-elements of wind turbine system with off-axis CFRP ply placement in the spar cap region can be obtained as compared to the GFRP usage. In Chapter 5 of the thesis, the load reductions achieved in the wind turbine system by bending twisting coupling effect generated by the off-axis use of CFRP and GFRP material in the spar caps of the wind turbine is presented. The experimental study conducted in this chapter showed that CFRP material has higher bend-twist coupling potential than the GFRP material and it can be used in the spar cap regions to provide the necessary blade stiffness as well as load reduction through the bending twisting coupling effect.

Table 2.8 Comparison of bend-twist coupling potentials of GFRP and CFRP box-beam structures

Fiber Orientation Angle (°)	**GFRP Box-Beams**		**CFRP Box-Beams**		**(CFRP/GFRP) Ratio of Unit Twist Angle**
	Twist Angle (°)	**Unit Twist Angle (°/mm)**	**Twist Angle (°)**	**Unit Twist Angle (°/mm)**	
0	0.002	0.0008	0.017	0.0109	-
15	0.089	0.0382	0.084	0.0558	1.46
25	0.101	0.0428	0.100	0.0487	1.14

CHAPTER 3

TESTING OF COMPOSITE MATERIALS

In the present study, composite plates and box beams used for the determination of the bending-twisting coupling potential are made of E-glass/Epoxy and Carbon/Epoxy. Bending-twisting coupling potential of the composite materials utilizing composite plate and box beam tests under bending loads are determined by finite element analysis in Chapter 4 and finite element results are compared with the DIC test results given in Chapter 2. In this chapter, material properties of the composite materials used in the composite plates and box beams are determined by material testing and composite material properties are used in the finite element model in Chapter 4. A composite material which is the combination of a matrix and a reinforcement shows dissimilar material properties due to its constituent content, manufacturing method, and constituent materials. Composite materials are said to be anisotropic materials and their material properties alter in different orthogonal directions, unlike isotropic materials whose material properties do not depend on the orientation. Since there are limitless ways to produce a composite material, material testing is a must in order to fully define the properties. Therefore, a series of tests should be performed to determine the material properties prior to create a finite element model. Throughout the years, testing standards are developed specifically for composite materials so as to ascertain trustworthiness of the determined material properties from tests.

3.1 Tensile Test Specimens

In order to generate a reliable finite element model, properties of composite materials should be determined correctly. For this purpose, standardized test coupons are produced by Yüksel Composite Technologies Inc. All test coupons are made of unidirectional GFRP and CFRP fibers and Biresin CH80-2 resin, and vacuum bagged and cured in room temperature. The constituents are given in Table 2.1. Four different material properties are determined by three different test procedures. The material properties determined by tensile test standards are presented in Table 3.1. Since the finite element model requires out-of-plane properties of composite materials (E_3, G_{13}, G_{23}, ν_{13}, and ν_{23}), several assumptions are made. For unidirectional composite materials, relations given by Eq. 5 and Eq. 6 are assumed to hold.

$$E_2 = E_3,\ \nu_{12} = \nu_{13} \tag{5}$$

$$G_{12} = G_{13} \tag{6}$$

Moreover, it is a known fact that G_{23} has a very close value to in-plane shear modulus; therefore, one can also assume that transverse shear modulus G_{23} is equal to the in-plane shear modulus as stated in Eq. 7.

$$G_{12} = G_{13} = G_{23} \tag{7}$$

Table 3.1 Material properties determined by tensile test procedures

Material Property	Definition	Standard(s) Utilized
E_1	Modulus of elasticity in fiber direction	ASTM D3039 [24]
E_2	Modulus of elasticity in transverse direction	ASTM D3039 [24]
ν_{12}	Poisson's ratio	ASTM D3039 [24]
G_{12}	In-plane shear modulus	DIN EN 6031 [25] ASTM D3518 [26]

The test specimens are produced according to tensile test standards by Yüksel Composite Technologies Inc. For the sake of correctness of the tests, at least five specimens must be tested. Therefore, eight specimens are produced for each test procedure in case of premature failure of the test coupons. Furthermore, tabs are used in specimens in order to successfully introduce the grip force into the coupon, prevent premature failure, and avert gripping damage. Due to the difference in the thicknesses of the tabs and the test coupons, they are produced separately. Table 3.2 and Table 3.3 present the test coupon and tab properties that are produced by Yüksel Composite Technologies Inc., respectively. The tabs are bonded to test coupons using high-elongation adhesive to prevent slippage. Figure 3.1 shows the produced CFRP and GFRP test specimens with bonded tabs.

Table 3.2 Test coupon properties

Material	**Thickness (mm)**	**Fiber Angle (deg.)**	**Dimensions (mm)**	**Test Standard**	**Quantity**
GFRP	1	0	15x250	ASTM 3039	8
GFRP	2	90	25x175	ASTM 3039	8
GFRP	$[45/-45/45/-45]_s$	$[45,-45,45,-45]_s$	25x230	EN 6031	8
CFRP	1	0	15x250	ASTM 3039	8
CFRP	2	90	25x175	ASTM 3039	8
CFRP	$[45/-45/45/-45]_s$	$[45,-45,45,-45]_s$	25x230	EN 6031	8

Table 3.3 Tab properties

Material	**Thickness (mm)**	**Fiber Angle (deg.)**	**Dimensions (mm)**	**Test Standard**	**Quantity**
GFRP	1.5	$[45,-45]_{ns*}$	56x15	ASTM 3039	32
GFRP	1.5	$[45,-45]_{ns*}$	25x25	ASTM 3039	32
GFRP	2	4-ply UD [45/-45/-45/45]	50x25	EN 6031	32
CFRP	1.5	$[45,-45]_{ns*}$	56x15	ASTM 3039	32
CFRP	1.5	$[45,-45]_{ns*}$	25x25	ASTM 3039	32
CFRP	2	4-ply UD [45/-45/-45/45]	50x25	EN 6031	32

**ns:* number of symmetrical stacking

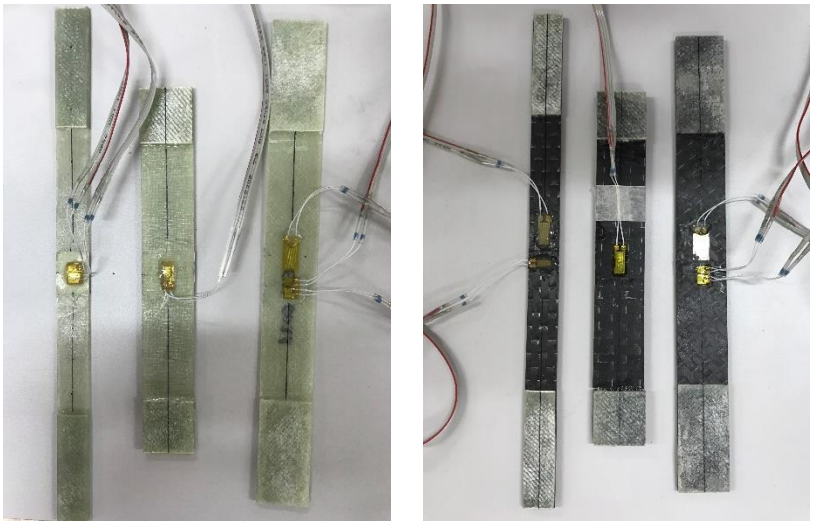

(a) (b)

Figure 3.1 (a) GFRP and (b) GFRP tensile test specimens with bonded tabs (from left to right: 0° UD, ±45°, 90° UD ply placement)

3.2 Test Procedure

For the determination of mechanical properties, MTS High-Force 809 Axial/Torsional Test System [37] which has the capacity of 100 kN/1100 Nm axial/compressive load and torque, respectively is used in the tensile test procedures. Figure 3.2 shows the image of MTS tensile test machine. By using MTS 809 Axial/Torsional Test System, torsion-induced strains are eliminated by keeping the torque at zero. Furthermore, the machine is equipped with hydraulic wedge grips that prevent slipping of the tabs under the applied grip pressure. Strains are measured by applying strain gauges on the specimens and strain data is read from MGCplus amplifier system [38] and transferred to the computer with CATMAN software or are collected with DIC system calibrated specifically for tensile testing. The load and strain data are recorded simultaneously with a sampling rate of five data points per second with the aim of minimum 100 data points per test conducted. Each test requires different strain gauge installation and follows a different procedure. Several tensile tests are also conducted with the aid of the DIC system. The DIC system is used for strain data collection in accordance with the tensile load.

Figure 3.2 MTS High-Force 809 Axial/Torsional Test System

3.2.1 Modulus of Elasticity and Poisson's Ratio Calculation Procedures

For the calculation of Poisson's ratio, modulus of elasticity in fiber direction, and modulus of elasticity in the transverse direction ASTM D3039/D3039M standard is utilized. Specimen dimensions and properties given in Table 3.2 and Table 3.3 are used in order to prepare specimens. Young's modulus in the fiber direction (E_{11}) and the Poisson's ratio for the strain in the transverse direction caused by the stress in the fiber direction (v_{12}) are calculated for GFRP and CFRP materials for tensile test specimens which have 0° unidirectional fiber orientation. Therefore, two strain gauges must be installed with the purpose of measuring strains in the fiber and transverse directions. Figure 3.3 illustrates the strain gauges in the fiber and transverse directions applied on 0° unidirectional GFRP and CFRP tensile test specimens.

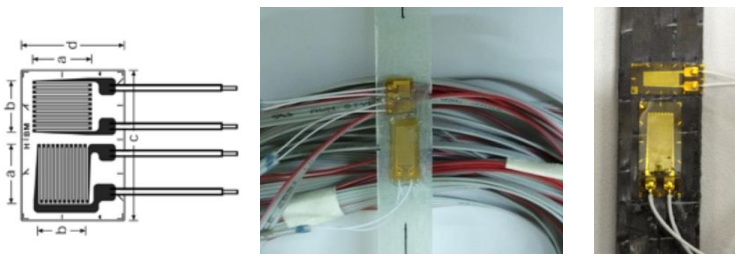

Figure 3.3 Strain gauges in the fiber and transverse directions applied on 0° unidirectional GFRP and CFRP tensile test specimens

Calculation of modulus of elasticity in the transverse direction (E_2) is performed by applying strain gauges which has a 10 mm gage length on GFRP and CFRP specimens which have 90° unidirectional fiber orientation. Figure 3.4 shows the strain gauges having 10 mm gage length applied on 90° unidirectional GFRP and CFRP tensile test specimens.

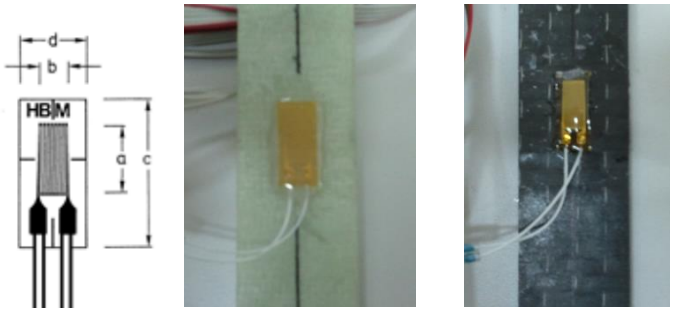

Figure 3.4 Strain gauges in the transverse direction applied on 90° unidirectional GFRP and CFRP tensile test specimens

As a general rule, tensile chord modulus and Poisson's ratio calculations are made in the linear range of stress-strain curve. Plastic region of stress-strain curve should be discarded so as to avoid incorrect calculations of these material properties. ASTM D3039/D3039M standard suggests that the longitudinal strain range to be between 1000 με and 3000 με, where 1000 με is equal to 0.001 actual strain. Constant head speed is set to be 2 mm/min as recommended in ASTM D3039/D3039M. If specimens reach plastic region prior to 3000 με, a proper longitudinal strain range must be determined. Modulus of elasticity in the fiber or in the transverse direction are calculated by Eq. 8.

$$E = \Delta\sigma/\Delta\varepsilon \tag{8}$$

where:

E = modulus of elasticity in the fiber or transverse direction
$\Delta\sigma$ = applied tensile stress difference between two strain points
$\Delta\varepsilon$ = longitudinal strain difference between two strain points

Poisson's ratio is calculated by measuring longitudinal and transverse strain with the same sampling rate. The formula for Poisson's ratio calculation is presented in Eq. 9.

$$\nu_{12} = -\Delta\varepsilon_T/\Delta\varepsilon_L \quad (9)$$

where:

ν_{12} = Poisson's ratio
$\Delta\varepsilon_T$ = transverse strain difference corresponding to two strain points
$\Delta\varepsilon_L$ = longitudinal strain difference between two strain points

3.2.2 In-Plane Shear Modulus Calculation Procedure

In-plane shear modulus (G_{12}) calculations are performed by following the combination of DIN EN 6031 and ASTM D3518 standards. The specimens are produced with the requirements of the DIN EN 6031 standard. Two strain gauges, which are applied on GFRP and CFRP specimens with $[45,-45, 45,-45]_s$ layup configuration, are attached in the tensile load direction and transverse direction to measure the shear strain. Constant head-speed is set to be 1 mm/min until desired maximum load occurs. DIN EN 6031 standard advises the longitudinal strain range to be between 500 με and 2500 με, unless the specimen falls in the plastic region under the applied load corresponding to the strain range defined. Figure 3.5 exemplifies the strain gauges in the fiber and transverse directions applied on $[45,-45, 45,-45]_s$ GFRP and CFRP tensile test specimens.

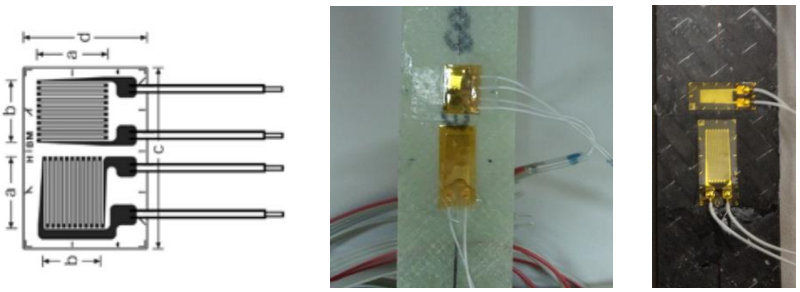

Figure 3.5 Strain gauges in the fiber and transverse directions applied on $[45,-45, 45,-45]_s$ GFRP and CFRP tensile test specimens

Shear stress in the test specimen (τ) can be calculated with Eq. 10

$$\tau = 0.5\frac{P}{wt} \tag{10}$$

where, *P* is the tensile load, *w* and *t* are the average width and thickness measurements per test specimen, respectively. In-plane shear modulus for the preferred elastic longitudinal strain range can be found by dividing shear stress to shear strain as shown in Eq. 11:

$$G_{12} = 0.5\frac{\Delta P}{wt(\Delta\varepsilon_L - \Delta\varepsilon_T)} \tag{11}$$

where,

ΔP = difference in tensile loads between the strain range defined
$\Delta\varepsilon_L$ = longitudinal strain difference between two strain points
$\Delta\varepsilon_T$ = transverse strain difference between two strain points

3.2.3 DIC Material Testing Procedure

In the present study, to cross check the strain gage measurements, several material tests are also performed by using DIC measurement system. GOM ARAMIS 4M (2400x1728 pixel resolution) with adjustable base DIC sensor system in Middle East Technical University Center for Wind Energy (METUWIND) Composite Materials Characterization Laboratory is utilized in the material tests. Since the DIC system is capable of detecting and measuring strains in three dimensions, utilizing the DIC system eliminates the necessity of application of strain gauges; thus, saves time and increases the repeatability of the tests conducted. Five centimeter length of each test specimen is painted with stochastic pattern for DIC system to analyze longitudinal and transverse strains. A set of test specimens which are paint with stochastic pattern is presented in Figure 3.6. For the material testing process, DIC system is calibrated for the measurement area of 65x48 mm, depth of 12 mm with 100 mm lens configuration.

The DIC system is calibrated with using reference points on a *calibration cube* and the image of calibration cube and the calibration process is presented in Figure 3.7. With the calibrated configuration, DIC system is located at 685 mm away from the specimen, providing enough space for MTS tensile test machine to perform safely. Figure 3.8 shows the image of a GFRP specimen under test with the strain measurements done by the DIC system. With this configuration, DIC system and the tensile testing machine are used together in order to obtain load and the strain data.

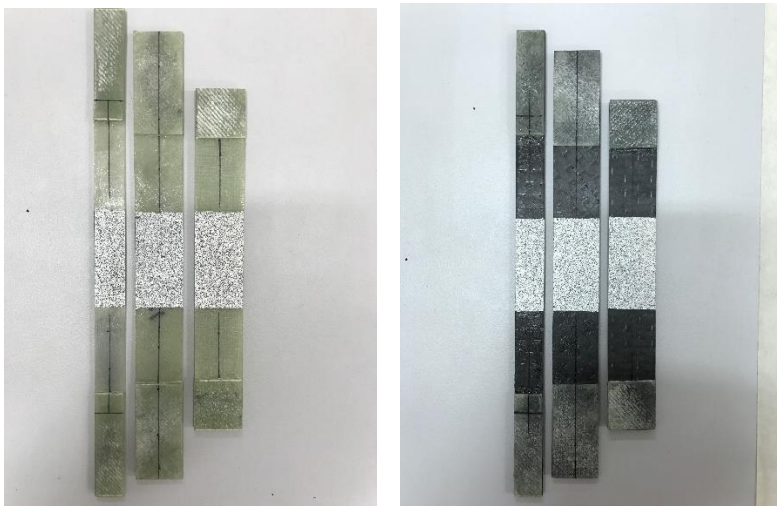

(a) (b)

Figure 3.6 A set of (a) GFRP and (b) CFRP test specimens which are painted with stochastic pattern

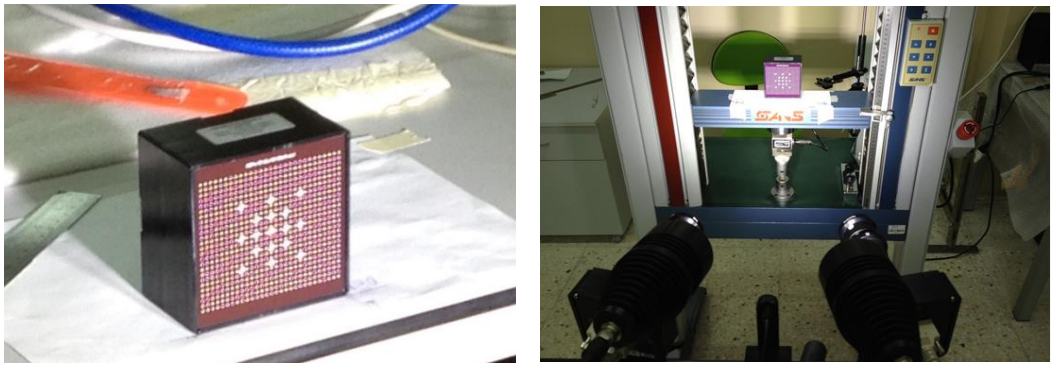

Figure 3.7 Calibration cube and calibration process

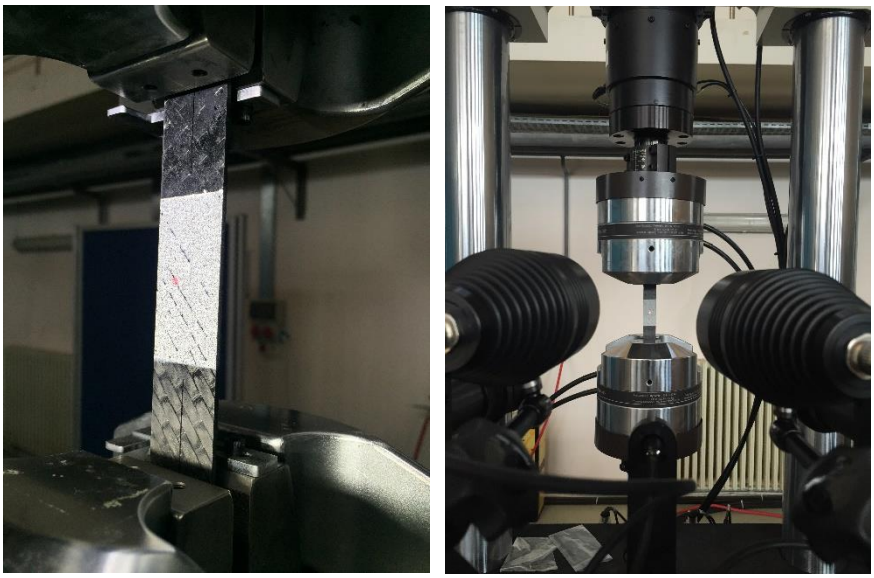

(a) (b)

Figure 3.8 (a) Tensile specimen exposed to DIC cameras and (b) the test setup with DIC system

The sampling rate of the DIC system is matched to that of MTS system which is 6 data points per second in order to interlace the test data. In the measurements performed by the DIC system, due to the condition of the paint and irregularities on the test specimens such as minuscule cavities between fibers, extreme strain values can be acquired. This situation can be overcome by measuring average strain of the whole paint area for each image taken. The elastic properties are then calculated by the load data acquired by the MTS test machine and the strain data acquired from processing of the measurements by the DIC system by the ARAMIS software. The longitudinal and transverse strain data on the stochastic paint surface is evaluated by ARAMIS software. The longitudinal strain contours on the painted surface of a GFRP specimen with $[45,-45, 45,-45]_s$ layup configuration under increasing tensile load for every 50^{th} image are shown in Figure 3.9. The first image is taken under zero load; hence, there is no strain occurrence. As the load is increased via the constant motion of the head, strain develops and it maximizes in the 225^{th} image.

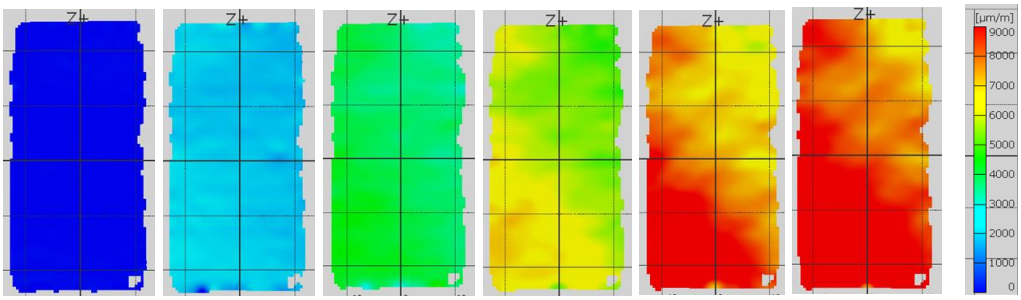

Figure 3.9 Longitudinal strain field of a GFRP specimen with $[45,-45, 45,-45]_s$ layup configuration

3.3 Material Testing

As stated previously, the calculation of elastic properties of GFRP and CFRP materials should be performed in the elastic range as the calculations made in plastic range divert significantly from the actual value. ASTM D3039 standard suggests a longitudinal strain range between 1000 με and 3000 με for determining the modulus of elasticity in fiber direction and the Poisson's ratio. The tests performed showed that the produced test data fall in the elastic range for 0° unidirectional GFRP and CFRP specimens. In order to evaluate the linearity of stress-strain curves, linear trend lines are approximated between the determined strain ranges. Figure 3.10 illustrates the stress-strain curve of a 0° unidirectional GFRP tensile test specimen within the strain limits as proposed by ASTM D3039 standard. The modulus of elasticity in the fiber direction for the strain range of 1000 με and 3000 με (which is equal to 0.001 and 0.003 actual strain) is calculated by using Eq. 8 as 36.88 GPa. In order to evaluate the linearity of the stress-strain curve, a trend line is drawn for the strain range of 0.001 and 0.003 and the slope of curve is found to be 37.04 GPa, with only 0.4% difference.

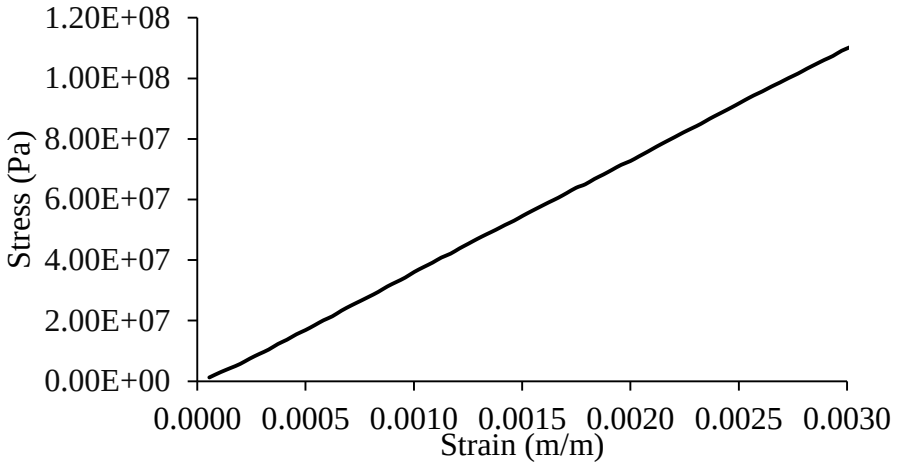

Figure 3.10 Stress-strain curve of a 0° unidirectional GFRP tensile test specimen

Poisson's ratio for the same test specimen is calculated by using Eq. 9 in the same strain range with the utilization of strains in longitudinal and transverse directions and found to be 0.261. In order to evaluate the linearity, longitudinal strain versus time and transverse strain versus time curves are plotted in Figure 3.11. The slopes of the longitudinal and the transverse strain versus time curves are abbreviated as y_L and y_T, respectively. The ratio of slopes of the longitudinal and the transverse strain with respect to time yields the Poisson's ratio and it is found to be 0.261; exactly the same result obtained by using Eq. 9. Consequently, it can be stated that stress-strain curve is linear and the calculations are made in the elastic range.

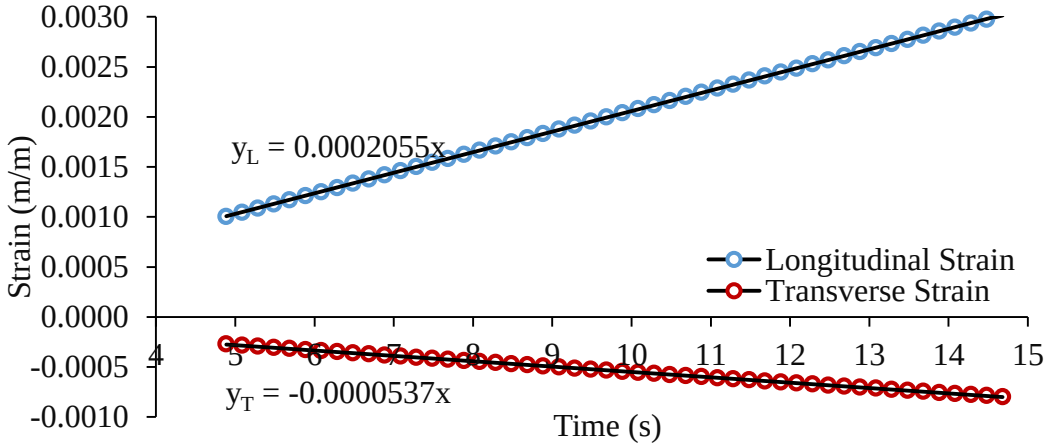

Figure 3.11 Longitudinal and transverse strain data of a 0° unidirectional GFRP tensile test specimen with respect to time

The tests conducted with all 0° unidirectional GFRP and CFRP tensile test specimens produced linear stress-strain curves within the strain range of 1000 με and 3000 με. However, stress-strain curves of 90° unidirectional and shear stress-shear strain curves of ±45° GFRP and CFRP test specimens are nonlinear; thus, calculations of E_2 and G_{12} in the plastic region would be incorrect. Stress-strain curve of a 90° unidirectional GFRP specimen and shear stress-shear strain curve of a ±45° CFRP specimen are presented in Figure 3.12 and Figure 3.13, respectively. For the calculation of modulus of elasticity in the transverse direction for materials that fail below 0.006 actual strain, ASTM D3039 suggests the usage of the strain range of 25 to 50% of the ultimate strain. Likewise, upper limit for the strain range for in-plane shear modulus calculations is defined as 90% of the highest value of shear strain in the initial linear region according to ASTM D3518. Eq. 8-11 are followed through the calculations of E_2 and G_{12}, and strain ranges that are used in the calculations are presented in Table 3.4.

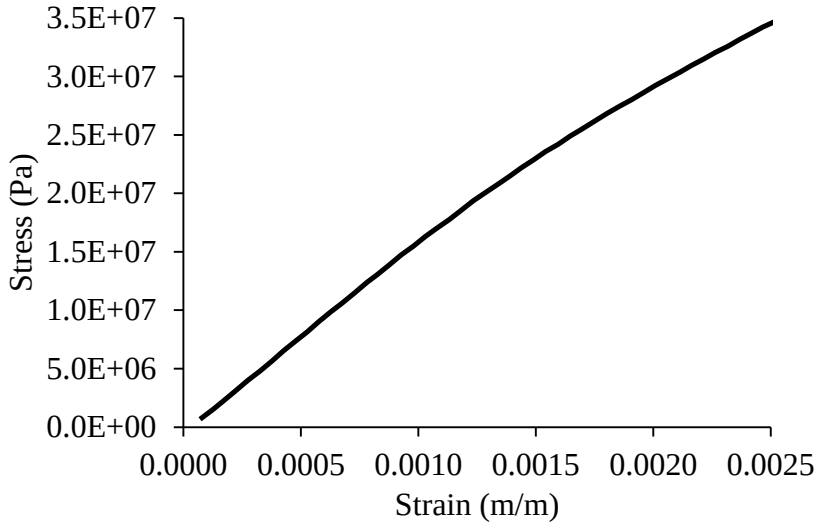

Figure 3.12 Stress-strain curve of a 90° unidirectional GFRP tensile test specimen

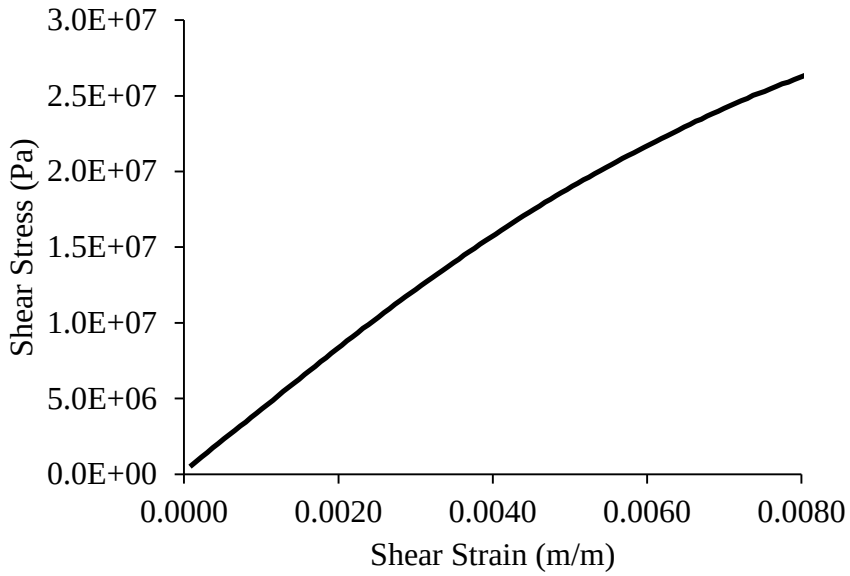

Figure 3.13 Shear stress-shear strain curve of a ±45° CFRP tensile test specimen

Table 3.4 Strain ranges used in the calculations of material properties

Material	Property	Strain Range (με)
0° UD GFRP	E_1, v_{12}	1000 - 3000
90° UD GFRP	E_2	500 - 1000
±45° GFRP	G_{12}	300 - 875
0° UD CFRP	E_1, v_{12}	1000 - 3000
90° UD CFRP	E_2	1000 - 2000
±45° CFRP	G_{12}	500 - 1500

At least five specimens are tested using the appropriate ASTM and DIN EN standards. The test data are evaluated in the specimens' elastic range in order to calculate material properties by using Eq. 8-11. The results attained from each test procedure are averaged in order to obtain a mean value as stated in the standards used. Two of the tests are performed with the aid of the DIC system upon measuring the strains and it is seen that with the DIC system compromising results are obtained as the elastic property measurements done with the strain gauges. Therefore, material properties obtained by the DIC system are also included in the average values. Table 3.5 presents

the Young's modulus in the fiber direction (E_{11}) and the Poisson's ratio values for the strain in the transverse direction caused by the stress in the fiber direction (v_{12}) calculated for six 0° UD GFRP and five 0° UD CFRP test specimens utilizing strain gages (*SG*) and DIC system as strain measurement devices. Modulus of elasticity and Poisson's ratio values are presented as two point difference and trendline values which are obtained by using Eq. 8-11 and drawing best fit lines, respectively. It is worth mentioning that two point difference and trendline values are comparable; which verifies the credibility of the strain range selected for the tests. Furthermore, the properties calculated by using strain gage and DIC systems produce results with a good agreement.

Table 3.5 Young's modulus in the fiber direction and the Poisson's ratio values for 0° UD GFRP and CFRP tensile test specimens

Material	Specimen Name	Strain Measurement Method	E_1 (Pa)		ν_{12}	
			Two Point Difference	Trendline	Two Point Difference	Trendline
0° UD GFRP	N1	SG	3.69E+10	3.70E+10	0.261	0.261
	N2	SG	3.66E+10	3.67E+10	0.258	0.258
	N3	SG	3.76E+10	3.75E+10	0.263	0.263
	N4	SG	3.73E+10	3.72E+10	0.262	0.262
	N5	DIC	3.63E+10	3.62E+10	0.288	0.293
	N6	DIC	3.67E+10	3.68E+10	0.276	0.280
0° UD CFRP	N1	SG	1.09E+11	1.09E+11	0.275	0.276
	N2	SG	9.34E+10	9.35E+10	0.352	0.353
	N3	SG	9.41E+10	9.41E+10	0.241	0.241
	N4	DIC	9.54E+10	9.53E+10	0.309	0.315
	N5	DIC	9.15E+10	9.16E+10	0.281	0.283

Table 3.6 enlists the Young's modulus in the transverse direction (E_2) values for five 90° UD GFRP and five 90° UD CFRP tensile test coupons displayed as two point difference and trendline values. For both GFRP and CFRP coupons, DIC system is used for strain measurements for two of the five specimens.

Likewise, Table 3.7 shows the in-plane shear modulus values for ±45° GFRP and CFRP test specimens presented as two point difference and trendline values. When Table 3.5-Table 3.7 are examined, strain measurements performed with DIC system

and strain gage application produce similar modulus and Poisson's ratio results. These similarities prove the strain measurement capabilities and accuracy of the DIC system; and hence, results obtained with the utilization of DIC system are included in the average results.

Table 3.6 Young's modulus in the transverse direction for 90° UD GFRP and CFRP tensile test specimens

Material	Specimen Name	Strain Measurement Method	E_2 (Pa)	
			Two Point Difference	Trendline
90° UD GFRP	N1	SG	1.62E+10	1.62E+10
	N2	SG	1.56E+10	1.57E+10
	N3	SG	1.67E+10	1.68E+10
	N4	DIC	1.54E+10	1.58E+10
	N5	DIC	1.54E+10	1.53E+10
90° UD CFRP	N1	SG	6.38E+09	6.40E+09
	N2	SG	6.27E+09	6.27E+09
	N3	SG	6.67E+09	6.72E+09
	N4	DIC	6.51E+09	6.44E+09
	N5	DIC	6.36E+09	6.38E+09

Table 3.7 In-plane shear modulus values for ±45° GFRP and CFRP tensile test specimens

Material	Specimen Name	Strain Measurement Method	G_{12} (Pa)	
			Two Point Difference	Trendline
±45° GFRP	N1	SG	5.68E+09	5.63E+09
	N2	SG	5.90E+09	5.91E+09
	N3	SG	6.04E+09	6.06E+09
	N4	SG	5.51E+09	5.48E+09
	N5	DIC	5.56E+09	5.53E+09
	N6	DIC	5.55E+09	5.56E+09
±45° CFRP	N1	SG	4.01E+09	4.02E+09
	N2	SG	4.00E+09	3.99E+09
	N3	SG	3.79E+09	3.79E+09
	N4	SG	3.48E+09	3.48E+09
	N5	DIC	3.54E+09	3.50E+09
	N6	DIC	3.49E+09	3.50E+09

Table 3.8 summarizes the average values of the material properties determined by material tests. It is worth noting that two-point difference values are obtained by Eq. 8-11, whilst trend line values are found by drawing best-fit lines between strain ranges enlisted in Table 3.4. The standards used in tests suggest the use of material properties acquired from two-point data set. Table 3.8 shows that there is negligible difference between the two-point and the trend line calculations. Material properties acquired from the tests are used in defining 3D orthotropic GFRP and CFRP material properties in the finite element models of the composite plate and the box beams in Chapter 4.

Table 3.8 Average values of the material properties determined by material tests

Material	**Property**	**Number of Tests Conducted with Strain Gauges**	**Number of Tests Conducted with DIC System**	**Total Number of Tests**	**Two-Point Difference (Average)**	**Trendline (Average)**
0° UD GFRP	E_1 (GPa)	4	2	6	36.90	36.91
	ν_{12}				0.27	0.27
90° UD GFRP	E_2 (GPa)	3	2	5	15.87	15.94
±45° GFRP	G_{12} (GPa)	4	2	6	5.71	5.69
0° UD CFRP	E_1 (GPa)	3	2	5	96.76	96.78
	ν_{12}				0.29	0.29
90° UD CFRP	E_2 (GPa)	3	2	5	6.44	6.44
±45° CFRP	G_{12} (GPa)	4	2	6	3.72	3.72

CHAPTER 4

FINITE ELEMENT ANALYSIS OF COMPOSITE PLATE AND BOX-BEAM STRUCTURES

In this chapter, results of the experiments performed on the determination of the bend-twist coupling potential of composite plate and box beam structures with the DIC method are compared with the finite element analysis results of these structures. In these analyses, orthotropic material properties acquired with the material tests described in Chapter 3 are used in the finite element models so as to model the structures as precise as possible. The plates and box-beam structures are modeled and analyzed in MSC PATRAN/NASTRAN software by using shell elements. The information acquired in finite element analyses and DIC experiments of structures with different materials and fiber orientations form a basis for designing bend-twist coupled blades for the wind turbine system with the aim of reduction in fatigue loads. Relative differences of unit twist angles of composite plates and torque-boxes obtained from experiments and finite element analyses are compared in order to comprehend the change in unit twist angle due to fiber angle configuration.

4.1 Finite Element Model of Composite Plates and Box-Beam Structures

4.1.1 Finite Element Model of Composite Plates

The finite element models of composite plates are generated in accordance with the actual produced composite plates. The plates which are manufactured from GFRP and

CFRP materials have fiber orientation angles of 0°, 10°, 15°, 20°, and 25° having dimensions of 50 cm in length and 15 cm in width. Figure 4.1 shows the dimensions of modeled GFRP and CFRP plates. Due to irregularities on the surfaces of the plates, the thicknesses are calculated by weighing the plates and making use of the fiber-volume ratio determined by thermogravimetric analyses (*TGA*). The calculated thicknesses of GFRP plates are 1.58 mm for each fiber orientation configuration. On the other hand, the calculated thicknesses of CFRP plates vary significantly; 2.77 mm, 2.86 mm, 2.92 mm, 2.94 mm, and 3.02 mm for plates with fiber orientations of 0°, 10°, 15°, 20°, and 25°, respectively.

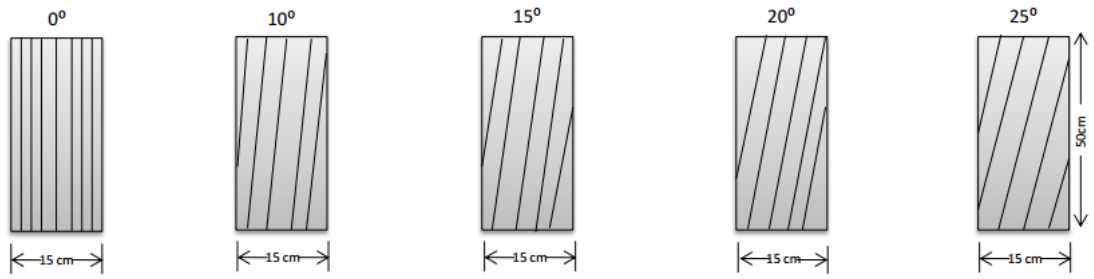

Figure 4.1 Dimensions of modeled composite plates

In finite element models, GFRP and CFRP plates are clamped 10 cm at the root and distributed load is applied on the 30.3x14.8 mm portion at the tip location that simulate the weight applied in the experiments. For GFRP plates, 1.039 N (105.95 gr) load is applied at the tip location as in the experiments. For CFRP plates, 4.239 N (432.084 gr) load is applied due to superior stiffness properties and higher thickness values. In order to evaluate the bend-twist coupling potential, the displacements of the left and right measurement points are determined at a distance of 5 cm from the tip of the plate with the intention of eliminating the local effects. The displacements are calculated at the left and right edge of the plate. Figure 4.2 presents the finite element model created in PATRAN software, left and right measurement points, and the applied load location of composite plates.

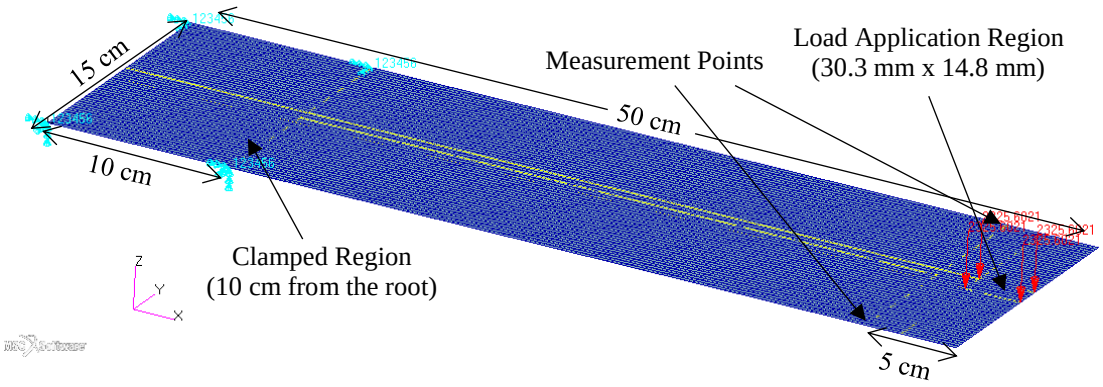

Figure 4.2 Finite element model of composite plates

The effect of fiber orientation on the bending stiffness and bend-twist coupling can be understood from the stress-strain relation of composite materials. The relation between stress and strain for unidirectional orthotropic material can be written as Eq. 12:

$$\{\sigma\} = [Q]\{\varepsilon\} \tag{12}$$

where, Q is the reduced stiffness matrix. Expanding Eq. 12 by neglecting out-of-plane terms yields Eq. 13:

$$\begin{Bmatrix}\sigma_1\\ \sigma_2\\ \sigma_6\end{Bmatrix} = \begin{bmatrix}Q_{11} & Q_{12} & 0\\ Q_{12} & Q_{22} & 0\\ 0 & 0 & Q_{66}\end{bmatrix}\begin{Bmatrix}\varepsilon_1\\ \varepsilon_2\\ \varepsilon_6\end{Bmatrix} \tag{13}$$

where;

$$Q_{11} = \frac{E_1^2}{E_1 - \nu_{12}E_2}, \qquad Q_{12} = \frac{\nu_{12}E_1E_2}{E_1 - \nu_{12}^2E_2}$$
$$Q_{22} = \frac{E_1E_2}{E_1 - \nu_{12}^2E_2}, \qquad Q_{66} = G_{12} \tag{14}$$

For unidirectional composite materials that have fiber orientation angle φ, transformed reduced stiffness matrix $\bar{Q}$ is utilized. Equation 15 presents the stress-strain relation for unidirectional composite materials that have fiber orientation angle φ.

$$\begin{Bmatrix}\sigma_1\\ \sigma_2\\ \sigma_6\end{Bmatrix}=\begin{bmatrix}\overline{Q}_{11} & \overline{Q}_{12} & \overline{Q}_{16}\\ \overline{Q}_{12} & \overline{Q}_{22} & \overline{Q}_{26}\\ \overline{Q}_{16} & \overline{Q}_{26} & \overline{Q}_{66}\end{bmatrix}\begin{Bmatrix}\varepsilon_1\\ \varepsilon_2\\ \varepsilon_6\end{Bmatrix} \quad (15)$$

In Eq. 15, $\overline{Q}_{11}$ term is the transformed axial stiffness and $\overline{Q}_{16}$ is the transformed coupling stiffness term. At the laminate level, bending-twisting coupling coefficients D_{16} or D_{26} depend on the coupling stiffness terms $\overline{Q}_{16}$ or $\overline{Q}_{26}$ linearly. Likewise, at the laminate level, bending stiffness coefficients D_{11} or D_{22} depend on the transformed axial stiffness $\overline{Q}_{11}$ or $\overline{Q}_{22}$ linearly. Transformed axial stiffness and coupling stiffness terms are expressed in terms of the reduced stiffness terms and the fiber orientation angle φ in Equation 16.

$$\begin{aligned}\bar{Q}_{11} &= Q_{11}cos^4\varphi+2(Q_{12}+2Q_{66})cos^2\varphi sin^2\varphi+Q_{22}sin^4\varphi\\ \bar{Q}_{16} &= (Q_{11}-Q_{12}-2Q_{66})\,cos^3\,\varphi\,sin\,\varphi-(Q_{22}-Q_{12}-2Q_{66})\,cos\,\varphi\,sin^3\,\varphi\end{aligned} \quad (16)$$

Figure 4.3 illustrates the transformed reduced axial stiffness ($\overline{Q}_{11}$) and coupling stiffness ($\overline{Q}_{16}$) terms stiffness terms of GFRP and CFRP materials with respect to the fiber orientation angle. The material properties that are used in Eq. 13 are determined with material tests and withdrawn from Table 3.8. For both GFRP and CFRP materials, $\overline{Q}_{11}$ reduces with increasing fiber angle. For a unidirectional CFRP laminate with 25° fiber angle, about 30% reduction in the $\overline{Q}_{11}$ occurs when compared to 0° fiber angle configuration. For a GFRP laminate, this reduction is only limited by 20%. However, there is a great upsurge in the $\overline{Q}_{16}$ coupling stiffness term for the CFRP material compared to the GFRP material with the increasing fiber angle. As a matter of fact, $\overline{Q}_{16}$ term for CFRP material with 25° fiber orientation configuration is four times greater than GFRP material with same fiber orientation configuration.

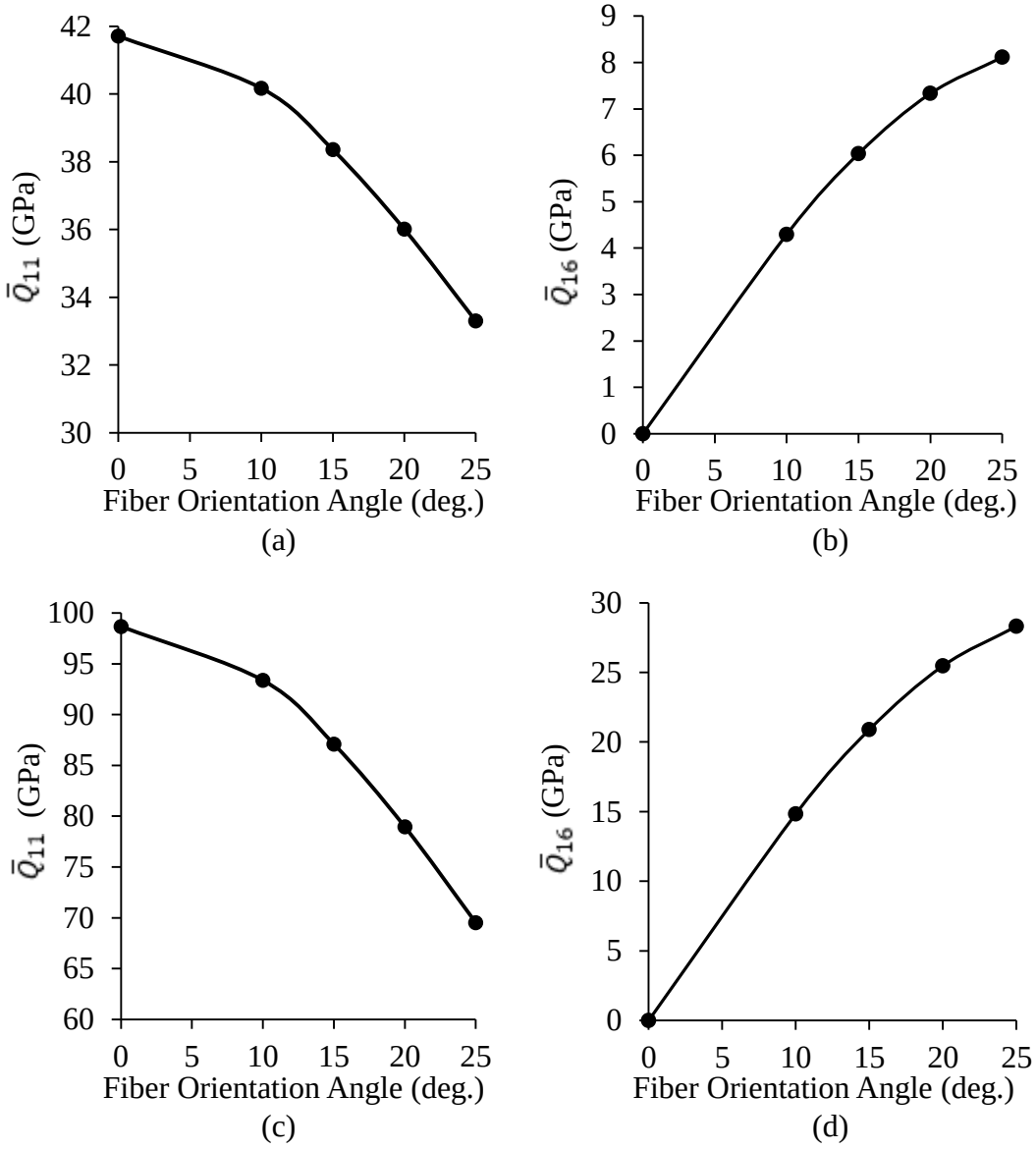

Figure 4.3 Transformed reduced axial and coupling stiffness terms of (a), (b) GFRP, and (c), (d) CFRP materials with respect to fiber orientation angle

Resultant equations in Eq. 17 can be constructed for the relation between moments and strains with the application of Classical Lamination Theory (*CLT*) based on Kirchhoff hypothesis and the assumption of perfect bonding between layers for thin laminates.

$$\begin{Bmatrix} M_x \\ M_y \\ M_{xy} \end{Bmatrix} = \begin{bmatrix} B_{11} & B_{12} & B_{16} \\ B_{12} & B_{22} & B_{26} \\ B_{16} & B_{26} & B_{66} \end{bmatrix} \begin{Bmatrix} \varepsilon_x^0 \\ \varepsilon_y^0 \\ \varepsilon_{xy}^0 \end{Bmatrix} + \begin{bmatrix} D_{11} & D_{12} & D_{16} \\ D_{12} & D_{22} & D_{26} \\ D_{16} & D_{26} & D_{66} \end{bmatrix} \begin{Bmatrix} \kappa_x \\ \kappa_y \\ \kappa_{xy} \end{Bmatrix} \quad (17)$$

where, M_x, M_y, and M_{xy} are resultant moments acting on the plate, ε_x^0, ε_y^0, and ε_{xy}^0 are strains, κ_{xy} is twisting curvature, and κ_x and κ_y are curvatures about the principal axes. Moreover, B_{ij} and D_{ij} are coupling stiffness and bending stiffness terms, respectively. These terms can be calculated from Eq. 18:

$$B_{ij} = \frac{1}{2}\sum_{k=1}^{N} \left(\bar{Q}_{ij}\right)_k (h_k^2 - h_{k-1}^2)$$
$$D_{ij} = \frac{1}{3}\sum_{k=1}^{N} \left(\bar{Q}_{ij}\right)_k (h_k^3 - h_{k-1}^3) \quad (18)$$

where, h_k is the vectorial distance from the mid-plane of the plate to the upper surface of the k^{th} laminate. For a symmetric stacking sequence, there is no coupling between the in-plane loads and out of plane deformations; therefore, B_{ij} terms vanish and Eq. 17 reduces to Eq. 19.

$$\begin{Bmatrix} M_x \\ M_y \\ M_{xy} \end{Bmatrix} = \begin{bmatrix} D_{11} & D_{12} & D_{16} \\ D_{12} & D_{22} & D_{26} \\ D_{16} & D_{26} & D_{66} \end{bmatrix} \begin{Bmatrix} \kappa_x \\ \kappa_y \\ \kappa_{xy} \end{Bmatrix} = [D] \begin{Bmatrix} \kappa_x \\ \kappa_y \\ \kappa_{xy} \end{Bmatrix} \quad (19)$$

In order to investigate the effect of bending moment on the twisting curvature, strain-resultant relation in Eq. 20 can be constructed with appropriate matrix operations:

$$\begin{Bmatrix} \kappa_x \\ \kappa_y \\ \kappa_{xy} \end{Bmatrix} = \begin{bmatrix} d_{11} & d_{12} & d_{16} \\ d_{12} & d_{22} & d_{26} \\ d_{16} & d_{26} & d_{66} \end{bmatrix} \begin{Bmatrix} M_x \\ M_y \\ M_{xy} \end{Bmatrix} \quad (20)$$

Under pure bending moment (M_y, $M_{xy}=0$) twisting curvature is dependent on only d_{16} compliance term and the magnitude of the moment as shown in Eq. 21.

$$\kappa_{xy} = d_{16} M_x \tag{21}$$

Figure 4.4 shows the variation of the compliance of coupling stiffness term (d_{16}) with fiber orientation angle for GFRP and CFRP materials. For both materials the compliance of the coupling stiffness term increases for increasing fiber orientation angle; however, the rate of increment slows down for fiber angles greater than 20°. Furthermore, the compliance of the coupling stiffness term of CFRP material is about 2.5 times higher than that of GFRP material. This implies that the plate which is made of CFRP plies is more prone to twist due to the bending than GFRP plate, as Eq. 21 suggests.

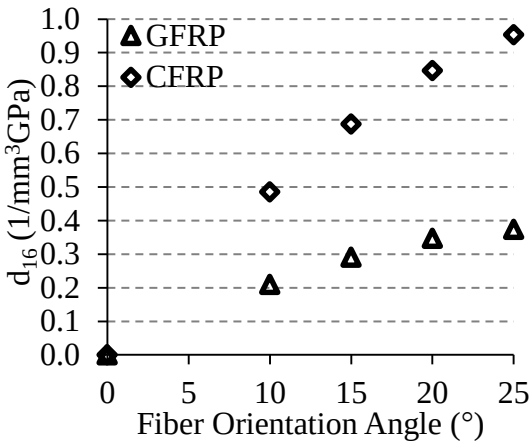

Figure 4.4 Variation of the compliance of the coupling stiffness term (d_{16}) with fiber orientation angle

Accuracy of the finite element analyses highly depend on the selected mesh size. Accuracy of the solution can be increased by imposing fine mesh; however, it comes with a cost of computational time. Therefore, mesh convergence is studied to successfully balance the accuracy of the solution as well as computational time. According to the mesh convergence studied for plates and box-beam structures, quad mesh size for plates is selected to be 2.5 mm whereas quad mesh size for torque-boxes is selected to be 5 mm. Figure 4.5 presents the displacement contours of GFRP plates having 0°, 10°, 15°, 20°, and 25° fiber angle orientations as a result of finite element analyses. As the fiber orientation angle increases, the angle between displacement

contours and plate axis increases due to the amplified displacement difference between left and right edges of plates.

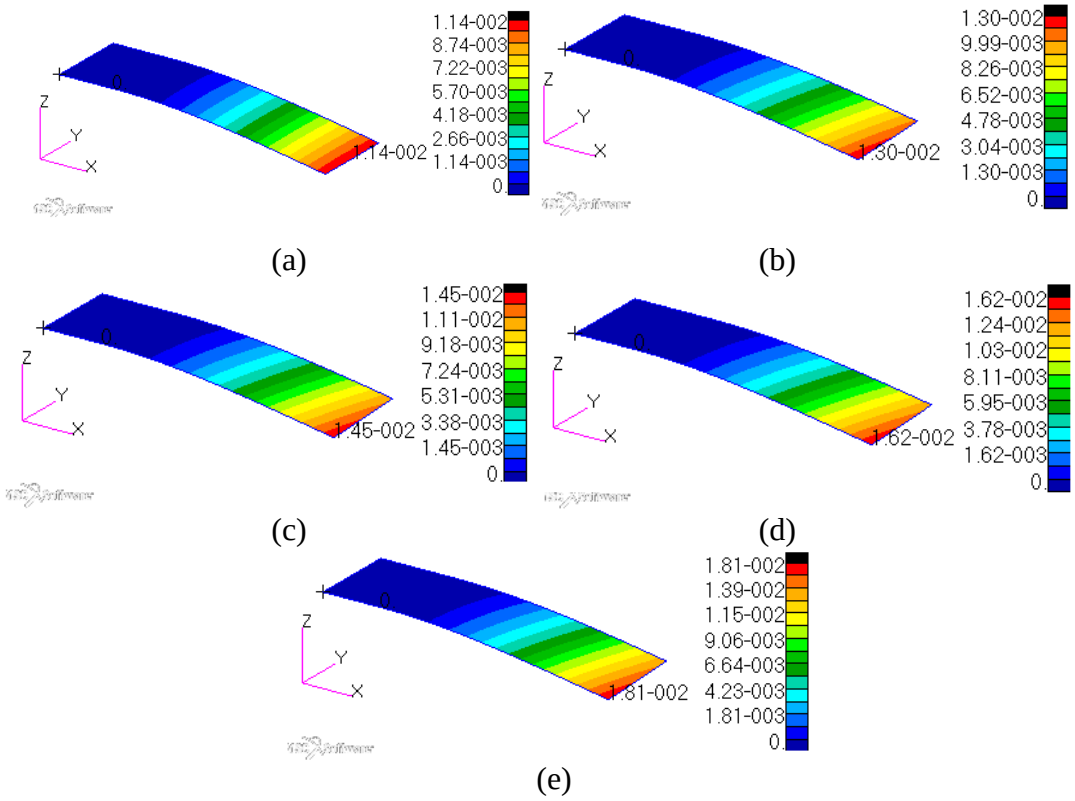

Figure 4.5 Displacement contours of GFRP plates having (a) 0°, (b) 10°, (c) 15°, (d) 20°, and (e) 25° fiber angle orientations

Table 4.1 gives the bend-twist coupling potentials of GFRP plates having fiber angles of 0°, 10°, 15°, 20°, and 25° obtained by finite element analyses. It is seen that the displacements of the left and the right measurement points, as well as the twist angle increase with the increasing fiber angle. However, unit twist angle, which is normalized by the mean value of displacements of left and right measurement points, grows up to 20° fiber orientation angle and reduces slightly for 25° fiber angle configuration. The reason for this phenomenon is that the rate of increase of the compliance of the coupling stiffness term reduces for fiber angles greater than 20°, as Figure 4.4 suggests. Whilst bending stiffness reduces, bend-twist coupling stiffness

does not increase at the same pace, resulting in increased twist angle with decreased unit twist angle result for 25° fiber angle configuration.

Table 4.1 Bend-twist coupling potentials of GFRP plates for different fiber orientation angles

Fiber Orientation Angle (°)	Displacement of Left Measurement Point (mm)	Displacement of Right Measurement Point (mm)	Twist Angle (°)	Unit Twist Angle (°/mm)
0	9.22	9.22	0	0
10	10.72	9.26	0.559	0.0560
15	11.93	9.88	0.785	0.0720
20	13.35	10.86	0.951	0.0786
25	14.89	12.16	1.046	0.0774

Figure 4.6 displays the displacement contours of CFRP plates having 0°, 10°, 15°, 20°, and 25° fiber angle orientations as a result of finite element analyses.

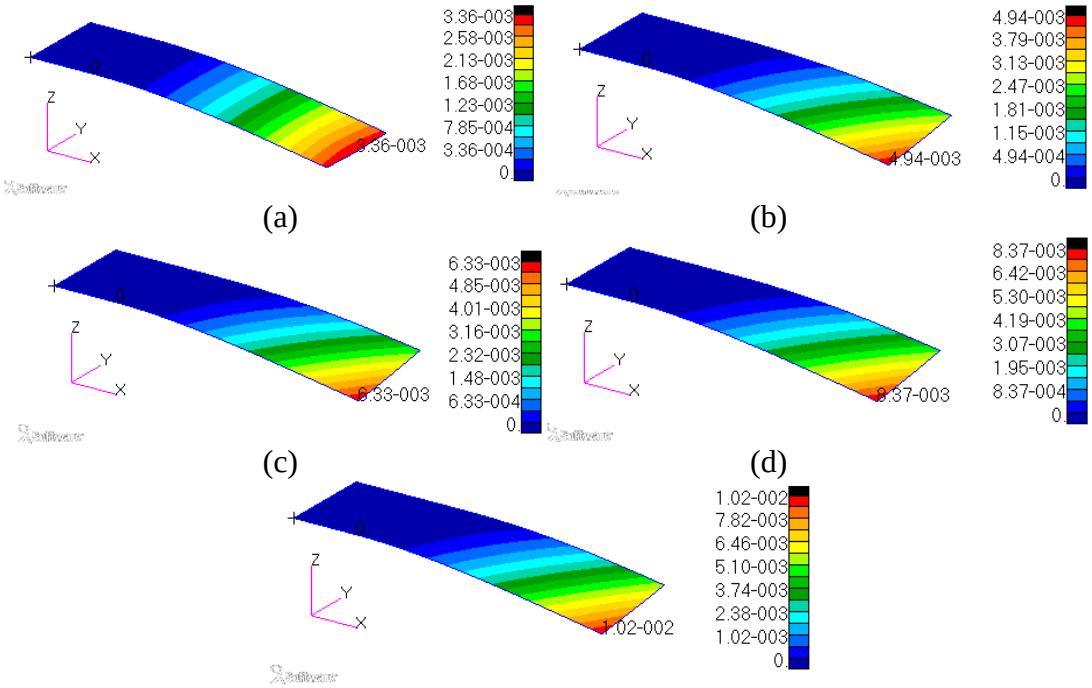

Figure 4.6 Displacement contours of CFRP plates having (a) 0°, (b) 10°, (c) 15°, (d) 20°, and (e) 25° fiber angle orientations

Table 4.2 shows the bend-twist coupling potentials of CFRP plates with fiber orientation angles of 0°, 10°, 15°, 20°, and 25°. Once more, displacements of the left and right measurement points, and the twist angle increases substantially with increasing fiber orientation angle. Conversely, unit twist angle, which is the bend-twist coupling potential criterion, decreases for fiber angle orientation greater than 15°. Although the twist angle increases with increasing fiber angle, unit twist angle decreases due to reduced bending stiffness and decreased rate of increase of bend-twist coupling stiffness.

Table 4.2 Bend-twist coupling potentials of CFRP plates for different fiber orientation angles

Fiber Orientation Angle (°)	Displacement of Left Measurement Point (mm)	Displacement of Right Measurement Point (mm)	Twist Angle (°)	Unit Twist Angle (°/mm)
0	2.66	2.66	0	0
10	4.11	2.31	0.688	0.2145
15	5.23	2.72	0.961	0.2418
20	6.92	3.68	1.240	0.2340
25	8.47	4.82	1.395	0.2099

4.1.2 Finite Element Model of Composite Box-Beam Structures

The torque-boxes that are modeled in MSC. PATRAN have the dimensions of 100 cm x 15 cm x 5 cm with upper and lower flanges having 0°, 15°, and 25° fiber orientation angles with respect to the beam axis. Figure 4.7 illustrates the properties and dimensions of box-beam structures that are modeled and produced. Upper and lower flanges are modeled with 8 unidirectional plies with a total laminate thickness of 1.264 mm thickness for the full-GFRP box beams and with a total laminate thickness of 2.32 mm thickness for the hybrid GFRP and CFRP box beams. Side walls that resemble to spar webs in actual wind turbine blades have 8 plies of GFRP material with $[0/90]_s$ symmetrical layup for all torque-box configurations so as to observe the effect of off-axis plies in the flanges on the bend-twist coupling potential.

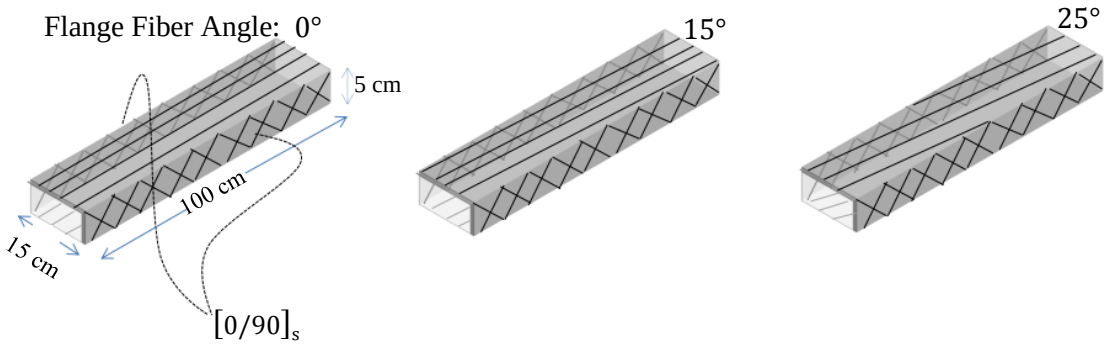

Figure 4.7 Properties and dimensions of box-beam structures

Figure 4.8 shows the box-beam structure modeled in MSC. PATRAN software by linear shell elements with four nodes. In the finite element model, box-beam is clamped for a distance of 10 cm from the root of the box-beam and the 56.56 N (5766 gr) distributed load is applied at the 10 cm x 15 cm portion of the tip section, as shown in

Figure 4.8. In the finite element analyses, the displacements of the left and right edges are measured 20 cm away from the tip in order to eliminate the local effects as practiced in the experiments.

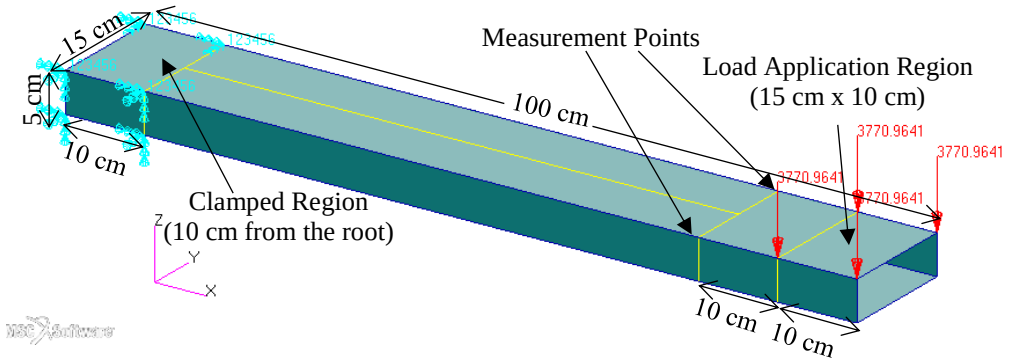

Figure 4.8 Finite element model of box-beam structures

Figure 4.9 demonstrates the displacement contours of torque-boxes that have GFRP flanges with fiber angle orientations of 0°, 15°, and 25°. Although slight local effect

due to the load applied is present in the vicinity of the measurement points, it does not have huge influence on the bend-twist coupling potentials. As in the case of composite plates, the angle between displacement contours and beam axis surges with the increasing fiber angles of flanges.

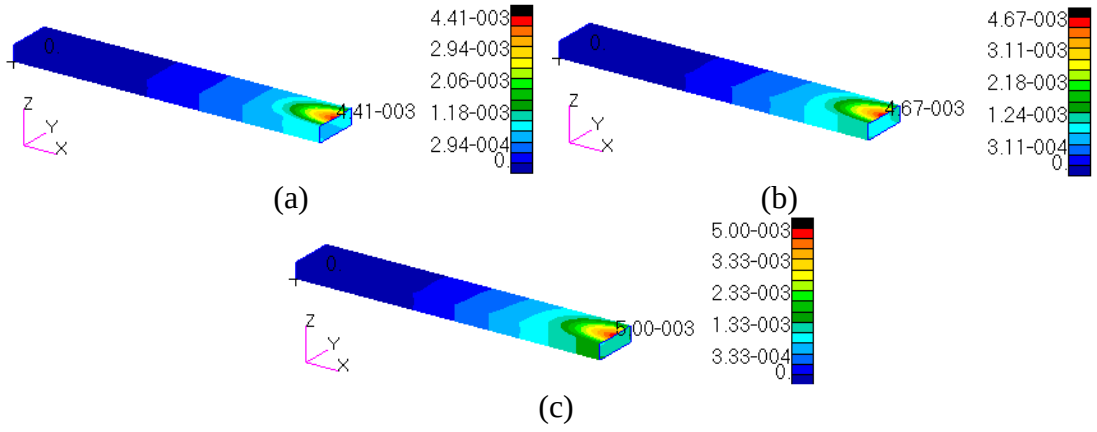

Figure 4.9 Displacement contours of torque-boxes that have GFRP flanges with fiber angle orientations of (a) 0°, (b) 15°, and (c) 25°

Table 4.3 shows the left and right measurement point displacements, twist angles, and unit twist angles for torque-boxes that have GFRP material in the flanges for different fiber orientations. With increasing fiber angle, displacements of left and right measurement points, twist angle, and unit twist angle increases. The displacements and twist angles are much smaller for torque-box structures when compared to plates because of higher stiffness on account of closed section and greater inertia due to the side walls and separation of upper and lower flanges.

Table 4.3 Bend-twist coupling potentials of GFRP box-beam structures for different fiber orientation angles

Fiber Orientation Angle (°)	**Displacement of Left Measurement Point (mm)**	**Displacement of Right Measurement Point (mm)**	**Twist Angle (°)**	**Unit Twist Angle (°/mm)**
0	0.999	0.999	0	0
15	1.261	1.126	0.051	0.0431
25	1.556	1.378	0.068	0.0464

Figure 4.10 illustrates the displacement contours of box-beam structures that have CFRP flanges and GFRP webs with fiber angle orientations of 0°, 15°, and 25°. As stated previously, these hybrid structures are named as *CFRP box-beams* so as to differentiate them from full-GFRP box-beam structures.

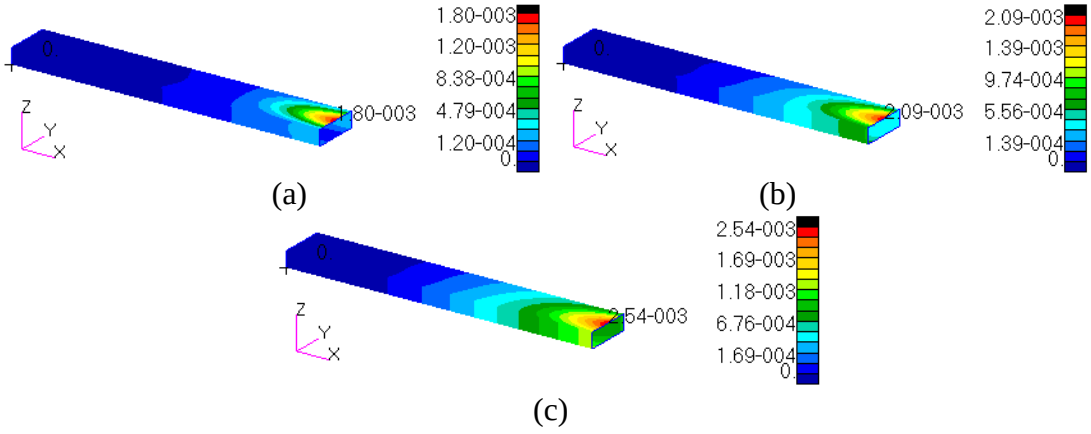

Figure 4.10 Displacement contours of box-beam structures that have CFRP flanges and GFRP webs with fiber angle orientations of (a) 0°, (b) 15°, and (c) 25°

Figure 4.11 shows the loaded case of a CFRP torque-box with fiber angle orientation of 25°. If a hypothetical line is drawn between the left and right measurement points, even though local effects due to applied load are still existent at the measurement points, the angle between the displacement contours and beam axis are perceptible. Due to this difference, left measurement point deflects more than the right one, resulting induced twist due to bending for off-axis ply placement configuration.

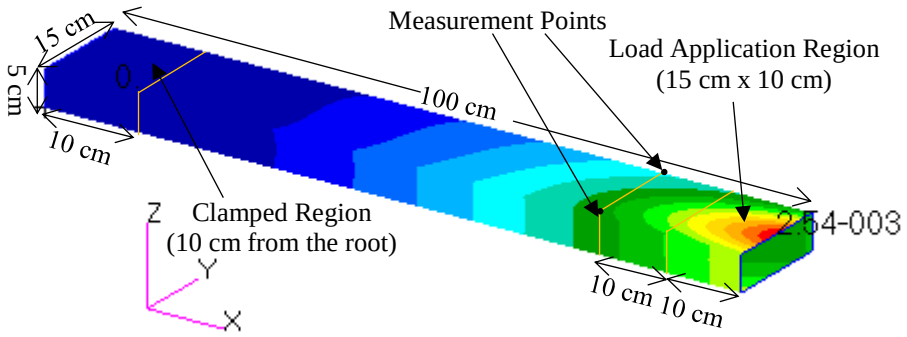

Figure 4.11 The loaded case of a CFRP torque-box with fiber angle orientation of 25° calculated with finite element analysis

Displacements of the left and the right measurement points, twist angles, and unit twist angles for CFRP torque-boxes with different fiber orientation angles under the applied distributed load are presented in Table 4.4. Despite the fact that displacements are small, the unit twist angles of hybrid CFRP box-beams are more than twice as high as the unit twist angles of GFRP box-beam for the same fiber angle. This is an indication of the higher bending twisting coupling potential of CFRP material compared to the GFRP material. Additionally, as fiber angle increases from 15° to 25°, the structure loses it bend-twist coupling potential according finite element analyses.

Table 4.4 Bend-twist coupling potentials of CFRP box-beam structures for different fiber orientation angles

Fiber Orientation Angle (°)	Displacement of Left Measurement Point (mm)	Displacement of Right Measurement Point (mm)	Twist Angle (°)	Unit Twist Angle (°/mm)
0	0.292	0.292	0	0
15	0.674	0.467	0.079	0.1382
25	1.123	0.828	0.111	0.1141

4.1.3 Comparison of Experiments and Finite Element Analyses

The finite element models of plates and box-beams are created with the purpose of comparing the bend-twist coupling potentials with the results of the DIC experiments.

The plates and torque box structures are modeled according to the actual structures produced and material properties determined from tensile tests are used in finite element analyses. Figure 4.12 and Figure 4.13 present the comparison of unit twist angles obtained by experiments via DIC method and finite element analyses with respect to the fiber angle orientation of GFRP and CFRP plates and box-beam structures, respectively. As Figure 4.12 suggests, Finite Element Method (FEM) and experiments conducted with DIC method produce compromising results with similar trends within 10% discrepancy. However, especially for hybrid GFRP-CFRP torque-boxes, unit twist angles determined by DIC measurements and finite element analyses differ more than 50% error. There are several reasons for such discrepancy. First of all, tensile and compressive properties for composite structures are actually different but in the finite element analyses tensile moduli are used. In the bending loading, certain parts of the plates and box structures are under compression and normally compressive elastic moduli have to be used in these zones. In this work, since compressive tests are not performed, elastic properties acquired from tensile tests are taken as mean values. The elastic properties are changed in a range of ±10% so as to impose compressive effects on the composite materials defined in the finite element models with the purpose of achieving results as close as results obtained experimentally via DIC system utilization. Secondly, due to the fiber-volume fraction unpredictability of materials, effective thicknesses that are used in FE models may be erroneous. Another reason for such a discrepancy arouse is that fiber angle definition in finite element models is definitive whereas in plates and torque-boxes that are produced may differ from the actual value mainly due to the vacuum infusion process. At several local regions, the fiber angle orientation of the structures may present different value from the intended ones because of manufacturing defects and vacuum infusion. Such a local defect can be seen in Figure 4.14 inside of a hybrid GFRP-CFRP box-beam with 25° fiber orientation angle. The results obtained from experiments and finite elements may show variance due to the local defects. It is mentioned that elastic properties are dependent on fiber angle definition and since ±10% margin is imposed on elastic moduli values, fiber angle values remained unchanged in this study. Lastly,

since the displacements of left and right measurement points are very small, slight change in reading of these displacements creates huge differences in unit twist angles.

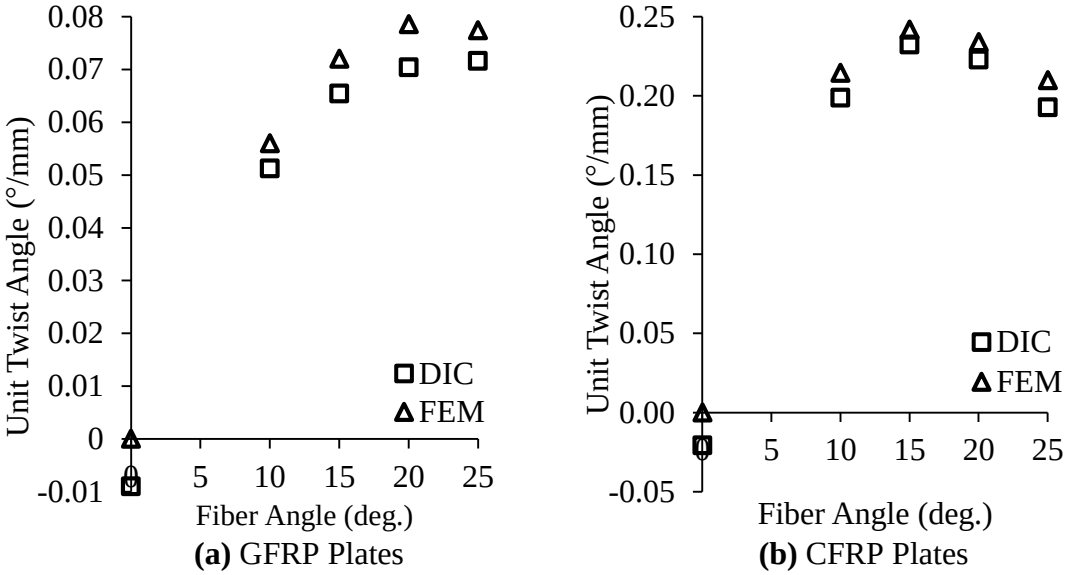

Figure 4.12 Comparison of unit twist angles obtained by experiments with DIC method and finite element analyses with respect to fiber angle orientation for (a) GFRP (b) CFRP plates

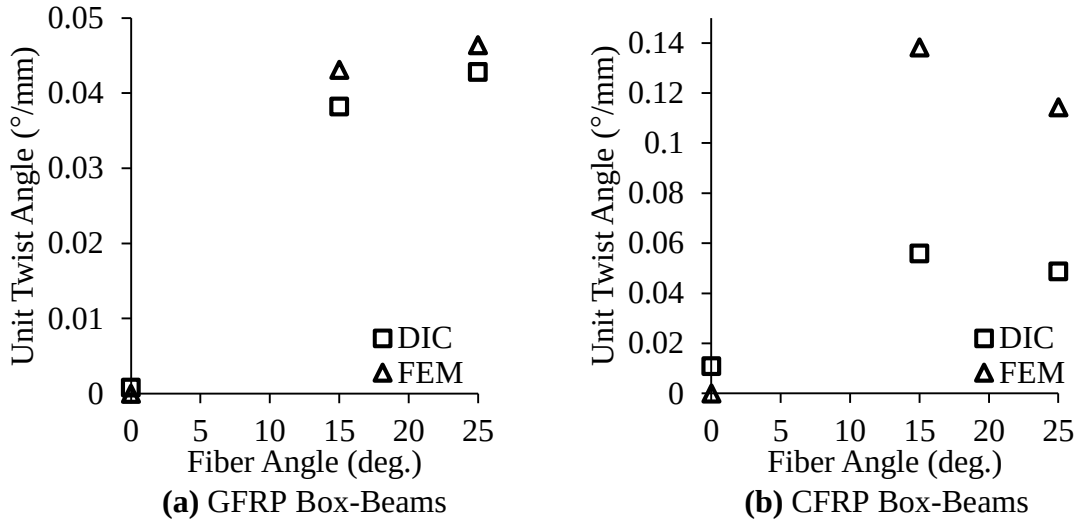

Figure 4.13 Comparison of unit twist angles obtained by experiments with DIC method and finite element analyses with respect to fiber angle orientation for (a) GFRP (b) CFRP box-beam structures

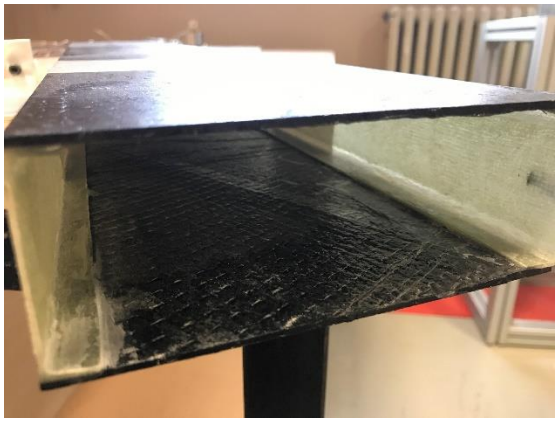

Figure 4.14 Local defect on a hybrid GFRP-CFRP box-beam with 25° fiber orientation angle

This situation can be best observed from the comparison of DIC and FEM results of twist angles and unit twist angles of GFRP plates given in Table 4.5. Although the twist angles determined from DIC measurements and finite element analyses are close to each other, the discrepancy becomes higher for unit twist angles. The reason of this increase can be understood by inspecting Eq. 4. The unit twist angle is calculated by dividing the twist angle by mean value of left and right measurement point displacements. Therefore, a small change in left and right displacements measured by the DIC method and the FEM causes substantial difference in unit twist angle calculation. Additionally, since the displacements are very small, slight difference in displacements changes the unit twist angle considerably.

Table 4.5 Comparison of DIC and FEM results of twist angles and unit twist angles of GFRP plates

Fiber Angle (°)	**DIC Results**		**FEM Results**		**Percent Difference of Twist Angle (%)**	**Percent Difference of Unit Twist Angle (%)**
	Twist Angle (°)	**Unit Twist Angle (°/mm)**	**Twist Angle (°)**	**Unit Twist Angle (°/mm)**		
0	-0.094	-0.0090	0	0	*NA*	*NA*
10	0.591	0.0512	0.559	0.0560	5.41	9.38
15	0.789	0.0654	0.785	0.0720	0.51	10.10
20	0.935	0.0704	0.951	0.0786	1.71	11.65
25	1.077	0.0716	1.046	0.0774	2.88	8.09

As stated previously, there is a strong possibility that bend-twist coupling potentials acquired from experiments and finite element analyses differ due to:

- material properties obtained from tensile tests. For composite materials, it is a well-known fact that tensile and compressive properties vary. Since compression occurs due to bending in experiments performed on plates and box-beam structures, about 10% change in material properties is envisaged.
- fiber-volume fraction unpredictability. The manufacturer provided 45% fiber-volume fraction in composite plates and box-beam structures as a rough value. Thus, difference in fiber-volume fraction alters the effective thickness that is used in finite element analysis. Therefore, 3% fudge factor in thickness is predicted.
- local fiber angle alteration due to vacuum infusion process and manufacturing flaws.

In order to overcome these impreciseness, optimum values of E_1, E_2, G_{12}, ν_{12}, and thicknesses of plates and torque-box structures are to be found. The main goal of this comparison procedure is to find the optimal material properties and thicknesses in the specified interval. Material properties obtained by material tests and thicknesses calculated are taken as the nominal values and an iterative optimization study is conducted by varying the material properties of the composite material properties and thicknesses of composite materials used in the composite plates. The objective of this study is to minimize the difference between the finite element results and DIC measurements in the determining the bending twisting coupling potential of composite plates. To accomplish this aim, a MATLAB code is written with the purpose of finding the optimum values by searching discontinuous intervals. The code changes the material properties and thicknesses (E_1, E_2, G_{12}, ν_{12}, and t) for each fiber orientation configuration by calling a Nastran input file (.bdf), sends the modified .bdf file for analysis in NASTRAN solver, acquires new left and right measurement point displacements, calculates new unit twist angle, and calculates the difference between the DIC measurement and finite element calculation. The error function of this discrete

range search in the j^{th} step for the optimum properties is defined as the summation of the absolute differences of unit twist angles determined by finite element analyses with altered properties and unit twist angles determined by the DIC system for fiber orientation angles of 10°, 15°, 20°, and 25°, as shown in Eq. 22. In Eq. 22, absolute differences of unit twist angles for corresponding fiber angle orientation φ obtained from experiments with DIC system and finite element analyses are summed and error function (E) is generated. The properties that give the lowest value of the error function are kept and discrete optimization process is repeated by halving or reducing the search interval initiated at the point that gives the lowest error in which the optimal solution is being searched for. The process is continued until no more reduction in absolute unit twist angle difference occurred by halving the search interval. Due to the inaccuracies described heretofore, material properties which are determined from material test campaign are varied in a range of ±10% with respect to their nominal values, whilst thicknesses are varied in a range of ±3% with respect to the nominal thicknesses calculated based on the measured fiber volume fractions and plate masses. Figure 4.15 shows the flow chart of the optimization scheme that is used for the determination of the optimum properties for GFRP and CFRP materials. It should be noted that iterative optimization process is applied only for composite plates since they are simple geometrically and do not have the inaccuracies associated with the manufacturing of the box beam structures.

$$E_j = \sum_{i=1}^{4} \left| \hat{\theta}(\varphi_i)_{DIC} - \hat{\theta}(\varphi_i)_{FEM} \right|_j , \qquad \varphi_i = 5(i+1) \tag{22}$$

The results for material properties gathered by carrying out the iterative optimization process for the GFRP and the CFRP plates are presented in Table 4.6 and Table 4.7, respectively. It is worth to mention once again that the thickness of each CFRP plate differs for varying fiber angle configuration. Therefore, thickness results are not presented in Table 4.7, however; 3% reduction in thickness for each CFRP plate is deemed suitable.

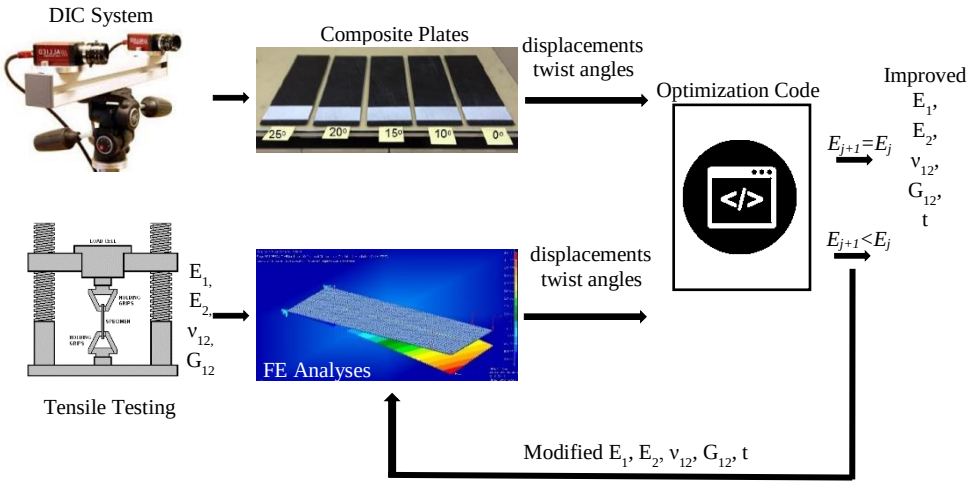

Figure 4.15 The flow chart of the optimization scheme

Table 4.6 Properties of GFRP material obtained by the iterative optimization process and material testing

Property	Iterative Optimization Process	Material Test	Ratio
E_1 (GPa)	33.579	36.900	0.91
ν_{12}	0.284	0.268	1.06
G_{12} (GPa)	5.534	5.705	0.97
E_2 (GPa)	16.028	15.869	1.01
t (mm)	1.564	1.580	0.99

Table 4.7 Properties of CFRP material obtained by the iterative optimization process and material testing

Property	Iterative Optimization Process	Material Test	Ratio
E_1 (GPa)	89.540	96.800	0.925
ν_{12}	0.274	0.292	0.94
G_{12} (GPa)	3.718	3.718	1.00
E_2 (GPa)	7.083	6.439	1.10

Comparisons of bend-twist coupling potentials acquired by the DIC method and finite element analyses with the usage of optimized properties of GFRP and CFRP plates are presented in Table 4.8 and Table 4.9, respectively. As shown in Table 4.5, unit twist angle values obtained from finite element analyses with material properties obtained

from tensile testing cause a difference of approximately 10% which is improved substantially by using the material properties obtained from the iterative optimization process. The unit twist angles obtained from finite element analyses with the improved material properties and thicknesses produce compromising results as the in the for 9 out of 10 plates, differences in the unit twist angles are within 2% of the unit twist angles determined by the DIC system. By amending material properties in a small interval, substantial reduction in bend-twist coupling inaccuracy between experiments and finite element analyses is accomplished.

Table 4.8 Comparison of bend-twist coupling potentials of GFRP plates / DIC method / FEA results with material properties from material tests / FEA results with material properties from iterative optimization process

Fiber Angle (°)	**Unit Twist Angle, DIC Results (°/mm)**	**Unit Twist Angle, FEA Results[1] (°/mm)**	**Unit Twist Angle, FEA Results (Improved)[2] (°/mm)**	**Error of Unit Twist Angle (%)**	**Error of Unit Twist Angle (Improved) (%)**
0	-0.0092	0	0	*NA*	*NA*
10	0.0513	0.0560	0.0505	9.38	1.59
15	0.0652	0.0720	0.0653	10.10	0.12
20	0.0704	0.0786	0.0716	11.65	1.66
25	0.0716	0.0774	0.0707	8.09	1.23

[1] FEA results using material properties from material tests
[2] FEA results using material properties from iterative optimization process

Table 4.9 Comparison of bend-twist coupling potentials of CFRP plates / DIC method / FEA results using material properties from material tests / FEA results using material properties from iterative optimization process

Fiber Angle (°)	**Unit Twist Angle, DIC Results (°/mm)**	**Unit Twist Angle, FEA Results[1] (°/mm)**	**Unit Twist Angle, FEA Results (Improved)[2] (°/mm)**	**Error of Unit Twist Angle (%)**	**Error of Unit Twist Angle (Improved) (%)**
0	-0.0209	0	0	*NA*	*NA*
10	0.1988	0.2145	0.2026	7.89	1.93
15	0.2324	0.2418	0.2296	4.08	1.21
20	0.2229	0.2340	0.2228	4.99	0.05
25	0.1926	0.2099	0.2001	9.01	3.87

[1] FEA results using material properties from material tests
[2] FEA results using material properties from iterative optimization process

Figure 4.16 shows the comparison of unit twist angles obtained by experiments via DIC method and finite element analyses with the utilization of improved material properties with respect to the fiber angle orientation of GFRP and CFRP plates. Although the difference in the results between experiments and finite element analyses with material properties determined from tensile tests are acceptable, as Figure 4.16 suggests, the unit twist angles obtained by experiment and finite element analyses with the improved material properties are very close to each other for both GFRP and CFRP plates.

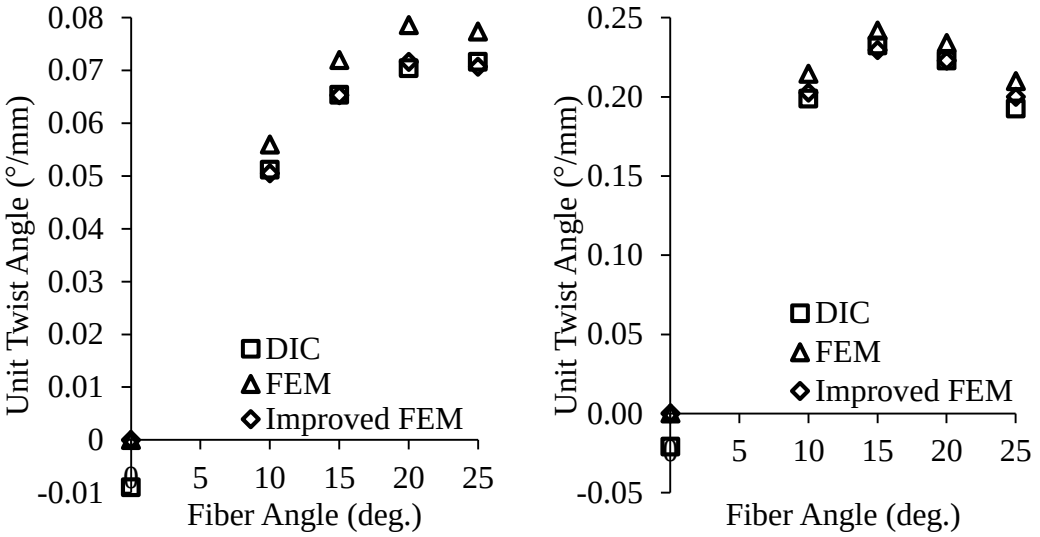

(a) GFRP Plates **(b)** CFRP Plates

Figure 4.16 Comparison of unit twist angles obtained by experiments with DIC method and finite element analyses with improved material properties with respect to fiber angle orientation for (a) GFRP (b) CFRP plates

Table 4.8 and Table 4.9 show that percent errors of unit twist angles are truncated. Nevertheless, evaluation of the bend-twist coupling potentials qualitatively rather than quantitatively is the main objective of this specific work. That is to say, relative percentage differences of unit twist angles of composite plates and torque-boxes obtained from experiments and finite element analyses are compared in order to comprehend the change in unit twist angle due to fiber angle configuration. For this

purpose, the error function (γ) can be defined as the percentage of relative differences of bend-twist coupling potentials determined by the DIC method and the finite element analyses as depicted in Eq. 23,

$$\gamma = \left| \frac{\hat{\theta}_2^{DIC} - \hat{\theta}_1^{DIC}}{\hat{\theta}_1^{DIC}} - \frac{\hat{\theta}_2^{FEM} - \hat{\theta}_1^{FEM}}{\hat{\theta}_1^{FEM}} \right| \tag{23}$$

where, $\hat{\theta}_1^{DIC}$ and $\hat{\theta}_2^{DIC}$ are the unit twist angles determined by the DIC method for fiber orientation angles φ_1 and φ_2 for the case $\varphi_2 > \varphi_1$, respectively. Correspondingly, $\hat{\theta}_1^{FEM}$ and $\hat{\theta}_2^{FEM}$ are the unit twist angles determined by finite element analyses for fiber orientation angles φ_1 and φ_2. With this function, relative errors for different fiber orientation angles are exposed as well as accounting the behavior of unit twist angle with respect to fiber orientation. The percentage of relative differences of bend-twist coupling potentials acquired by the DIC method and the finite element analyses with improved properties, that is; the comparison of rate of change of unit twist angles of finite element model with respect to experiments for GFRP and CFRP plates are given in Table 4.10 by using Eq. 23. Once more, the relative errors are far below than 5% and the finite element model with improved properties efficaciously validates the experiments conducted with DIC monitoring system for composite plates in terms of bend-twist coupling potentials and rate of change of unit twist angles.

Table 4.10 The percentage of relative differences of unit twist angles acquired by the DIC method and the finite element analyses with improved properties

Fiber Angle, φ_1 (°)	**Fiber Angle, φ_2 (°)**	**Relative Error, GFRP Plates, γ (%)**	**Relative Error, CFRP Plates, γ (%)**
10	15	2.20	3.59
10	20	4.54	2.17
10	25	0.51	1.85
15	20	1.67	1.12
15	25	1.48	4.26
20	25	0.46	3.39

The improvement of material properties process is scripted for composite plates. Therefore, the material properties of the GFRP and the CFRP material and thicknesses of the plates are optimized for plates only and they are assumed be valid for composite box-beams. The new finite element models of the box-beams are generated with improved material properties and effective thicknesses. The relative percentage difference of unit twist angles, hence; comparison of the rate of change of bend-twist coupling potentials determined by finite element analyses with the improved properties and experiments are made for GFRP and hybrid GFRP-CFRP torque boxes. Table 4.11 and Table 4.12 show the unit twist angle values determined from experiments with the DIC method and finite element analyses by using material properties from test data and improved properties for GFRP and hybrid GFRP-CFRP torque-boxes, respectively.

Table 4.11 Unit twist angle values obtained from experiments with the DIC method and the finite element analyses for GFRP box-beams

Fiber Angle (°)	**Unit Twist Angle, DIC Results (°/mm)**	**Unit Twist Angle, FEA Results[1] (°/mm)**	**Unit Twist Angle, FEA Results (Improved)[2] (°/mm)**
0	0.0008	0	0
15	0.0382	0.0431	0.0390
25	0.0428	0.0464	0.0423

[1] FEA results using material properties from material tests
[2] FEA results using material properties from iterative optimization process

Table 4.12 Unit twist angle values obtained from experiments with the DIC method and the finite element analyses for hybrid GFRP-CFRP box-beams

Fiber Angle (°)	**Unit Twist Angle, DIC Results (°/mm)**	**Unit Twist Angle, FEA Results[1] (°/mm)**	**Unit Twist Angle, FEA Results (Improved)[2] (°/mm)**
0	0.0109	0	0
15	0.0558	0.1382	0.1309
25	0.0487	0.1141	0.1090

[1] FEA results using material properties from material tests
[2] FEA results using material properties from iterative optimization process

Table 4.11 shows that unit twist angles obtained from finite element analyses, utilizing the material properties obtained from material tests, significantly deviate from the experimental values for GFRP box-beams. With the improved properties of the GFRP material obtained by the iterative optimization process, finite element analyses produce comparable results with the experiments performed by the DIC system. Thus, selection of material properties by the iterative optimization of composite plates also works for GFRP box-beam structures. However, there are still noteworthy differences between unit twist angle values determined by finite element analyses utilizing the material properties via the iterative optimization process and the DIC experiments, as Table 4.12 suggests. Although the improved material property usage decreases the differences by a small amount, the discrepancies between the finite element results and the DIC test results are still high. This situation can be explained by investigating the twist angle and unit twist angle values. Table 4.13 gives the twist angle and unit twist angle values determined by the DIC experiments and finite element analyses with optimum material properties for the hybrid GFRP and CFRP box-beams. It is noticed that although the differences between the twist angles are small, the discrepancies between the unit twist angles are considerably high. This is due to the mean displacement value given in Eq. 4. Since the deformation of the hybrid GFRP-CFRP box-beams is very small due to the high stiffness of CFRP flanges, small changes in the displacements cause large variances in the unit twist angles. Consequently, relative errors defined in Eq. 23 are examined for the comment on the success of the iterative optimization process performed. Table 4.14 gives the comparison of relative errors determined by the finite element analyses utilizing the material properties obtained from material tests and from the iterative optimization process with respect to the experimental results obtained the for full-GFRP and the hybrid GFRP-CFRP box-beams. With the usage of improved material properties in the finite element models, approximately 1% reduction in relative errors is achieved. For the box-beams, with the finite element analysis the rate of change of the unit twist angle with the fiber orientation angle is obtained within 4% difference with respect to experimental results.

Table 4.13 Twist angle and unit twist angle determined by experiments and finite element analyses with optimum material properties for hybrid GFRP and CFRP box-beams

Fiber Angle (°)	DIC Results		FEA (Improved) Results	
	Twist Angle (°)	Unit Twist Angle (°/mm)	Twist Angle (°)	Unit Twist Angle (°/mm)
0	0.0172	0.0109	0	0
15	0.0844	0.0558	0.0785	0.1309
25	0.0997	0.0487	0.1100	0.1090

Table 4.14 Comparison of relative errors of finite element analyses and experiments performed with DIC method

Fiber Angle, φ_1 (°)	Fiber Angle, φ_2 (°)	GFRP Box-Beams		CFRP Box-Beams	
		Relative Error, γ (%)	Relative Error (Improved), γ (%)	Relative Error, γ (%)	Relative Error (Improved), γ (%)
15	25	4.48	3.67	4.55	3.97

Table 4.15 and Table 4.16 present the comparison of bend-twist coupling potentials of GFRP and CFRP plates and torque-boxes acquired from finite element analyses with improved material properties and DIC system, respectively. As in the experiments conducted with DIC system, finite element results show that CFRP material has higher bend-twist coupling potential when compared with the GFRP material. Nevertheless, this superiority decreases as the fiber angle orientation increases for both plates and box beam structures. Another observation that can be drawn when Table 4.15 and Table 4.16 are compared is that ratios of unit twist angles calculated from FEA and DIC results are very close for plates. For box-beams, on the other hand, there is a significant difference between FEA and DIC results. Nevertheless, relative difference of bend-twist coupling potentials due to fiber angle φ between FEA and DIC measurement are very close to each other with less than 5% difference.

Table 4.15 Comparison of bend-twist coupling potentials of GFRP and CFRP plates acquired from finite element analyses with improved material properties

Fiber Orientation Angle (°)	**GFRP Plates**	**CFRP Plates**	**(CFRP/GFRP) Ratio of Unit Twist Angle**	**(CFRP/GFRP) Ratio of Unit Twist Angle**
	Unit Twist Angle (°/mm)	**Unit Twist Angle (°/mm)**	***FEA Results*[1]**	***DIC Results***
0	0	0	-	-
10	0.0505	0.2026	4.01	3.88
15	0.0653	0.2296	3.52	3.55
20	0.0716	0.2228	3.11	3.17
25	0.0707	0.2001	2.83	2.69

[1] FEA results using material properties from iterative optimization process

Table 4.16 Comparison of bend-twist coupling potentials of GFRP and CFRP plates acquired from finite element analyses with improved material properties

Fiber Orientation Angle (°)	**GFRP Box-Beams**		**CFRP Box-Beams**		**(CFRP/GFRP) Ratio of Unit Twist Angle**	**(CFRP/GFRP) Ratio of Unit Twist Angle**
	Twist Angle (°)	**Unit Twist Angle (°/mm)**	**Twist Angle (°)**	**Unit Twist Angle (°/mm)**	***FEA Results*[1]**	***DIC Results***
0	0	0	0	0	-	-
15	0.0431	0.0390	0.0785	0.1309	3.36	1.46
25	0.0464	0.0423	0.1100	0.1090	2.58	1.14

[1] FEA results using material properties from iterative optimization process

Ratios of unit twist angles obtained both experimentally and numerically for plates and torque-boxes with different materials with varying fiber angles show that utilization of CFRP material in the spar cap region in wind turbine blades may have greater influence on reducing loads in the wind turbine system when compared to the GFRP material. In addition, due to high stiffness of the CFRP material, less number of CFRP plies is required to provide the sufficient blade stiffness. The effect of using off-axis GFRP and CFRP plies in the flange region of the wind turbine blade on the load reduction of wind turbine system is investigated in Chapter 5 with different bend-twist coupled blade designs. Experimental and finite element results on the bending-twisting coupling potential of GFRP plates and box beams reveal that for the GFRP material,

bending-twisting coupling increases up to approximately 25^{o} fiber orientation angle and reduces afterwards. For the CFRP plates and box beams, bending-twisting coupling increases up to approximately 15^{o} fiber orientation angle and reduces afterwards. Based on this outcome, in the bend-twist coupled wind turbine blades off-axis fiber angle range is decided to be 5^{o}-20^{o}. Experimental and numerical study on the evaluation of bending twisting coupling potential of GFRP and CFRP plates and box-beams allowed the determination of the off-axis fiber angles to implement in the bend-twist coupled blades in the wind turbine system for load alleviation purposes utilizing the concept of bending twisting coupling of composite blades.

CHAPTER 5

TRANSIENT AEROELASTIC ANALYSES OF MULTI-BODY WIND TURBINE SYSTEM AND REDUCTION OF LOADS

Bend-twist coupling potentials of GFRP and CFRP materials with the use of off-axis fiber orientation angles are examined with the experiments and finite element analyses in Chapter 4. In Chapter 5, the effect of bend-twist coupled blades, designed with the use of off-axis fiber angles in the spar flange regions of the blades, on the load reduction in the whole wind turbine system is studied. Wind turbine systems are modeled in Samcef Wind Turbines (SWT) [28] to study and compare the effect of bend-twist coupling on the load alleviation on several monitor points located on wind turbine system. Transient flexible multi-body aeroelastic analyses of the whole wind turbine system are done for different blade configuration under realistic operation scenarios and wind conditions defined in wind turbine design standard IEC 61400-1 [27] for the purpose of investigating the effect of bending twisting coupling on the load reduction. In the wind turbine model, except for the blade, standard sub-structure definitions are used which consist of tower structure, rotor hub, rotor shaft, staged gearbox, coupling shaft, generator system and bedplate. Multi-body simulations of the turbine systems are carried out with Samcef Mecano [39], a high performance finite element solver provided by Siemens PLM, embodies classical nonlinear implicit finite element analysis to multi-body simulation (*MBS*). The time history is grounded on the fully coupled formulation that includes aeroelasticity, controllers and structural flexibility. Samcef Wind Turbines (SWT) comprises this finite element solver which takes in multi-body simulation feature that design of subcomponents can be based on

these capabilities. Transient aeroelastic simulations are executed in time domain taking into consideration of structural, aerodynamic and control attributes via parametric integrator differentiator (PID) controller.

In this work, the effect of bend-twist coupling on the wind turbine blades on the load alleviation of whole wind turbine system is investigated. The bend-twist coupling effect on the blades is generated due to the anisotropic behavior of composite materials. The section of a wind turbine blade is composed of upper and lower skins, two shear webs (spars) that carry flapwise loads, and the flange regions between the webs, as depicted in Figure 5.1.

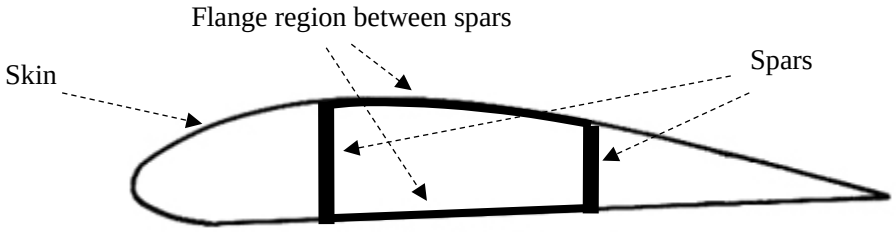

Figure 5.1 Section of a wind turbine blade

For a general wind turbine blade, the ratio of the length of the flange region between the webs to the chord length increases from blade root to the tip. Therefore, the most efficient way to utilize bend-twist coupling with the purpose of load alleviation is to apply off-axis composite plies at an angle of φ with respect to the blade axis towards feather. The ply placement on a bend-twist coupled section of a wind turbine blade can be seen in Figure 5.2. The utilization of bend-twist coupling for aerodynamic and/or structural optimization is called aeroelastic tailoring. Due to the off-axis ply placement at an angle of φ towards leading edge on the flange region between the shear webs, reduction of angle of attack (α) is aimed that leads to load alleviation for the subcomponents of the turbine system. Angle of attack is directly related to aerodynamic loads. Due to the aerodynamic forces, the blade twists due to the bending which increases the angle of attack. The aerodynamic forces and the angle of attack of

a blade section is presented in Figure 5.3. Moreover, since the torsional stiffness of the blade reduces towards the blade tip, the sections towards the tip are more prone to twist than the root sections. Due to this induced twist, aerodynamic loads on the wind turbine system increase. With the concept of bend-twist coupling, it is aimed to prevent the increase in angle of attack due to aerodynamic loads by inducing twist in the opposite direction in order to alleviate aerodynamic loads on the elements of the turbine system. Due to the off-axis ply placement with respect to the blade axis, flapwise stiffness of the aeroelastic tailored partition decreases whereas increased torsional stiffness prevents increment in angle of attack.

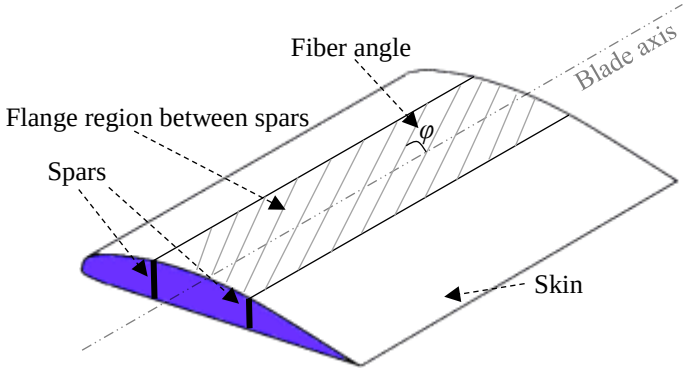

Figure 5.2 Bend-twist coupled section of a wind turbine blade

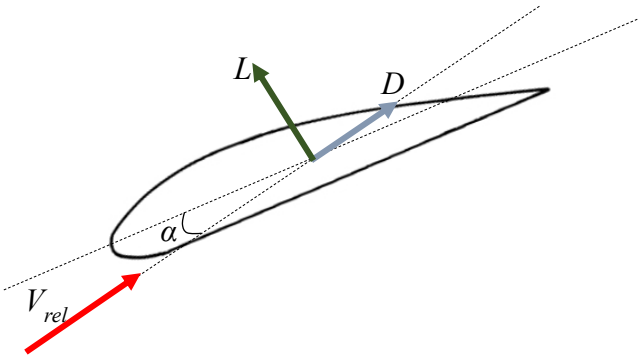

Figure 5.3 Aerodynamic forces on a blade section

5.1 Properties of Wind Turbine Model

Load reduction at the monitor point locations due to bend-twist coupling utilization is investigated by generating 5 MW wind turbine models in SWT with designed blades having different materials and fiber orientation angles in the flange region between the spars as depicted in Figure 5.2. Wind turbine model generated in SWT has the components of generic model of the tower, bedplate, gearbox, rotor shaft, coupling shaft, generator, 5 MW controller, and pre-bent superelement blade. Figure 5.4 presents the SWT model of the wind turbine with 4 meter prebent at the blade tip with 5º tilt angle.

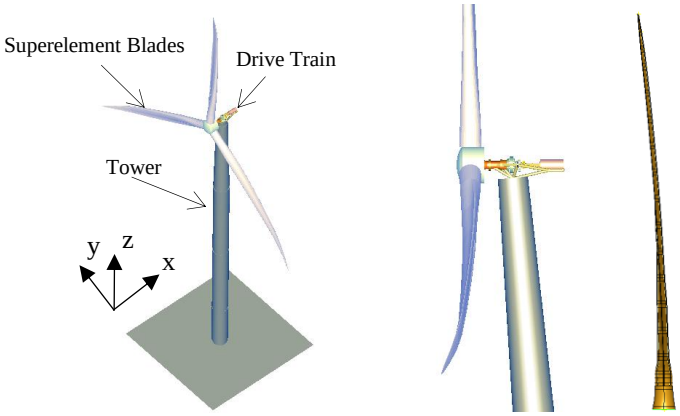

Figure 5.4 (a) SWT model of the wind turbine (b) tilt angle of the rotor and the pre-bent blade

Figure 5.5 shows the main components of the SWT drive train model. The rotor shaft is supported by two main bearings. The staged gearbox and coupling shaft linking the gearbox and the generator are also included in the drive train model. The CAD model of the wind turbine system is generated from the turbine tree of the user interface of SWT by selecting system elements. For accurate and consistent representation of the internal loads, main substructures of the wind turbine system must be present in the model. Elements of the SWT drive train model of the wind turbine

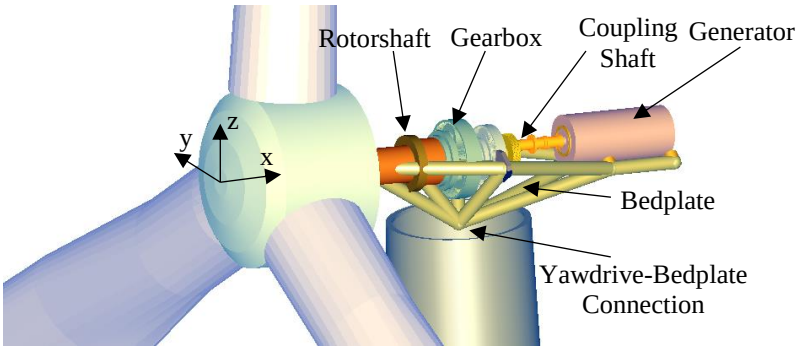

Figure 5.5 Elements of the SWT drive train model of the wind turbine

In SWT, wind turbine models are generated according to NREL's 5 MW [15] wind turbine. Main properties of the wind turbine generated in SWT are the same with NREL's 5 MW turbine; nevertheless, several properties differ. For instance, the rated wind speed and rotor speed for NREL's 5 MW wind turbine are 11.4 m/s and 12 rpm, respectively. For the wind turbine generated in SWT, on the other hand, the rated wind speed is 12 m/s. Properties of the baseline wind turbine are presented in Table 5.1. The rotor speed is controlled by a PID controller scheme. In simulations, the demanded torque generated is set to be 37880 Nm to yield the nominal electrical power production of 5 MW under the rated conditions for all turbine designs. The relation between the power generation, torque and rotor speed is given in Eq. 24.

$$P = T\omega \tag{24}$$

where, T is the generated torque and ω is angular coupling shaft speed. The angular coupling shaft speed is obtained by the multiplication of the rotor speed (in radians/second) and the gear ratio which is 105. For the rated conditions, in order to extract 5 MW of electrical power, torque generation and the rotor speed should be 37880 Nm and 12 rpm, respectively.

Wind turbine system analyses are executed for the power production case with Kaimal turbulence model to account for the external turbulent wind. Six simulations are

performed for six different turbulence wind profile designations with a mean speed of 15 m/s with the purpose of meeting the IEC 61400-1 standard. Simulations are made for six hundred seconds operation time of wind turbines and the acquired internal load data are then averaged to have mean value. In the simulations, demanded generator torque is set to 37880 Nm. It is worth to note that the nominal electrical power of 5 MW can be produced under the rated conditions for all wind turbine models which are created using different bend-twist coupled blades.

Table 5.1 Main properties of wind turbine system modeled in SWT

Nominal electrical power	5 MW
Number of blades	3
Number of blade elements used	17
Blade prebent at the blade end	4m
Rated rotor speed	12 RPM
Demanded rated generator torque	37880 Nm
Wind speed at hub height	15 m/s
Turbulent wind generator	TURBSIM [29]
Gearbox ratio	105
Rotor/Hub diameter	126 m/4 m
Hub length	4 m
Blade length	61.5 m
Rotor conicity	0°
Rotor tilt angle	5°
Gear ratio	105
Tower centerline elevation	98.2 m
Hub height	100 m
Hub mass	50000 kg
Hub inertia	100000 kgm^2
Controller	PID pitch position control

5.1.1 Wind Turbine Blade Models

NREL's 5 MW wind turbine blade is inversely designed with 17 sections along the spanwise direction [19]. The geometric properties of the inversely designed blade are composed from NREL's report [15]. Nevertheless, the transition region near the blade root remained undefined in the report. Thus, the transition region is generated so that

a smooth transition is achieved through the axis of the blade. The 3D reference blade design is shown in Figure 5.6.

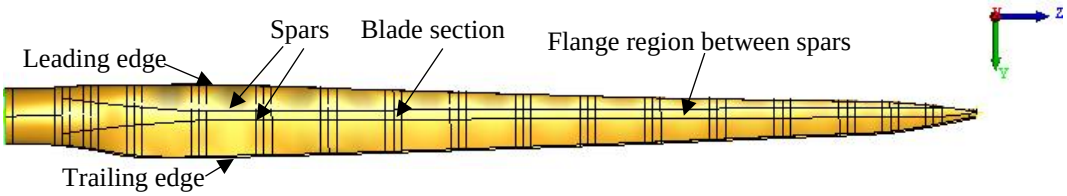

Figure 5.6 Three dimensional inversely designed reference blade

The chord lengths of the sections and the name of the airfoils are presented in Table 5.2. Front and rear spars are placed such that the thickest section of the airfoils are bounded by the shear webs. The blade pitch axis passes through the center of the circular cross-section of the root and the middle of the spars, and the sections of the blades are arranged accordingly to pitch axis. The inversely designed blade is fully composed of GFRP material. The skins between the leading edge and front spar, and rear spar and trailing edge portions as well as two spars are made of ±45° biaxial laminae. Furthermore, circular root blade section is composed of 0° and 90° UD GFRP plies placed with respect to the blade axis. Flange regions between the two shear webs on the pressure and suction side are shaded in dark brown in Figure 5.7 and are composed of 0° UD GFRP plies.

For the design process, sectional flatwise, flapwise and torsional stiffness properties of inversely designed blade are closely matched to that of NREL's 5 MW turbine blade with the modification of number of ply placement on each section by utilizing variational asymptotic beam section method (VABS) that calculates the sectional properties of the beam [40]. Utmost importance is given in the inverse design phase of the blade since the turbine blade ought to have comparable properties with the NREL's blade in order to represent the loads on the turbine and power production correctly.

Table 5.2 Geometrical properties of NREL's 5 MW turbine blade

Section Starting Point (m)	Chord Length of Section (m)	Airfoil Name
0	3.542	Circular
3.644	3.711	Transition
5.467	4.050	Transition
8.200	4.557	DU40_A17
12.300	4.652	DU35_A17
16.400	4.458	DU35_A17
20.500	4.249	DU30_A17
24.600	4.007	DU25_A17
28.700	3.748	DU25_A17
32.800	3.502	DU21_A19
36.900	3.256	DU21_A20
41.000	3.010	NACA643-618
45.100	2.764	NACA643-618
49.200	2.518	NACA643-618
53.300	2.313	NACA643-618
56.033	2.086	NACA643-618
58.767	1.419	NACA643-618
61.500	0.500	NACA643-618

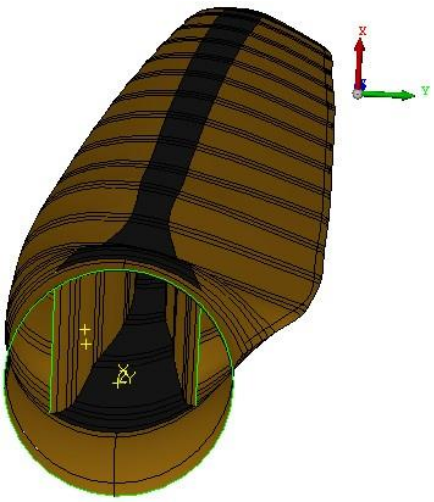

Figure 5.7 Flange region between the spars on pressure and suction sides

Sectional flapwise bending and torsional stiffness of the inversely designed reference blade and NREL's turbine blade for 17 sections are shown in Figure 5.8 and Figure

5.9, respectively. When Figure 5.8 and Figure 5.9 are investigated, reference turbine blade present comparable sectional flapwise and torsional stiffness values with 5MW wind turbine blade of NREL.

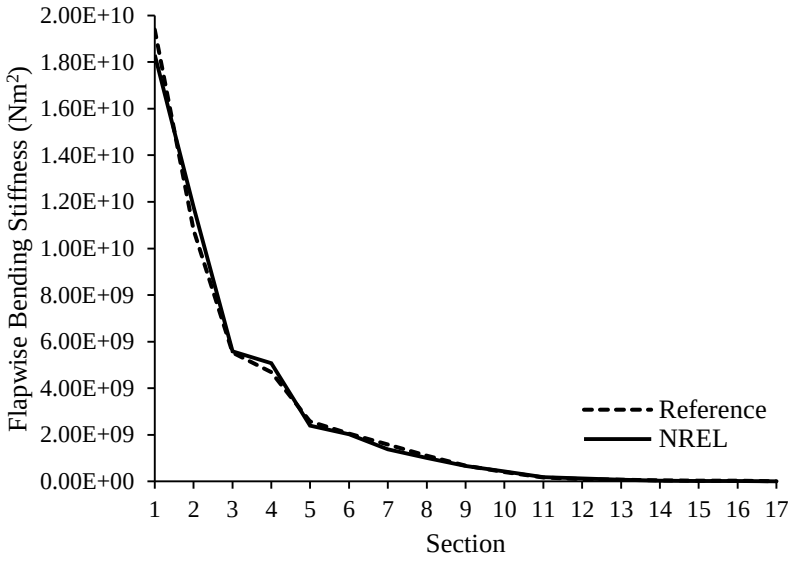

Figure 5.8 Sectional flapwise bending stiffness of the reference and NREL's 5MW turbine blade

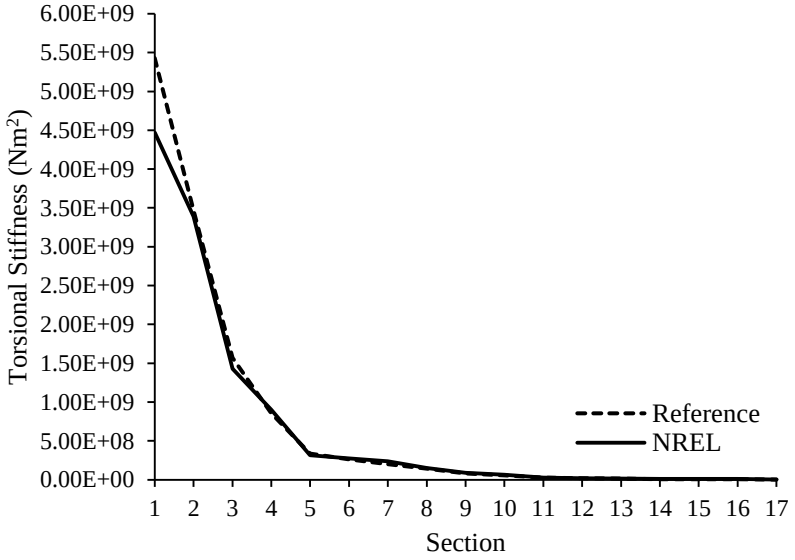

Figure 5.9 Sectional torsional bending stiffness of the reference and NREL's 5MW turbine blade

In order to evaluate the effect of bend-twist coupling utilization of the wind turbine blades, ten different wind turbine systems with modified blades are generated with the intention of load alleviation at several monitor points. The blades are created by modifying the spar cap plies at the outboard section of the blade. Note that the reference blade is an uncoupled blade that consists of on-axis GFRP plies in the flange region between the front and the rear webs. GFRP and CFRP materials are used in the spar cap plies in the design process of the blades. In the work of Gözcü et al., the properties of the reference blade is presented [41]. The baseline blade, which is the inversely designed wind turbine blade having sectional stiffness properties matched to that of NREL's 5 MW wind turbine blade, has full-GFRP material with 0° fiber angle configuration in the spar caps. Based on the outcome of the study of the determination of the bending-twisting coupling potential of GFRP and CFRP materials by experiments and finite element analyses, in the bend-twist coupled wind turbine blades off-axis fiber angle range is decided to be 5º-20º. Bend-twist coupling effect is exploited by utilizing GFRP and CFRP materials in spar cap plies oriented at 5º- 20º with 5º increments with respect to the blade axis. For all blade configurations, inboard 31.5 meter portion comprise of 0° GFRP plies. The outboard 30 meter portion of the blade is where the modifications take place by retaining GFRP and CFRP plies with 5º- 20º fiber angles in the spar caps as depicted in Figure 5.10.

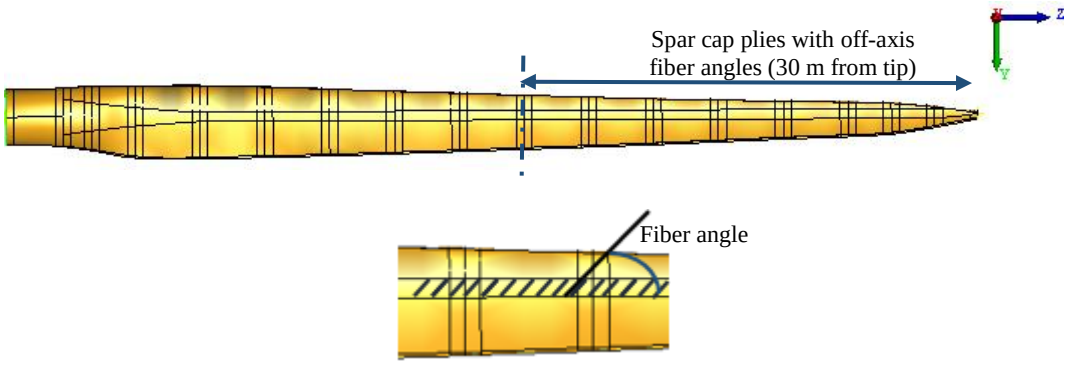

Figure 5.10 Spar cap region with fiber angles of the spar cap plies oriented with respect to the blade axis

In the work of Şener et al. [42], five blades are selected among the ten designed blades due to their structural performance on the load alleviation. Selected blades are described in Table 5.3. Baseline blade GFRP_1 is the inversely designed blade to match the NREL blade [15]. It has GFRP spar cap plies on both pressure and suction sides positioned along the blade axis. The bend-twist coupled GFRP_2 blade is generated by the rotation of the unidirectional plies in the flange area between the webs at the outboard section described in Figure 5.10 by a fiber orientation angle of φ. For GFRP_2 blade, the same number of plies is used for the coupled spar cap region as reference blade. Therefore, as aforementioned, sectional flapwise stiffness is sacrificed in order to gain torsional stiffness by off-axis ply usage. In order to keep the flapwise stiffness of GFRP_2 blade the same as GFRP_1 blade, more off-axis plies should be installed in the coupled spar cap region. Initial studies show that applying additional plies on that region resulted in no gain in load reduction on monitor points on the turbine system. The effect of such decrease in the count of off-axis plies on the maximum tip displacement is investigated in Section 5.2.3.

Table 5.3 Blade configurations studied

Blades	**Description**
GFRP_1	Baseline GFRP blade with pressure/suction side GFRP spar cap plies along the blade axis (0 deg.) in the bend-twist sections of the blade.
GFRP_2	0 deg. plies in the bend-twist sections of GFRP_1 blade are made 5º, 10º, 15º, and 20º.
HGCFRP_2	0 deg. plies of HGCFRP_1 are made 5º, 10º, 15º, and 20º HGCFRP_1: Number of CFRP layers in the bend-twist sections of blade is adjusted such that these sections have very close flapwise bending stiffness compared to the flapwise bending stiffness of GFRP_1.
HGCFRP_3	Number of CFRP layers in the bend-twist sections of the blade is adjusted such that these sections have very close flapwise bending stiffness compared to the flapwise bending stiffness of GFRP_2.
HGCFRP_5	2/3 of the total number of GFRP layers in the bend-twist sections of GFRP_1 is made 5º, 10º, 15º, and 20º, and 1/3 of the total number of GFRP layers in GFRP_1 is modified to CFRP at 5º, 10º, 15º, and 20º. CFRP plies are placed in the outer layers.

Because of higher bend-twist coupling potential and superior material properties of CFRP material, other three bend-twist coupled blades are selected as hybrid GFRP-CFRP blades due to the results of the preliminary studies. In order to generate hybrid bend-twist coupled blade, a reference hybrid uncoupled blade, abbreviated as HGCFRP_1, which has UD 0° CFRP plies on the flange area between webs is created by matching flapwise bending stiffness as close as that of reference blade GFRP_1. The design process of hybrid blades are relatively harder since the wind turbines with these hybrid blades must produce comparable power outputs as the reference wind turbine with the reduction at several monitor locations. Moreover, the cost of CFRP material is significantly higher than GFRP material. For the uncoupled hybrid blade HGCFRP_1, only outboard portion of spar cap plies are consist of CFRP plies. Understandably, less CFRP plies in the outboard flange area are required to match the sectional flapwise stiffness properties to that of GFRP_1 than GFRP plies. Front and rear spars, skins, and the plies on the inboard flange region are all consist of GFRP material. HGCFRP_2 blade is generated by rotating unidirectional CFRP plies at the outboard flange area by fiber angle orientation of φ. In like manner, for the creation of HGCFRP_3 blade, sectional flapwise bending stiffness of designated blade is adjusted as close as that of GFRP_2 blade for the specific fiber orientation angle φ. The idea behind of the generation of this blade is to take advantage of higher bend-twist coupling potential of CFRP material while matching the sectional properties to that of GFRP_2 plates without significant increase in material cost. Last of all, HGCFRP_5 blade is generated by replacing one third of the GFRP plies with CFRP plies at the outboard section in the reference blade and rotating all of the plies by angle of φ. Therefore, total number of plies at the flange area in the bend-twist coupled section of HGCFRP_5 is the same as GFRP_1 blade with the only difference being that one third of the GFRP plies converted in CFRP ones. Obviously, utilization of CFRP plies increases the flapwise bending stiffness considerably. In fact, HGCFRP_5 blade has the highest flapwise bending stiffness in the bend-twist coupled section among the five selected blades.

Blade designs given in Table 5.3 are converted into the superelement models in Samcef Field, a generic finite element solver [43]. Dynamic superelement that is used in this thesis is a non-linear superelement model which is based on Craig & Bampton component method [44]. The main benefit of using dynamic superelement blade model in multi-body dynamic wind turbine model is to achieve the detailed global model of the blade with complex geometry and structural assets while having a simpler dynamic model with less number of degrees of freedom leading to much less computational time for multi-body simulations. The superelement formulation allows the blade model to undergo large displacements and rotations in space associated with the rigid body rotation of the wind turbine blade. Upon generating a superelement model, several nodes on the finite element model are created which are called *retained nodes* that represent the points by which the super element will be connected to the main model. In the current design, 18 retained nodes are utilized. The retain nodes on the finite element model of the blade are presented in Figure 5.11. The first retained node is called the boundary retained node located at the center of the circular root section which acts as a connector between the blade and hub. The retained nodes are located at the aerodynamic centers of each blade section as Figure 5.11 depicts.

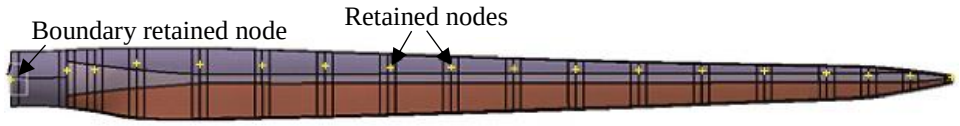

Figure 5.11 Retained nodes on a superelement blade

At the blade sections, neighboring surfaces are connected to retained nodes via mean elements. The displacements and the rotations at the retained nodes are calculated as the mean of the nodes of the adjacent surfaces' displacements and rotations. Figure 5.12 shows the mean elements at the neighboring faces connected to the retained nodes at the aerodynamic centers of the sections consist of DU25_A17 airfoil and circular cross-section at the root.

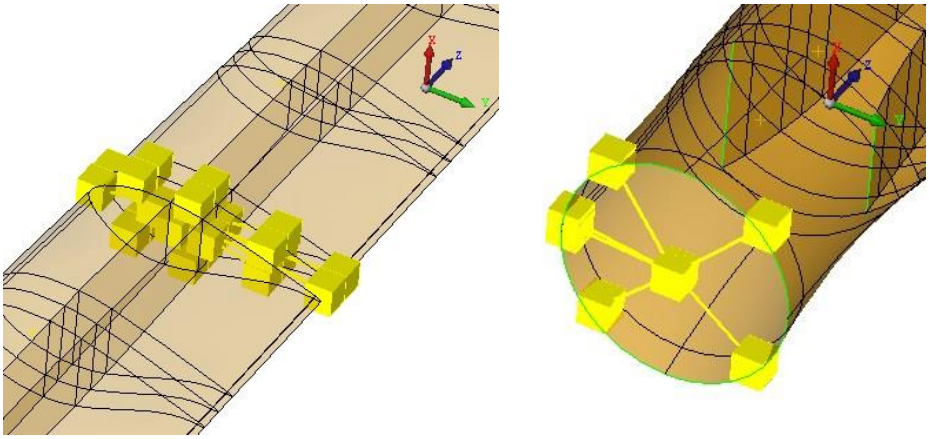

(a) (b)

Figure 5.12 Mean elements connected to the retained nodes at the (a) DU25_A17 airfoil section and (b) circular cross-section at the root

The superelement blade created in Samcef Field is implemented in the dynamic multi-body wind turbine model in SWT. Verification process is vital in order to evaluate the correctness of the superelement model extracted using original 3D finite element model. Verification of the superelement model of the blade is accomplished with the comparison of modal analysis results of three dimensional finite element and superelement models of the baseline blade. It is worth noting that in the SWT model of the turbine, connection between the blade and the hub is established by retained node which is tied to the neighboring faces via mean elements. Therefore, for the sake of consistency, the same boundary conditions are applied for both 3D FE and superelement models. Figure 5.13 shows the location of the retained node on which the boundary condition applied.

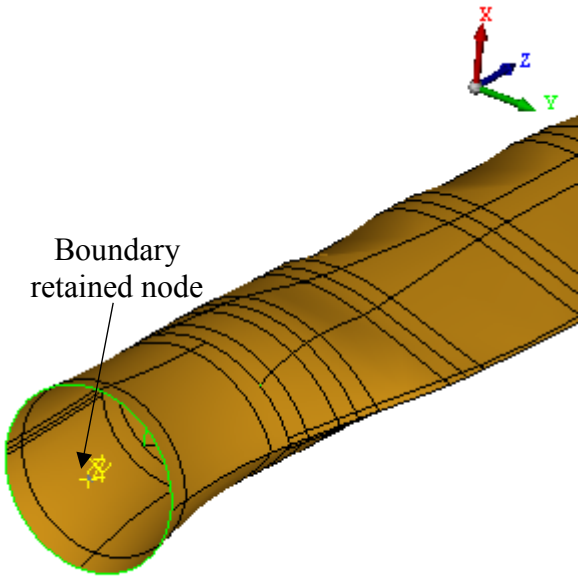

Figure 5.13 Location of the retained node on the superelement blade

First five modes of the baseline 3D FE and superelement blades that include major flapwise, chordwise and torsional modes are compared in Table 5.4. Results show that there is good agreement between the free vibration frequencies obtained by the 3D FE and superelement blade models. It is thus concluded that the superelement blade included in the wind turbine model generated in SWT for performing the transient aeroelastic analyses.

Table 5.4 Comparison of first five free vibrational frequencies of baseline 3D FE and superelement blade models

Modes	**3D FE Model (Hz)**	**Superelement Blade (Hz)**
1	0.703	0.703
2	1.071	1.071
3	1.794	1.799
4	3.005	3.011
5	3.465	3.480

The calculations of the aeroelastic loads on the rotor is one of the most important aspects of the computational tools handled in the wind turbine aeroelastic analyses. SWT utilizes unsteady blade element momentum (BEM) theory so as to resolve the wake equilibrium problem at the rotor [45]. Stationary aerodynamic calculation results obtained by SWT is compared with another computational tool, Bladed [46], a wind turbine design software produced by DNV GL, in order to validate the credibility of the results obtained by SWT. Default library values are selected for wind turbine models. Since "Aerodynamic Information" process of Bladed software does not contain azimuth-dependent effects, wind shear, spatial wind turbulence, and tower shadow effects are deactivated in SWT model of the wind turbine. The simulations are performed for rated conditions of the default wind turbine models of the multi-body codes with wind speed of 12 m/s, rotor speed of 15 rpm, and blade pitch angle of 0°. Note that constant wind speed is imposed on the turbine models; hence, the simulations are nearly perfectly steady-state. Table 5.5 presents the rotor torque, power generation, and power coefficient (C_p) values for wind turbine models that are set up in SWT and Bladed multi-body codes that underwent transient aeroelastic analyses under rated wind conditions. As Table 5.5 shows, the results found for the rotor torque, power generation, and power coefficient (C_p) values obtained by Bladed and SWT are very close to each other with negligible differences. This work validates the reliability of aerodynamic calculations conducted by Samcef Wind Turbines (SWT).

Table 5.5 Torque, power and power coefficient values obtained by Bladed and SWT

Results	**Bladed**	**SWT**	**Percent Difference (%)**
Rotor Torque (Nm)	1.20E+06	1.21E+06	0.2
Power (W)	1.89E+06	1.89E+06	0.2
Power Coefficient, C_p	0.355	0.356	0.2

5.1.2 Drive Train Model

The drive train of the wind turbine model generated in SWT consists of the rotor shaft, 2 planetary and 1 parallel gearboxes, coupling shaft and the generator. The designed blades are attached to the hub which has a diameter of 4 meters and a mass of 4 tons. There are two main bearings located on the bedplate as shown in Figure 5.14. In this model, main bearing 1 takes up all the axial force while main bearing 2 opposes the lateral forces. The bedplate has a total mass of 28.6 tons. The bearings have 4000 kN/mm axial and 200000 kN/mm radial stiffness with 10 N/mm radial bending stiffness.

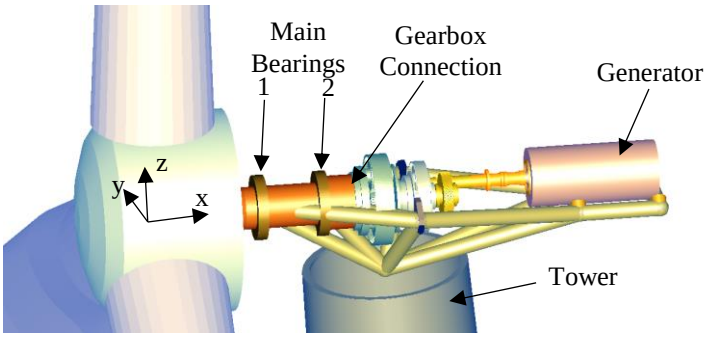

Figure 5.14 Main bearings and shaft-gearbox connection locations

Two planetary and one parallel gears increase the rotor speed acquired from low-speed rotor shaft and transmit it to the coupling shaft. The total gearbox ratio is 105 meaning that the rotor shaft speed is increased by 105 times. Figure 5.15 presents the gearboxes of the turbine system. The gearboxes which are colored green are planetary gear and located on the rotor side. The one in yellow color is the helical gear and positioned on the generator side.

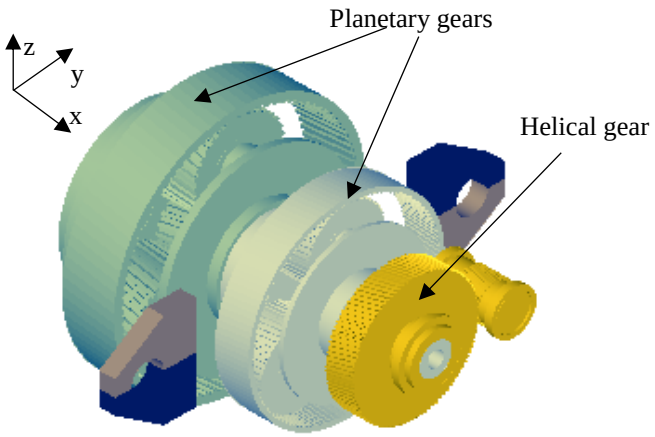

Figure 5.15 The two planetary and one helical gearboxes of the wind turbine system

The high speed (HS) coupling shaft has a diameter of 234 mm with a torsional stiffness of 3200 kNm/rad with maximum allowable torque of 14 kNm. HS coupling shaft comprises of the brake system, and slip and elastic coupling. The tower model is selected from the data tree in SWT as a standard tower with a height of 100m. The tower is made from steel with elastic modulus of 210 GPa and density of 8500 kg/m^3. The outer lower and upper diameters are 6 and 3.87 meters, respectively. The inner lower and upper diameters are 5.946 and 3.832 meters, respectively. In the SWT model, displacements and reactions at the tower top as well as tower foundation reactions are calculated during multi-body dynamic analyses.

5.1.3 Load Case and Wind Definitions

Multi-body simulations of wind turbine systems with superelement blade definitions are performed for the power production design load case with Kaimal turbulence model as the external wind loading. The mean wind speed at the reference height is taken as 15 m/s with a wind shear exponent of 0.2. IEC turbulence type is selected as normal turbulence with turbulence class of B. Initial pitch angle, rotor rotation speed and power are imposed by the wind dependent controller. The analyses are performed

for a duration of 615 seconds, nonetheless; calculations are made for 600 seconds, excluding initial 15 seconds which correspond to initial 3 revolutions of the rotor.

The calculations are performed for transient analyses with 6 different turbulent wind profiles with 15 m/s mean wind speed for each wind turbine configuration. The turbulent wind profiles are generated from TurbSim runtime options with pseudorandom number generator (pRNG) by selecting two random seeds of integers between –2147483648 and 2147483647 [29]. These selected seeds are utilized to generate phases one per frequency per grid point per wind component for the velocity time series. If the selected pRNG is kept the same, the exact same random turbulent wind profile is generated for each analysis making it useful to compare the effects of changes in blade configurations. In order to create a random turbulent wind, first and second random seeds are entered in "TurbSim Runtime Options" under the turbulent wind generator tab depicted in Figure 5.16.

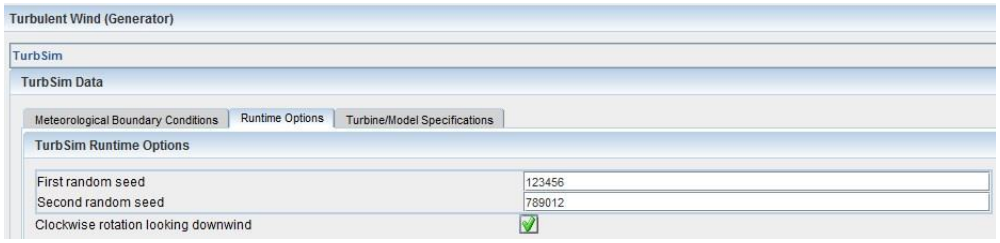

Figure 5.16 Turbulent wind generator tab in SWT

Six random turbulent profiles are generated by selecting pairs of first and second random seeds. The selected random seeds are presented in Table 5.6. TurbSim employs these selected seeds to create wind profile by utilizing two separate congruential generators together with the algorithm developed by L'ecuyer [47]. Figure 5.17 presents the corresponding turbulent wind profiles with the mean speed of 15 m/s that are generated by utilizing the random seeds given in Table 5.6. Each wind profile is unique due to pRNG definition with the exception that the mean wind speed is 15 m/s for all wind definitions.

Table 5.6 Selected random seeds for generation of turbulent wind profiles

Seed Number	First Random Seed	Second Random Seed
1	123456	789012
2	473944	923564
3	4752375	5783785
4	8345350	5257752
5	77535238	77535238
6	142747	7836785

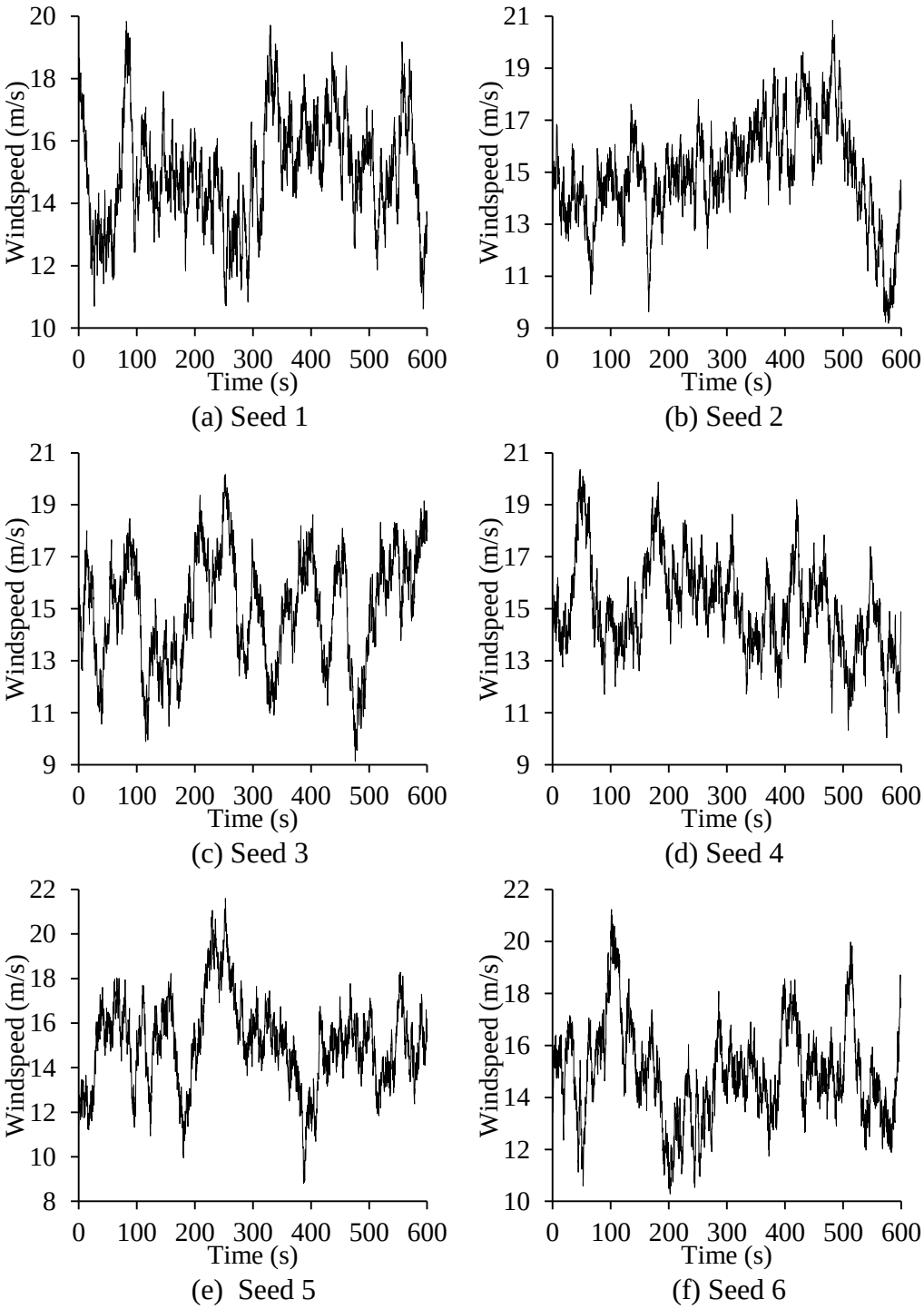

Figure 5.17 Turbulent wind profiles generated by TurbSim corresponding to pRNG seeds

The objectives of this study are to achieve load alleviation at the several monitor points on the wind turbine system and reduce stress in the blades whilst keeping the power production same level as the baseline turbine model and having sufficient tower-blade tip gap. For load alleviation, Fatigue damage equivalent load (DEL) is taken as indication of the deprivation of different parts of the wind turbine structure due to material fatigue incurred under cyclic loading. Reduction in damage equivalent loads is the implication of increased fatigue life of substructures. The S-N curve, a plot of stress and number of cycles, can be described by Basquin's equation in the high-cycle region as in Eq. 25.

$$S^q M = c \tag{25}$$

where, S is the stress amplitude, M is the number of cycles, and q and c are the exponent related to fatigue loading and empirical constant, respectively. For the same body under cyclic loading, force (P) versus number of cycle graph can be plotted instead of stress versus number of cycle graph.

Figure 5.18 shows two forces affecting on an arbitrary body and corresponding number of cycles due to forces.

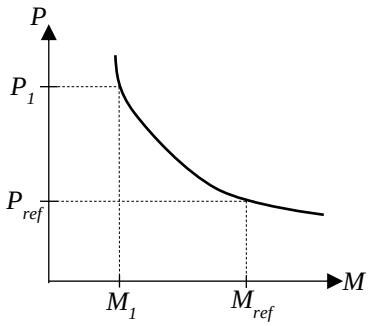

Figure 5.18 Force versus number of cycles curve

By utilizing Basquin's equation, it can be stated that in Eq. 26:

$$\frac{M_1}{M_{ref}} = \left(\frac{P_{ref}}{P_1}\right)^q \tag{26}$$

The term M_1 can be explicitly written in Eq. 27 as,

$$M_1 = \left(\frac{P_{ref}}{P_1}\right)^q M_{ref} \tag{27}$$

If a body experiences damages from n sources, with the fractional damage at the stress level S_j being m_j/M_j, damage incurred due to these sources (D) can be written as in Eq. 28.

$$D = \frac{m_1}{M_1} + \frac{m_2}{M_2} + \cdots + \frac{m_n}{M_n} = \sum_{j=1}^{n} \frac{m_j}{\left(\frac{P_{ref}}{P_j}\right)^q M_{ref}} \tag{28}$$

Miner's Rule states that the fatigue failure occurs when D is equal to 1. Therefore, at the fatigue failure case, Eq. 29 can be written:

$$\sum_{j=1}^{n} \frac{m_j}{\left(\frac{P_{ref}}{P_j}\right)^q M_{ref}} = 1 \tag{29}$$

By explicitly writing P_{ref} term in Eq. 29 yields to fatigue damage equivalent load equation represented in Eq. 30:

$$P_{ref} = \left(\sum_{j=1}^{n} \frac{P_j^q m_j}{M_{ref}}\right)^{1/q} \tag{30}$$

In Eq. 30, M_{ref} is usually taken as 10^8 for wind turbine components, and P_j, and m_j are the internal load and fatigue load cycles in the j^{th} load division, respectively. If two different spectra are selected, the ratio of fatigue damage equivalent (DEL) will be independent from the reference number of cycle (M_{ref}) provided that the same reference number of cycle is chosen for both spectra as shown in Eq. 31.

$$\frac{(F_{DEL})_1}{(F_{DEL})_2} = \frac{\left(\sum_{j=1}^{n} P_j^q m_j\right)^{1/m}}{\left(\sum_{k=1}^{n} P_k^q m_k\right)^{1/m}} \tag{31}$$

The results of fatigue damage equivalent loads at the critical monitor points of the wind turbine systems with coupled blades are presented in ratios with respect to the damage equivalent fatigue load at these points of the wind turbine system with the reference uncoupled blade. With that way, the ratio will be independent from the reference number of cycles. If the ratio at the selected monitor point is smaller than 1, it indicates that load mitigation occurs due to the utilization of bend-twist coupled blade in the wind turbine system.

5.1.4 Stress Recovery Process in Superelement Blades

Although the primary objective of the present study is to reduce loads at the monitor points on the wind turbine system while keeping the power production at 5 MW, it is equally important to achieve decreases in maximum stresses in the wind turbine blades. The stress computation in SWT is accomplished by the superelement restitution which makes it possible to compute the ply stresses in the original 3D finite element model which is associated to the degrees of freedom of the superelement blade. It should be emphasized that if the blade is integrated to the wind turbine system as superelement blade, the full FEM solution can be obtained by superelement restitution process at the selected time steps of the transient analysis in SWT [48]. Having done the transient aeroelastic analysis, superelement restitution analysis (RSUP) is performed in the defined time range with discrete time steps in SWT. Subsequently, post processing in Samcef Field is initiated to obtain the stresses distribution in the 3D finite element model. As an example, Figure 5.19 shows the superelement restitution analysis (RSUP) data selection tab in SWT for HGCFRP_2 blade with 10° fiber angle configuration.

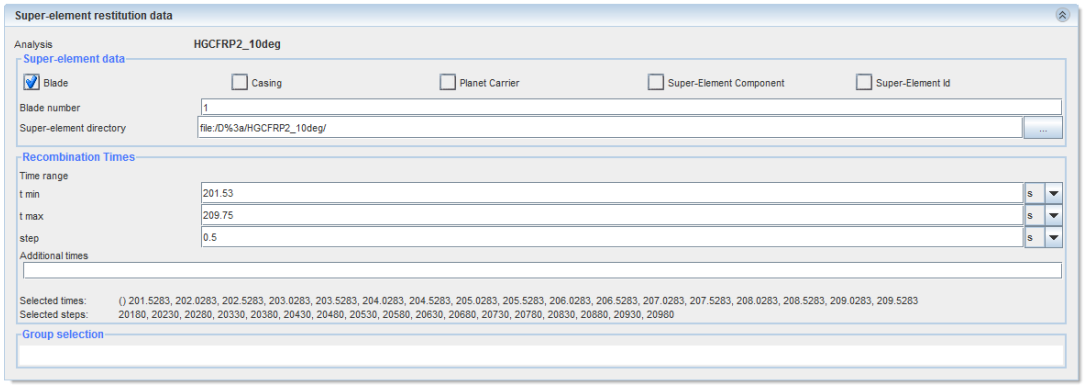

Figure 5.19 Superelement restitution analysis (RSUP) data selection tab for HGCFRP_2 blade with 10° fiber angle configuration

5.2 Results

As mentioned previously, bend-twist coupled twist coupled blades are generated by the off-axis ply placement at the outboard 30 meter of the blades. In Figure 5.20, the flange regions between the spars on the pressure and suction sides on which yellow lines drawn show the bend-twist coupled sections of the blade.

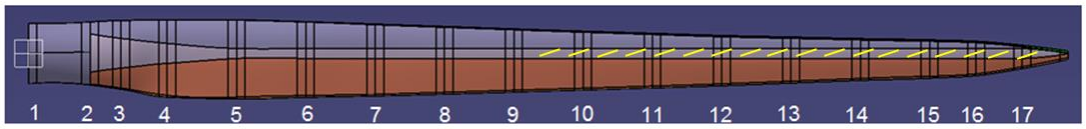

Figure 5.20 Bend-twist coupled flange regions between the webs

Sectional lift values for the reference blade GFRP_1 and bend-twist coupled blade GFRP_2 with 15° off-axis ply placement at the outboard section are presented in Figure 5.21 as a result of 600-second aeroelastic analysis performed in SWT. At the outboard bend-twist coupled sections of the blade, sectional lift is reduced. However, for the inboard uncoupled sections, the sectional lift is increased for bend-twist coupled GFRP_2 when compared to reference blade. For 600-seconds of aeroelastic analyses, the mean pitch angle of reference blade is 7.7°, whereas the mean pitch angle of bend-twist coupled blade is calculated to be 6.6°. Therefore, the main reason for the

increase in lift at the inboard sections of the bend-twist coupled blade is the reduction in pitch angle in order for turbine system to generate the required torque to produce 5MW of electricity. Although there is an increase in the sectional lift at the inboard sections, it is shown that there are significant reduction in fatigue damage equivalent flapwise moment and shear force at the root.

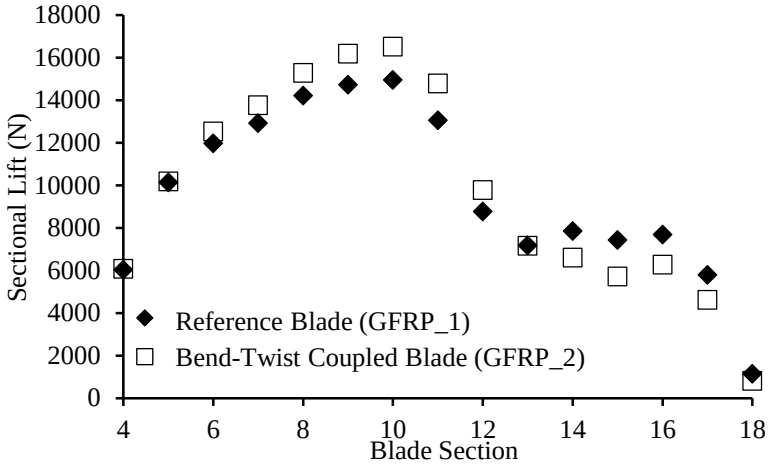

Figure 5.21 Sectional lift in blade sections for the reference blade and bend-twist coupled GFRP_2 blade with 15° off-axis plies

Effectiveness of the bending twisting coupling with the utilization of the designed bend-twist coupled blades is evaluated based on the reductions achieved in damage equivalent loads at the selected monitor points, electrical power produced, tower-blade end gap, and maximum stresses in the blades of the wind turbine systems. The calculations are based on performing 600-second transient aeroelastic analysis with 6 different turbulent wind profiles with 15 m/s mean wind speed for all wind turbine configurations. Damage equivalent loads, power productions and blade tip displacements obtained from the transient aeroelastic analyses of the multibody wind turbine system for the six different turbulent wind conditions are then averaged to yield mean values for the damage equivalent loads, power productions and blade tip displacements.

5.2.1 Load Alleviation in the Whole Wind Turbine System

Due to the bend-twist coupled sections of the blades, load reduction in the whole wind turbine system may occur because of the coupling of bending and twisting deformations of the blade sections. The fatigue damage equivalent load ratios at the monitor points are taken as the measure for the load alleviation in the wind turbine subsystems. The aim is to acquire decrease in the damage equivalent loads at the monitor points by introducing bend-twist coupling with four different non-zero fiber orientations in bend-twist coupled sections of the blades. Damage equivalent loads at these points are calculated for 6 different turbulent wind profiles and are averaged as stated in IEC 61400-1. Performance of bend-twist coupling is determined by the reduction that bend-twist coupling effect provides on damage equivalent loads. It is worth to note that off-axis fiber placement in the bend-twist sections of the blade does not solely reduce loads in the blade, but also causes load decrease at the shaft-gearbox connection, yaw drive-bedplate connection and main bearing of the turbine.

Figure 5.22 presents the variation of flapwise, edgewise, and torsional moments at the blade root of reference GFRP_1 blade in a 600-second of operation interval. From Figure 5.22, it can be clearly stated that the torsional moment is much smaller than flapwise and edgewise moments. Therefore, damage equivalent torsional moment and radial force at the blade root are excluded from the calculations.

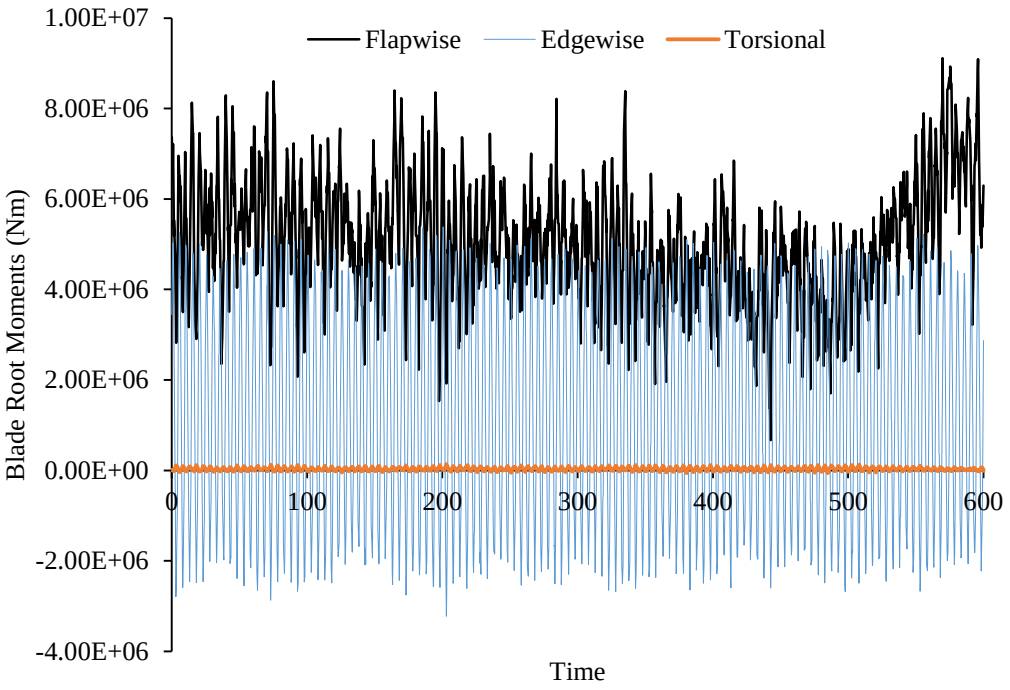

Figure 5.22 Variation of flapwise, edgewise, and torsional moments at the blade root of the reference GFRP_1 blade

Table 5.7-Table 5.10 present the damage equivalent loads and moments at the blade root for the wind turbine systems with the reference and designed bend-twist coupled blades. Fatigue damage equivalent loads and moment are calculated with Eq. 30. In order to have a clear understanding of the load reductions at the examined points, the ratios of the damage equivalent loads for wind turbine systems with designed bend-twist coupled blade to the turbine system with reference blade are also given at the monitor points. Note that the values presented in Table 5.7-Table 5.10 are the mean values that are extracted from six analyses performed under six different turbulent wind profiles. The change of damage equivalent loads with respect to the fiber orientation angle for designed coupled blades is the main concern of this work. Thus, variation graphs of damage equivalent loads with respect to fiber orientation angles for wind turbine systems with designed bend-twist coupled are plotted in order to further investigate the effect of bend-twist coupling on the reduction in loads in the whole turbine system.

Table 5.7 Damage equivalent loads and the ratios at the blade root* / Fiber orientation angle (φ)=5°

Wind turbine system with blades		GFRP_1	GFRP_2	HGCFRP_2	HGCFRP_3	HGCFRP_5
DEL	Leadwise Moment (Nm)	235339	234621	192880	193544	230200
	Flapwise Moment (Nm)	136157	129601	123921	125131	133077
	Leadwise Shear Force (N)	12438	12426	11366	11382	12313
	Flapwise Shear Force (N)	4025	3901	3784	3820	3968
DEL Ratio	Leadwise Moment (Nm)		1.00	0.82	0.82	0.98
	Flapwise Moment (Nm)		0.95	0.91	0.92	0.98
	Leadwise Shear Force (N)		1.00	0.91	0.92	0.99
	Flapwise Shear Force (N)		0.97	0.94	0.95	0.99

* Mean wind speed: 15 m/s, Duration: 15-615 seconds, Fatigue exponent=4, Number of bins=1000

Table 5.8 Damage equivalent loads and the ratios at the blade root* / Fiber orientation angle (φ)=10°

Wind turbine system with blades		GFRP_1	GFRP_2	HGCFRP_2	HGCFRP_3	HGCFRP_5
DEL	Leadwise Moment (Nm)	235339	234158	197467	191713	229289
	Flapwise Moment (Nm)	136157	124869	117568	115150	127096
	Leadwise Shear Force (N)	12438	12423	11480	11339	12306
	Flapwise Shear Force (N)	4025	3814	3660	3611	3851
DEL Ratio	Leadwise Moment		0.99	0.84	0.81	0.97
	Flapwise Moment		0.92	0.86	0.85	0.93
	Leadwise Shear Force		1.00	0.92	0.91	0.99
	Flapwise Shear Force		0.95	0.91	0.90	0.96

* Mean wind speed: 15 m/s, Duration: 15-615 seconds, Fatigue exponent=4, Number of bins=1000

Table 5.9 Damage equivalent loads and the ratios at the blade root* / Fiber orientation angle (φ)=15°

Wind turbine system with blades		GFRP_1	GFRP_2	HGCFRP_2	HGCFRP_3	HGCFRP_5
DEL	Leadwise Moment (Nm)	235339	233858	190869	197246	228905
	Flapwise Moment (Nm)	136157	120347	107460	114234	122266
	Leadwise Shear Force (N)	12438	12418	11312	11485	12296
	Flapwise Shear Force (N)	4025	3734	3429	3584	3769
DEL Ratio	Leadwise Moment		0.99	0.81	0.84	0.97
	Flapwise Moment		0.88	0.79	0.84	0.90
	Leadwise Shear Force		1	0.91	0.92	0.99
	Flapwise Shear Force		0.93	0.85	0.89	0.94

* Mean wind speed: 15 m/s, Duration: 15-615 seconds, Fatigue exponent=4, Number of bins=1000

Table 5.10 Damage equivalent loads and the ratios at the blade root* / Fiber orientation angle (φ)=20°

Wind turbine system with blades		GFRP_1	GFRP_2	HGCFRP_2	HGCFRP_3	HGCFRP_5
DEL	Leadwise Moment (Nm)	235339	234231	190518	197893	229165
	Flapwise Moment (Nm)	136157	117823	103224	111884	118958
	Leadwise Shear Force (N)	12438	12425	11293	11505	12300
	Flapwise Shear Force (N)	4025	3682	3332	3523	3693
DEL Ratio	Leadwise Moment		1.00	0.81	0.84	0.97
	Flapwise Moment		0.87	0.76	0.82	0.87
	Leadwise Shear Force		1.00	0.91	0.92	0.99
	Flapwise Shear Force		0.91	0.83	0.88	0.92

* Mean wind speed: 15 m/s, Duration: 15-615 seconds, Fatigue exponent=4, Number of bins=1000

Figure 5.23 displays the variation of the ratio of damage equivalent flapwise and leadwise moments at the blade root of the wind turbine models with bend-twist coupled blades with respect to the wind turbine with the baseline GFRP_1 blade with the fiber orientation angle of 0° in the spar caps. Likewise, Figure 5.24 presents the variation of the ratio of damage equivalent flapwise and leadwise shear forces at the blade root of the wind turbine model with coupled blades with respect to the turbine system with the reference blade.

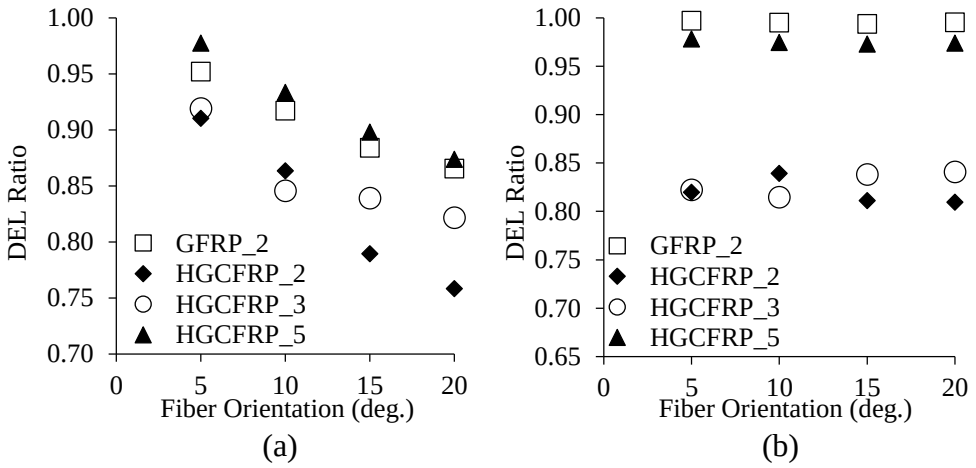

Figure 5.23 Variation of the ratio of damage equivalent (a) flapwise blade root moment and (b) leadwise root moment with the fiber angle for wind turbine models with bend-twist coupled blades

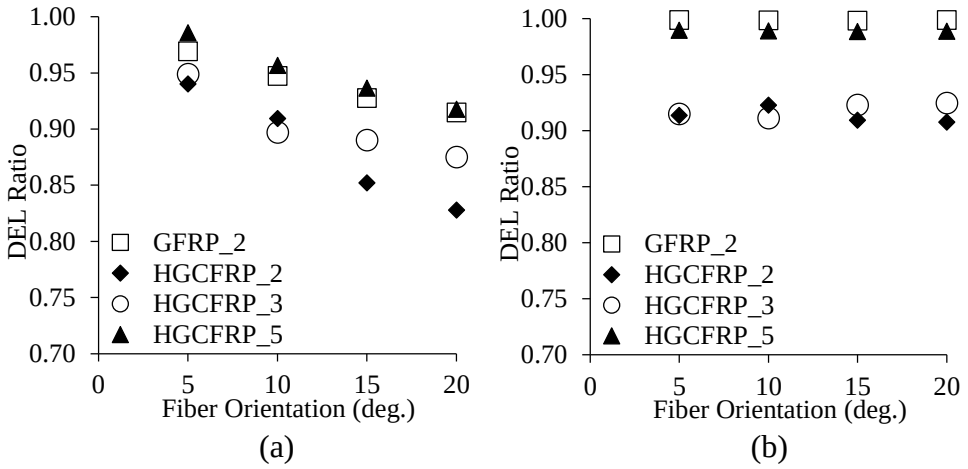

Figure 5.24 Variation of the ratio of damage equivalent (a) flapwise and (b) leadwise shear force at the root with the fiber angle for wind turbine models with bend-twist coupled blades

Results are obtained by SWT, and ratio of the damage equivalent loads is calculated with respect to the wind turbine model with the baseline blade GFRP_1 for different spar cap fiber angles. If the ratio of the damage equivalent loads (DEL) is 1, it indicates that the damage equivalent load at the requested monitor point of the wind turbine system with the bend-twist coupled blade is same as the damage equivalent load in the reference wind turbine system with the baseline blade GFRP_1. Reduction in damage equivalent flapwise moment leads to lower maximum stress in the blade, thus longer blade life. Due to the bend-twist coupling, the blade twists as it bends as a result of anisotropic behavior of composite materials. Figure 5.23 and Figure 5.24 show that as the fiber angle increases, higher reductions in damage equivalent flapwise moment and shear force are obtained. For the case of the wind turbine configuration with the HGCFRP_5 blade, the stiffest blade in terms of bending, more than 10 percent reduction in damage equivalent flapwise moment occurs. Furthermore, by utilizing only CFRP material in the flange regions of the blade, as in HGCFRP_2 and HGCFRP_3, higher reduction in damage equivalent flapwise bending moment is obtained compared to full GFRP bend-twist blade GFRP_2. Despite the fact that damage equivalent flapwise moment reduces for increasing fiber angle for all blade configurations, this is not the case for damage equivalent leadwise moment and shear

force. Utilization of off-axis fiber angle does reduce the leadwise moment and shear force up to 20% and 10%, respectively, for wind turbines with HGCFRP_2 and HGCFRP_3 blades due to the CFRP material usage on the spar caps. Increasing the fiber angle in the spar cap plies does not contribute to reduce leadwise moment further as it has little effect on leadwise stiffness terms. Utilization of off-axis plies in the flange area induces bending-torsional coupling and this placement has the most effect on flapwise bending stiffness and torsional stiffness, as explained in Chapter 4 and in the beginning of Chapter 5. Moreover, due to the reduction in lift in bend-twist coupled sections, as Figure 5.21 depicts, it has greater effect on the reduction in flapwise moment and shear force. Off-axis ply utilization has also influence on torsional moment at the blade root, nonetheless; time history of torsional moment is very low when compared to flapwise and edgewise moments. Therefore, torsional moment and radial force are omitted from the calculations. Another monitor point which has been investigated is damage equivalent bending moment and the shear force in y-direction at the shaft-gearbox connection. Figure 5.25 illustrates a closer look on the location of the shaft-gearbox connection monitor point. The bending moment and shear force are given in y-direction with respect to the coordinate system presented in Figure 5.25. Figure 5.26 shows the variation of the ratio of the damage equivalent bending moment and the shear force transmitted from the rotor shaft to the gearbox connection in the SWT model of the wind turbine with bend-twist coupled blades with respect to the wind turbine with the baseline blade GFRP_1. Figure 5.26 illustrates that damage equivalent bending moment at the shaft-gearbox connection decreases substantially as the fiber angle is increased. Correspondingly, damage equivalent shear force at the same location reduces up to 10% for the HGCFRP_2 blade. Using CFRP material in the spar cap plies of the bend-twist coupled blade again provides higher reduction at the shaft-gearbox connection compared to full GFRP bend-twist coupled blade GFRP_2. Statistically, gearboxes of the wind turbine systems are to be replaced every 5 to 7 years, and due to complex manufacturing processes, they are costly [49]. It should be noted that most of the failures occur in gearboxes of wind turbines and reduction in damage equivalent loads at the gearbox connection is important to lower the probability of damage that can be incurred in the gearbox.

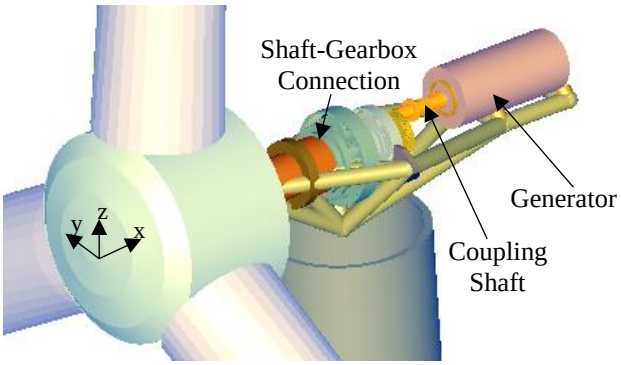

Figure 5.25 Shaft-gearbox connection location on a wind turbine system

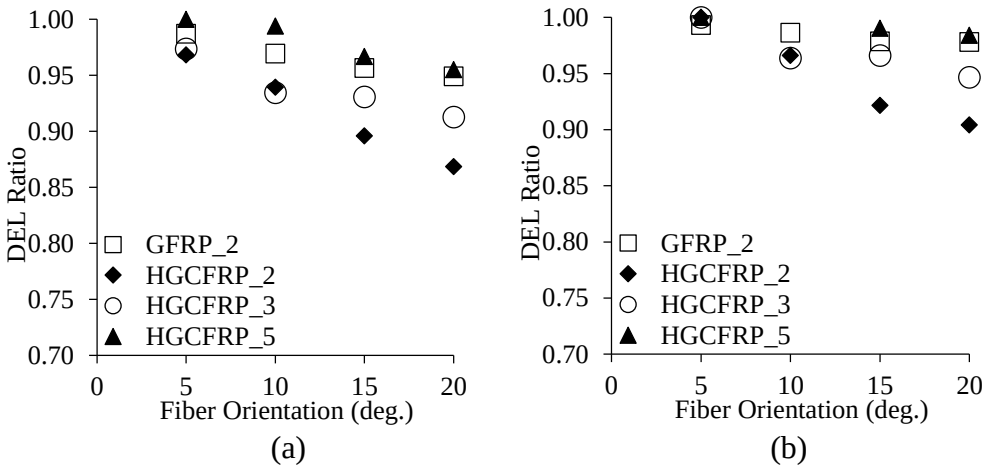

Figure 5.26 Variation of the ratio of damage equivalent (a) bending moment and (b) shear force in y-direction at the shaft-gearbox connection with the fiber angle for wind turbine models with bend-twist coupled blades

Seventy six percent of the gearbox failures are caused by bearings due to axial cracks forming in the bearings during the operation of high- and intermediate-speed stages of wind turbine systems [50]. Therefore, alleviation of the axial and the lateral forces in the bearings holds great importance for elongating the life of wind turbine systems without failure. Figure 5.14 shows the bearings and the shaft-gearbox connection point in the SWT model. In the drive train model designed in SWT, main bearing 1 takes up all the axial force, whilst the main bearing 2 bears lateral forces. Figure 5.27 gives the variation of the ratio of damage equivalent axial force x and shear force z in the main

bearing 1 and main bearing 2, respectively, in the wind turbine models with bend-twist coupled blades with the fiber angle. By utilizing bend-twist coupling in wind turbine blades, especially for hybrid CFRP-GFRP bend-twist coupled blades, significant reductions can be accomplished in the damage equivalent axial force x in main bearing 1 and shear force z in main bearing 2 with the fiber angle, as shown in Figure 5.27. The axial force on the bearing and the shaft is directly related to the thrust component of the lift force acting on the blades. Due to the bend-twist coupling effect on the blades, axial force on the bearing reduces noticeably. This is because of the reduction of the lift force. For fiber orientation angle greater than 10°, significant reductions occur in the shear force in z-direction in main bearing 2, particularly for hybrid GFRP-CFRP bend-twist coupled blades. Reduction in the axial and the shear forces on the main bearings are essential to reduce bearing failures due to fatigue loading in long operation of the wind turbine system.

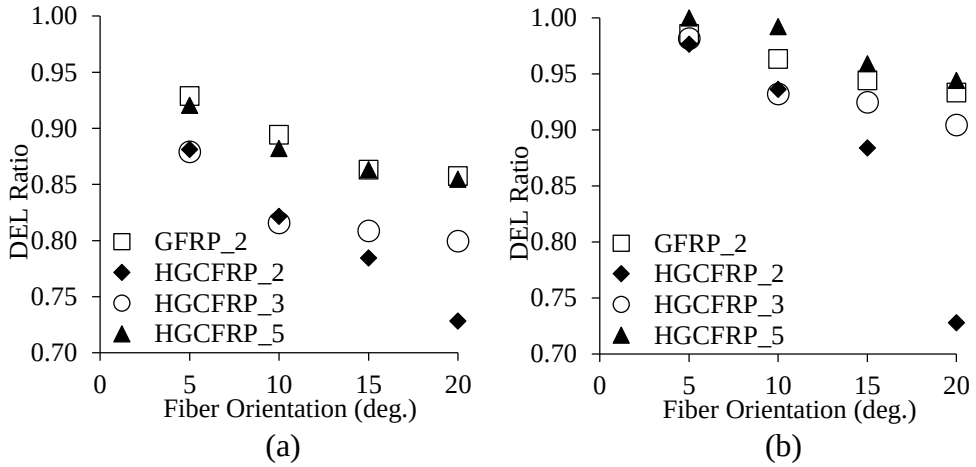

Figure 5.27 Variation of the ratio of fatigue damage equivalent (a) axial force in the main bearing 1 (b) shear force in main bearing 2 with the fiber angle for the wind turbine models with bend-twist coupled blades

Continuous yawing motion for the orientation of the wind turbine rotor towards to the direction of wind may result in failure in the yaw system whether it is passive or active. Utilizing bend-twist coupling effect due to the anisotropic behavior of composite materials may help to reduce damage equivalent loads at the yaw drive-bedplate

connection point of wind turbine systems. Figure 5.28 illustrates the variation of the ratio of the damage equivalent yawing moment and the axial force at the yaw drive-bedplate connection monitor point of wind turbine models with bend-twist blades with respect to the wind turbine with the baseline blade GFRP_1 with the fiber angle. The location of this connection point is illustrated in Figure 5.14. In Figure 5.28 it is seen that, designed bend-twist coupled blades contribute to reducing damage equivalent yawing moment at the yaw drive-bedplate connection monitor point up to 5%, except for the HGCFRP_2 blade, which approximately reduces the damage equivalent moment by 10% for fiber angles of 15° and 20°. Moreover, for the wind turbine configurations with HGCFRP_2 and HGCFRP_3 blades with fiber angles of 15° and 20°, it is possible to achieve more than 15% reduction for the axial force at the monitor point which has been investigated. These reductions may result in longer yaw drive mechanism life.

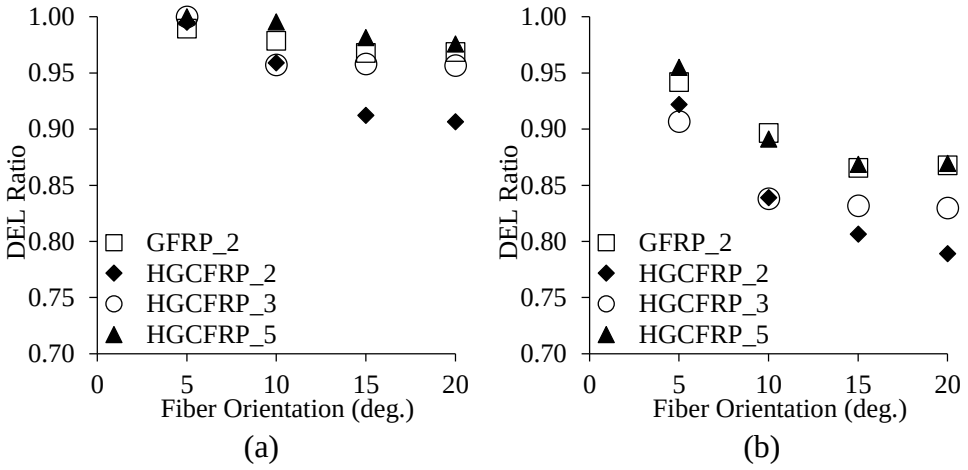

Figure 5.28 Variation of the ratio of fatigue damage equivalent (a) yawing moment and (b) axial force at the yaw drive-bedplate connection with the fiber angle for wind turbine models with bend-twist coupled blades

Results show that higher reductions in fatigue damage equivalent loads are obtained at the monitor points as the fiber angle of the spar cap region increases. Moreover, utilizing hybrid GFRP-CFRP off-axis spar cap plies in the blades provides more reduction at these monitor points compared to wind turbine system with full-GFRP

bend-twist coupled blade GFRP_2. Hybrid GFRP-HGCFRP blade HGCFRP_2 stands out among the four designed bend-twist blades as there are considerable load reductions at blade root, shaft-gearbox connection, main bearing, shaft, and yaw drive-bedplate connection.

5.2.2 Effect of Fiber Angle of Bend-Twist Coupled Blades on the Electrical Power Produced

Although high reductions in damage equivalent loads occur at several monitor points in the wind turbine system, keeping the electrical power produced same as the baseline wind turbine is essential. Figure 5.29 shows the variation of the mean electrical power production ratio of wind turbine systems with coupled blades with respect to the turbine system with uncoupled blade modeled in SWT with the fiber angle for the mean wind speed of 15 m/s. Mean electrical power produced is calculated for 10-minute simulation time and as the average of 6 different power results corresponding to 6 normal turbulence wind definitions.

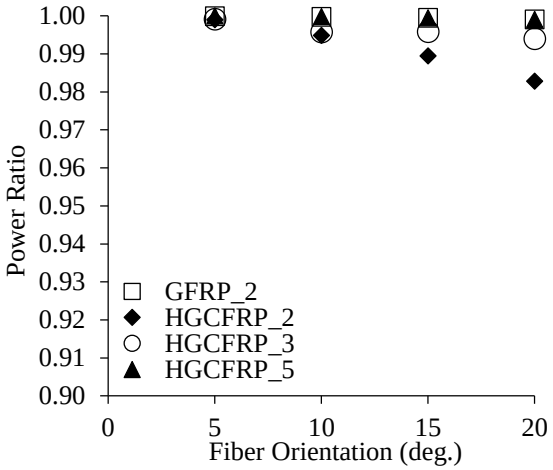

Figure 5.29 Variation of the ratio of mean electrical power produced by the wind turbines with bend-twist coupled blades with the fiber angle

As higher reductions in loads are achieved with the increase in the fiber angle, the mean electrical power produced by the wind turbine systems do not divert much from

the desired electrical power output which is 5 MW. This is because the controller of the turbine system controls the pitch angle in such a way that the electrical power produced is kept at 5 MW. For the wind turbine system with full-GFRP bend-twist coupled blade GFRP_2, reductions in damage equivalent loads occur whilst maintaining the electrical power at 5 MW, with almost no loss of electrical power. For the wind turbine systems with hybrid GFRP-CFRP bend-twist coupled blades HGCFRP_2 and HGCFRP_3, only 1.7% and 0.6% loss of electrical power for the 20º fiber angle eventuate when compared to the reference wind turbine system, respectively. Figure 5.30 illustrates the comparison of the mean electrical power produced by the wind turbine systems with complete GFRP bend-twist coupled blade GFRP_2 and hybrid CFRP-GFRP bend-twist coupled blade HGCFRP_3 for the fiber angle of 15º with respect to the wind turbine with the baseline blade.

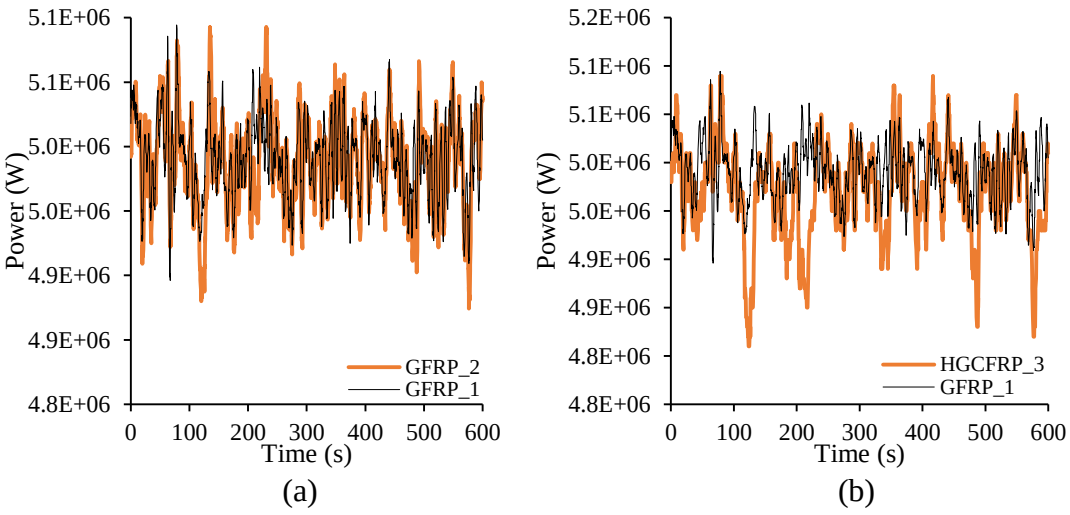

Figure 5.30 Comparison of the mean electrical power produced by wind turbines with bend-twist coupled blades (a) GFRP_2 and (b) HGCFRP_3 with the reference turbine

The mean electrical power is calculated by the average power output of the turbine systems at each time step subjected to 6 different turbulent wind profiles using the time responses extracted from SWT. As it can be seen from Figure 5.30, throughout the time history, electrical power produced by both turbine systems match up with each

other except for the sudden drops of electrical power produced by the wind turbine systems with coupled blades, especially for HGCFRP_3 blade, which cause slightly less mean electrical power production.

Table 5.11 presents the average power outputs of wind turbine systems with the reference and bend-twist coupled blades that underwent 6 different turbulent wind profiles with 600-second aeroelastic analyses performed in SWT.

Table 5.11 Average power generations of wind turbine systems

Fiber Orientation Angle	**Power generation of wind turbine systems with blade configuration (W)**				
	GFRP_1	**GFRP_2**	**HGCFRP_2**	**HGCFRP_3**	**HGCFRP_5**
5	4.991E+06	4.991E+06	4.986E+06	4.987E+06	4.991E+06
10	4.991E+06	4.990E+06	4.965E+06	4.970E+06	4.990E+06
15	4.991E+06	4.989E+06	4.939E+06	4.970E+06	4.989E+06
20	4.991E+06	4.987E+06	4.905E+06	4.961E+06	4.987E+06

In order to have a deeper understanding on the power drops occur in the coupled blades, time history of blade pitch angles of coupled GFRP_2 and hybrid coupled HGCFRP_3 with fiber orientation angle of 15° are plotted with respect to the reference blade in Figure 5.31 for wind profile Seed 1 (*Figure 5.17*). The mean pitch angles of HGCFRP_2, GFRP_2, and the baseline blade GFRP_1 are calculated from 600-second SWT analyses to be 5.85°, 6.60°, and 7.69°, respectively. The effective angle of attack of coupled blades reduce due to the bend-twist coupling that lessens the aerodynamic torque caused by the drop in lift. For the wind turbines with bend-twist coupled blades, the blade pitch angle is decreased by the controller with the purpose of increasing the effective angle of attack to provide required torque by sustaining rated rotor speed to achieve 5 MW of power production. Since the hybrid coupled HGCFRP_2 blade has greater bend-twist coupling due to CFRP material utilization in the flange regions, the mean pitch angle reduces more than GFRP_2 blade. Despite of the fact that pitch angle is decreased in order to increase the effective angle of attack, bend-twist coupling usage overrules this reduction by reducing effective angle of attack, resulting in alleviation in the fatigue damage equivalent loads.

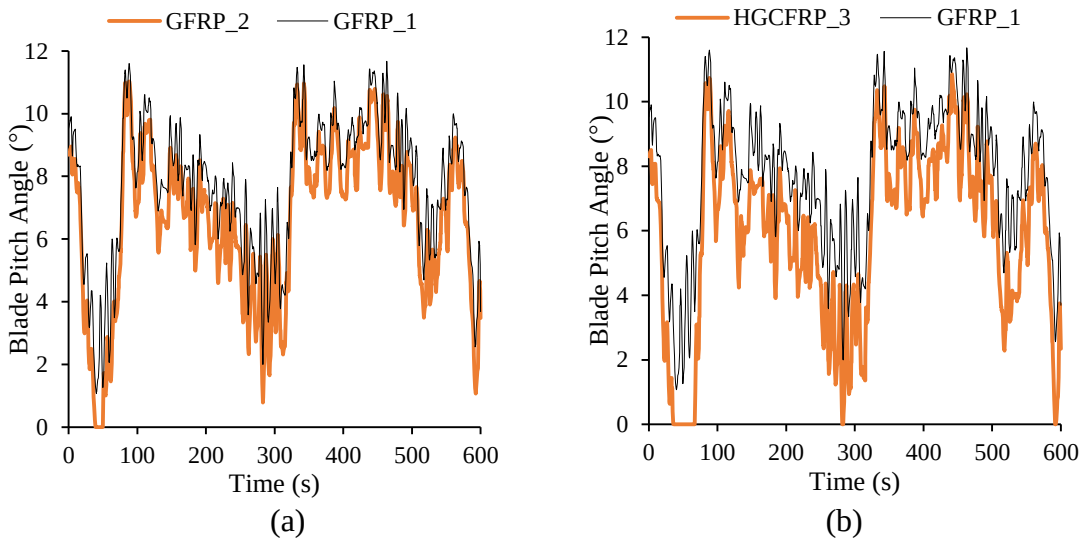

Figure 5.31 Comparison of blade pitch angles of bend-twist coupled blades (a) GFRP_2 and (b) HGCFRP_3 with the reference (GFRP_1) blade

5.2.3 Effect of Fiber Angle of Bend-Twist Coupled Blades on the Tower-Blade Tip Gap

The tower clearance of wind turbine systems with designed bend-twist coupled blades presented in Table 5.3 needed to be tested to avoid tower-blade crash. As previously mentioned, flapwise bending stiffness of designed bend-twist coupled blades, except HGFCRP_5, are all lower than the reference blade due to the off-axis ply placements. Therefore, for blades with lower flapwise stiffness are anticipated to have higher flapwise deflections. 10-minute transient aeroelastic analyses are performed in SWT and blade tip displacements throughout the analyses are extracted. Figure 5.32 shows the tip displacements of the reference blade, GFRP_2 and HGCFRP_3 coupled blades with fiber angle orientation of 15° for wind profile generated by Seed 1 (*Figure 5.17*). From the time history of the displacements, highest displacement value is taken as the maximum value for the specific fiber orientation under the specific wind profile.

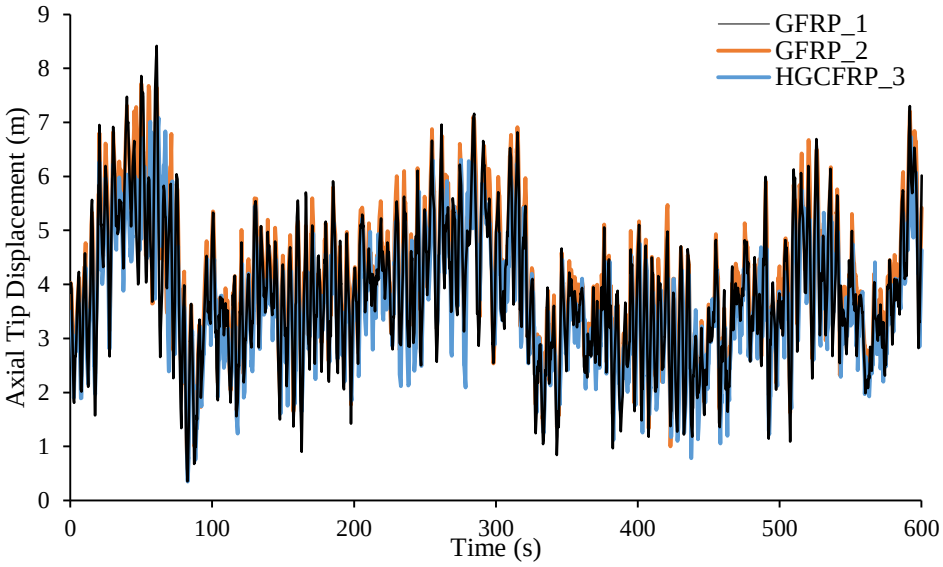

Figure 5.32 Time history of tip displacement of the reference blade and coupled blades of GFRP_2 and HGCFRP_3 with 15° fiber angle configuration

Maximum blade tip displacements of the designed blade configurations are presented in Table 5.12. For the wind turbine configuration with the baseline blade GFRP_1, maximum blade end displacement is calculated to be 8.42 meters. Therefore, except for the GFRP_2 and HGCFRP_2 blades with 20° fiber angle, maximum blade end displacements calculated by SWT are consistently lower than the maximum blade end displacement of the baseline blade. The reason for lower blade end displacement is the reduction in the lift due to bend-twist coupling. Despite of the fact that coupled blades have lower flapwise stiffness, reduction of aerodynamic loads due to the bend-twist coupling is accounted for lower tip displacements. Another important outcome of this study is that, although GFRP_2 and HGCFRP_3 have very close flapwise stiffness values, HGCFRP_3 blade has higher tower clearance as a result of higher reduction of lift force. This outcome also validates the reduction in damage equivalent loads at the blade root presented in Table 5.7-Table 5.10.

Table 5.12 Blade tip displacements

Fiber Angle (deg.)	Maximum Blade Tip Displacement (m)			
	GFRP_2	HGCFRP_2	HGCFRP_3	HGCFRP_5
5	7.96	7.00	6.65	6.67
10	7.93	6.92	6.90	6.77
15	7.72	7.80	7.08	6.91
20	8.46	9.15	7.67	7.76

5.2.4 Effect of Fiber Angle of Bend-Twist Coupled Blades on the Stresses in the Blade

For the evaluation of structural performance of wind turbine systems with bend-twist coupled blades, maximum stresses in the blades at selected time intervals during the transient aeroelastic analyses are indispensable. The stress computation in SWT is accomplished by the superelement restitution which makes it possible to compute the ply stresses in the original 3D finite element model which is associated to the degrees of freedom of the superelement blade. It should be emphasized that if the blade is integrated into the transient aeroelastic analysis as superelement blade, the full FEM solution can be obtained by superelement restitution process at the selected time steps of the transient analysis in SWT.

In order to compare the sole effect of the fiber angle on the maximum stresses in the blades at the selected times, maximum stresses in the baseline blade GFRP_1 and complete GFRP bend-twist coupled blade GFRP_2 having 15^{o} fiber angle are compared. Although coupled blades have the same layup configuration, hybrid coupled blades have lower weights and the location of critical section in terms of stress is also related to the weight of the blade. Since the only modification performed on GFRP_2 blade is the rotation of the unidirectional laminae in the flange area, the absolute effect of the bend-twist coupling can be observed by comparing the maximum stresses in GFRP_1 and GFRP_2 blades. Figure 5.33 shows the local crest in the flapwise bending moment at the root sections of GFRP_1 and GFRP_2 blades. The

stresses are computed on the full FEM model through the s7uperelement restitution process at the times 185.14 seconds and 185.23 seconds, which correspond to local maxima of the flapwise bending moments at the root section of GFRP_1 and GFRP_2 blades, respectively.

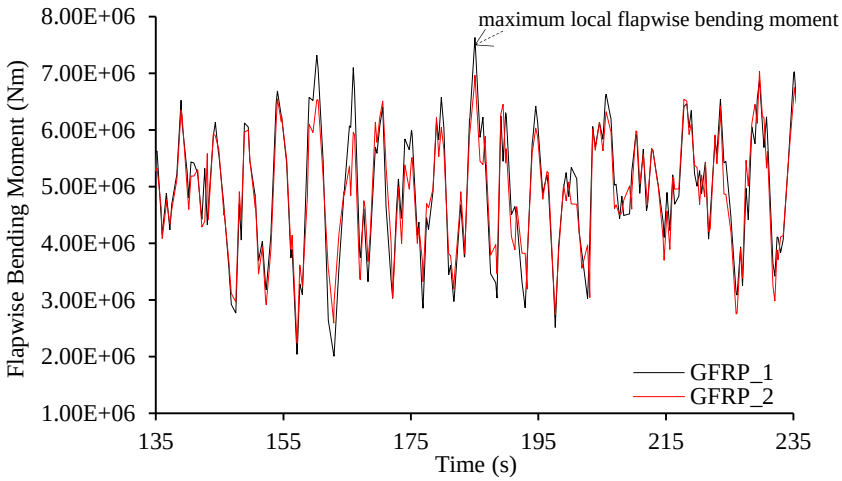

Figure 5.33 Variation of the flapwise bending moment at the blade root for the GFRP_1 and the GFRP_2 blades

Figure 5.34 visualizes the maximum fiber direction stresses of the baseline blade GFRP_1 and the complete GFRP bend-twist coupled blade GFRP_2. As it is seen in the figure, the maximum fiber direction stress occurs at the junction of the transition region with the DU40 airfoil, at about 8.2 meters from the blade root for both blades. Figure 5.34 portrays that there is about 9.7% reduction in the maximum fiber direction stress in the full GFRP bend-twist coupled blade GFRP_2 compared to the baseline blade GFRP_1. The reason for such a decrease in the maximum fiber direction stress is the reduction of the lift in bend-twist coupled blade GFRP_2 due to due to the coupling of bending and twisting deformations.

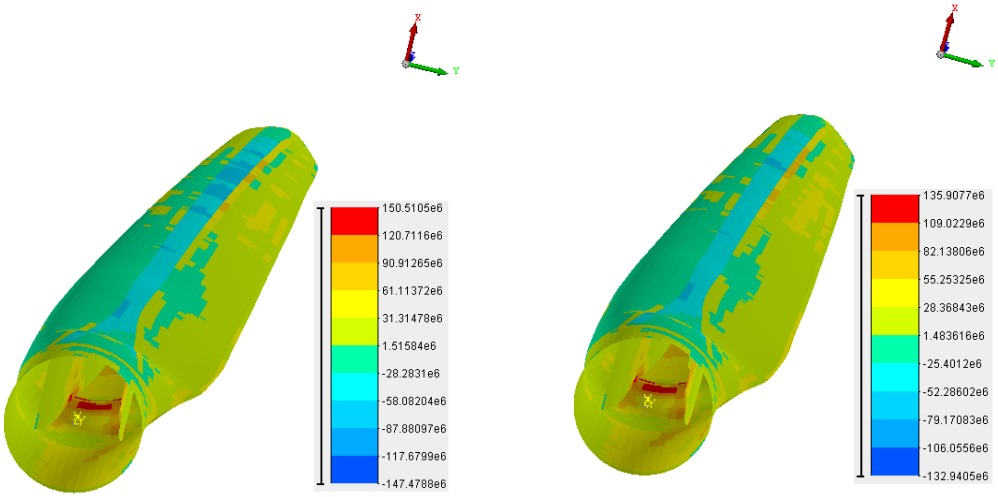

(a) Blade configuration GFRP_1 (baseline blade) **(b)** Blade configuration GFRP_2 (15º spar cap plies)

Figure 5.34 Comparison of fiber direction stresses in the upper faces of the elements of complete GFRP baseline blade GFRP_1 and the bend-twist coupled blade GFRP_2 blade (Pa)

Table 5.13 shows the maximum fiber direction, transverse normal and in-plane shear stresses in the reference and the coupled blade GFRP_2. There are significant mitigations in the stress components with the usage of bend-twist coupling. Furthermore, maximum stress components tend to reduce as the fiber angle orientation (φ) increases from 5° to 20°.

Table 5.13 Maximum stress components in the reference blade and coupled GFRP_2 blade

Blades	**Maximum Stress Components in the Blades**		
	Fiber Direction Stress (MPa)	**Transverse Normal Stress (MPa)**	**In-Plane Shear Stress (MPa)**
GFRP_1	150.51	62.45	37.76
GFRP_2, φ=5°	138.60	60.34	36.57
GFRP_2, φ=10°	136.58	59.71	36.44
GFRP_2, φ=15°	135.91	59.34	36.30
GFRP_2, φ=20°	134.22	58.83	36.06

In order to investigate the sole effect of the fiber angle on the stresses in the hybrid GFRP-CFRP bend-twist coupled blades, the stress comparison is made between hybrid GFRP-CFRP blades HGCFRP_3 having 5° and 10° fiber angles. Figure 5.35 illustrates the maximum fiber direction stresses of hybrid GFRP-CFRP bend-twist coupled blades HGCFRP_3 computed at 184.93 seconds and 185.73 seconds. The times at which superelement restitutions are processed correspond to local maxima of flapwise bending moments at the root sections of the blades. As the figure suggests, there is approximately 10.7% reduction in the maximum stress in the hybrid GFRP-CFRP bend-twist coupled blade HGCFRP_3 with 10° spar cap fiber angle configuration when compared to that of 5^o spar cap fiber angle configuration. For both blades, the maximum fiber direction stress occurs in the CFRP material at the junction of the inboard unidirectional GFRP spar cap section and the start of the off-axis CFRP spar cap region on the lower surface of the blade in the CFRP material, at about 31.5 meters from the blade root. It is seen that for the hybrid GFRP-CFRP blades with complete CFRP material in the spar caps of the bend-twist sections, maximum stress does not occur at the junction of the transition region and the DU40 airfoil near the blade root, but rather it occurs at the junction of the on-axis GFRP and the off-axis CFRP spar cap plies. This is expected, because CFRP material is much stiffer than the GFRP material and moreover, in order to match the flapwise bending stiffness of the bend-twist coupled blade HGCFRP_3 with the full GFRP bend-twist coupled blade GFRP_2, the number of CFRP plies is significantly less than GFRP plies in the spar caps of the bend-twist sections of the blade. Therefore, shell thickness of HGCFRP_3 is less than GFRP_2 in the bend-twist coupled sections of the blade. Stresses calculated for the hybrid GFRP-CFRP blade HGCFRP_3 for two different fiber angles shows that for higher fiber angle the maximum fiber direction stress reduces when the fiber angle increases. The same conclusion is also valid for the transverse normal stress and in-plane shear stress. The reduction in the load level due to the bending-twisting coupling also account for lower stress levels in the bend-twist coupled blades.

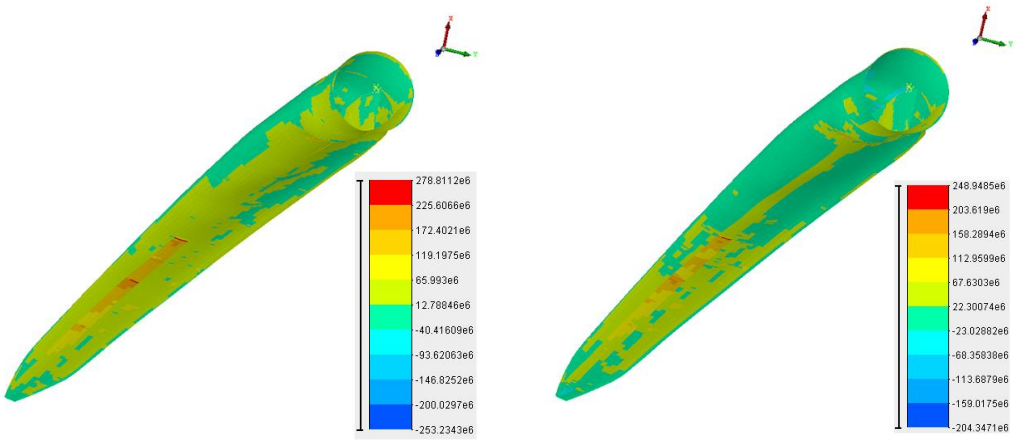

(a) Blade configuration HGCFRP_3 (5º spar cap plies) **(b)** Blade configuration HGCFRP_3 (10º spar cap plies)

Figure 5.35 Comparison of fiber direction stresses in upper faces of elements of bend-twist coupled blades HGCFRP_3 (Pa)

Figure 5.36 exemplifies the comparison of maximum fiber direction stresses for HGCFRP_2, HGCFRP_3, and HGCFRP_5 blades with 10º fiber angle. The back transformations to full FEM solutions are computed at 186.53 seconds, 185.73 seconds, and 185.13 seconds, which correspond to local maxima of flapwise bending moments at the root section of blade configurations HGCFRP_2, HGCFRP_3, and HGCFRP_5, respectively. For all three blades, maximum fiber direction stresses occur on the lower surface of the blades. Hybrid GFRP-CFRP blade HGCFRP_5 stands out among the three blades since the lowest maximum fiber direction stress occurs in HGCFRP_5. As in full-GFRP blades, the highest fiber direction stress arises at the confluence of the transition region with the DU40 airfoil, at about 8.2 meters from the blade root for the HGCFRP_5 blade. Due to the utilization of combination of CFRP and GFRP plies in the bend-twist coupled sections of the blade, fiber direction stress is approximately 45% less at the critical sections of HGCFRP_5 when compared to HGCFRP_2 and HGCFRP_3 blades with the same fiber angle configuration. On the other hand, the difference in maximum stresses in HGCFRP_2 and HGCFRP_3 is nearly same. From Figure 5.36, it is seen that in the hybrid GFRP-CFRP bend-twist coupled blades HGCFRP_2 and HGCFRP_3 with complete CFRP plies in the bend-twist sections of the blade, maximum stress occurs at the junction of the inboard

unidirectional GFRP spar cap section and the start of the CFRP bend-twist coupled sections of the blade.

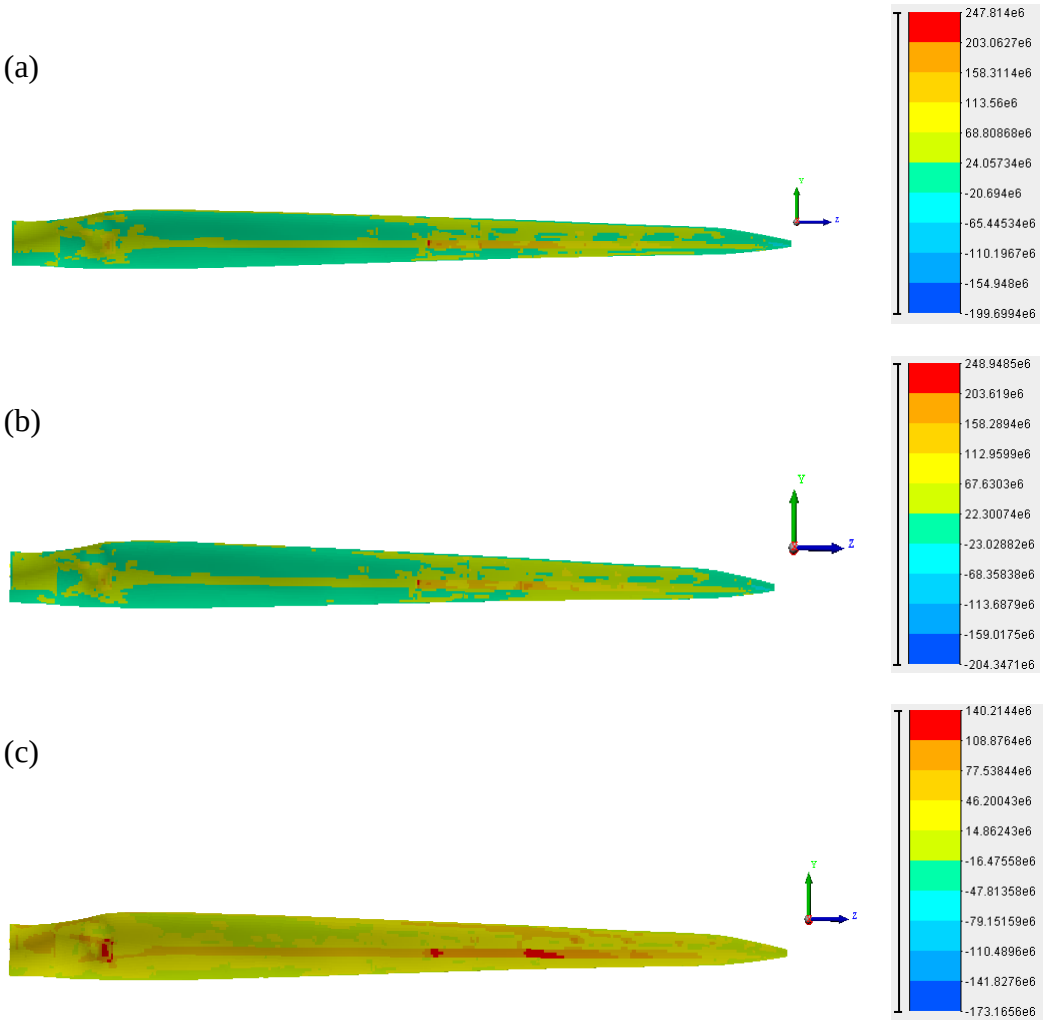

Figure 5.36 Comparison of fiber direction stresses in the upper faces of the elements of (a) HGCFRP_2 (b) HGCFRP_3 and, (c) HGCFRP_5 blades (Pa) (lower surface of blades)

Table 5.14 presents the strength properties of GFRP and CFRP materials used in the blade designs. For all designed bend-twist coupled blades with varying fiber angles examined in this context, maximum fiber direction stresses are notably lower than ultimate strength values presented in Table 5.14. The only parameter that varies is the

magnitude of margin of safety for designed blade configurations which is still high enough for all blade configurations to operate safely.

Table 5.14 Strength properties of GFRP and CFRP materials

Material	Ult. Tensile Strength 0° (MPa)	Ult. Compressive Strength 0° (MPa)	Ult. Tensile Strength 90° (MPa)	Ult. Comp. Strength 90° (MPa)	Ult. In-Plane Shear Strength (MPa)
GFRP	866	647	54	150	75
CFRP	1800	1200	60	200	90

With the utilization of the bend-twist coupling with off-axis unidirectional laminae placement, damage equivalent load reductions are obtained not only at the blade root, but also in the several subcomponents of the wind turbine system for the decided fiber angle orientation. Present study also showed that the reductions occur in fatigue damage equivalent loads in the bearings in which most of the failures happen. Different from the most of the work in literature, in this study load alleviation on the whole wind turbine system is examined. It is also presented that if CFRP material is used the flange area higher load alleviation is achieved in the monitor points, as in the turbine systems with HGCFRP_2 and HGCFRP_3 blade. With the increasing fiber angle orientation, DEL reductions reach up to 20%. Although the flapwise stiffness of GFRP_2 blade is lower than that of GFRP_1 blade, noticeable mitigations in DEL occur with sufficient tower-blade tip gap. Consequently, HGCFPRP_2 and GFRP_2 blades are selected as the better designs when compared to other designed blades in terms of load mitigation.

Besides the load mitigation, the wind turbine systems produce power with almost no loss while the blades preserve sufficient tower clearance with reduced maximum stress components. The losses of power in the wind turbine systems with HGCFRP_2 blade with 15° and 20° fiber angle configuration are only 1% and 1.7%. Another important outcome of this work is that bend-twist coupled blades have higher tower clearances and lower maximum stress components. Therefore, it can be concluded that utilization of bend-twist coupling on the wind turbine blades present no drawbacks.

CHAPTER 6

CONCLUSION

Wind energy is a vastly demanded source among renewable energies. Wind turbines are getting larger for the past ten years to capture more energy from the wind. Increasing the size of the turbines has resulted in the price reduction for the electricity per kWh; nonetheless, it has also created problems associated with the length of the blades. The new wind turbine blade designs have reached to 100 meter border. Increase in length and more sophisticated control mechanisms increase the weight of the blades that require inventive design solutions to alleviate loads. Utilization of bend-twist coupling in the blades due to the anisotropic behavior of composite materials is a preferable approach to lessen the loads in the wind turbine system. In this thesis, the effect of bend-twist coupling with the employment of GFRP and CFRP materials in the spar cap regions of the blades with different fiber angles and configurations is examined both theoretically and experimentally. Validation of the bend-twist coupling effect is performed with experiments and finite element analyses performed for composite plates and box-beams which simulate the flange regions between the shear webs in wind turbine blades .With the usage of bend-twist coupling, load reduction at several critical locations in the wind turbine system is aimed.

In this work, experimental study is based on the evaluation of bend-twist coupling effect on composite plates and box-beam structures which show resemblance to the flange regions between the spars of wind turbine blades via Digital Image Correlation (DIC) system, and making comparisons with finite element analyses. Bend-twist coupling potentials determined from the measurements performed by the DIC system

and finite element analyses are compared and combined for the purpose of crafting a dependable database for the effect of material and fiber angle orientation on the bend-twist coupling potential. Moreover, material tests are performed through following several test standards in order to determine GFRP and CFRP material properties correctly to be readily used in the finite element analyses for the validation of the experiments conducted with the DIC system. The material tests are conducted with utilization of strain gages and the DIC system with at least 5 specimens for each orthotropic property for the GFRP and the CFRP materials. It is shown that usage of the DIC system for strain calculations while performing tensile tests does not have any drawback; quite the opposite, it eliminates the necessity of strain gage application. It is concluded that for the calculation of the strain by the DIC system to be used in the evaluation of the elastic moduli, it is necessary to average the strains on the whole measurement area to eliminate the wiggles occurring in the calculated strains. It should be noted that the DIC system measures the displacement field and strains are then calculated by processing of the measured displacements. Depending on the quality of the speckle pattern generated on the measuring area slight measurement errors in the displacement field result in higher differences in the calculated strains in the neighboring points in a region of the measuring area. Therefore, wiggles occur in the calculated strain over the measuring area. However, if strains are averaged in the whole measuring area, then the resulting average strain represents the actual strain to be used for the elastic moduli calculations accurately. This conclusion has been arrived at after processing the DIC measurements differently and performing comparisons with the strain gage readings.

With the intention of elimination of discrepancies in material properties such as fiber-volume fraction unpredictability, thickness variations occurring in composite plates, different compression and tension elastic properties, a MATLAB script is written to obtain improved orthotropic GFRP and CFRP material properties to be used in finite element analyses. Bend-twist coupling database obtained through experiments and finite element analyses of the composite plates and box-beams, using the improved material properties obtained via the iterative optimization process, are assessed

qualitatively rather than quantitatively; that is to say, percent of relative differences of the bend-twist coupling potentials obtained from the DIC tests and finite element analyses are compared. Bending twisting coupling potentials of GFRP and CFRP plates and box beams determined by DIC experiments and finite element analyses have good agreement except for the hybrid GFRP and CFRP box beams. One of the reason for the differences in the outcomes of finite element analyses and DIC experiments for the hybrid GFRP and CFRP box beams is the local fiber angle alteration mainly due to vacuum infusion process and manufacturing flaws. Moreover, since the CFRP material has thicker fibers, the thickness variation along the upper and lower flange regions in box beams differ significantly. Another reason for such a discrepancy occurs is that tensile elastic moduli are used in finite element analyses. However, for composite materials, tensile and elastic properties can be significantly different and certain parts of the box-beams are exposed to compressive loads. Besides, because of the fiber-volume fraction unpredictability, effective thickness values used in finite element model can be inaccurate.

Based on the results of bending twisting tests and analyses performed for composite plates and box beams, it is concluded that CFRP material has greater bend-twist coupling potential when compared to the GFRP material. Acquired information of the effect of bend-twist coupling with different materials and different fiber orientations from experiments and finite element analyses by utilizing composite plates and box-beam structures forms a basis for designing bend-twist coupled wind turbine blades with the purpose of load reduction in the whole wind turbine system and lessening the maximum stress in the blades whilst keeping the power production at 5 MW with sufficient blade clearance. The outcome of the experimental and numerical study provided information on how the bend-twist coupling potential of different composite materials, such as E-Glass and Carbon composites, vary with the off axis fiber angle. Based on this study, off-axis fiber angle range to be used in the bend-twist coupled blade designs is decided. Experimental and finite element results on the bending-twisting coupling potential of GFRP plates and box beams revealed that for the GFRP material, bending-twisting coupling increases up to approximately 25^{o} fiber orientation

angle and reduces afterwards. For the CFRP plates and box beams, bending-twisting coupling increases up to approximately 15^{o} fiber orientation angle and reduces afterwards. Based on this outcome, in the bend-twist coupled wind turbine blades off-axis fiber angle range is decided to be 5^{o}-20^{o}. Experimental and numerical study on the evaluation of bending twisting coupling potential of GFRP and CFRP plates and box-beams allowed the determination of the off-axis fiber angles to implement in the bend-twist coupled blades in the wind turbine system for load alleviation purposes utilizing the concept of bending twisting coupling of composite blades.

For the investigation of the effect of bend-twist coupling on the load alleviation in the wind turbine system, transient flexible multi-body aeroelastic analyses of the wind turbine system are conducted in Samcef Wind Turbines (SWT) for different designed blades utilizing the real working scenarios and wind conditions that exist in the wind turbine design standard IEC 61400-1. Five designed bend-twist coupled blades are used in the wind turbine models generated in SWT. Transient aeroelastic analyses are performed for the power production case with six different wind profiles which have 15 m/s mean speed and with the baseline and the designed bend-twist coupled blades having four different fiber orientation angles. Damage equivalent loads are calculated for each wind turbine model with the designed bend-twist coupled blade for 600-second transient aeroelastic analyses. The calculations are made by averaging the results obtained from the analyses to meet IEC 61400-1 standard. Higher reductions in critical monitor points in the wind turbine system are achieved with the exploitation of off-axis CFRP plies in the spar caps with higher fiber angles compared to full-GFRP blades.

Despite of the fact that considerable declinations in damage equivalent load levels are accomplished with the introduction of off-axis spar cap plies on the blades of wind turbine systems, the mean power production of the wind turbine systems under six turbulence wind profiles are preserved at about 5 MW for the slightly over rated wind speed of 15 m/s. With increasing fiber angle, power generation of the turbine systems with designed blades lessen marginally. The reduction in power generation may be minimized with the selection of suitable bend-twist coupled blade configuration. It is

concluded that the designed bend-twist coupled blades with low off-axis fiber angles must be chosen so as to minimize the slight power loss. Moreover, sufficient tower clearance is provided by all wind turbine configurations with the bend-twist coupled blades except for the blade with 20° off-axis fiber angle and pose no problem in terms of tower-blade crash. As a demonstration of the stress recovery procedure, superelement restitution process is used for the determination of maximum ply stresses at the selected time steps in SWT. For the selected time steps, the highest stress in the GFRP bend-twist coupled blade occur at the junction of the transition region with the DU40 airfoil near the blade root and noticeably lower than the baseline blade. Another remark that can be made in this work is that maximum stress in the bend-twist coupled blades reduces with the increasing fiber angle; even though flapwise bending stiffness decreases. For hybrid bend-twist coupled blades, the maximum stress occurs at the junction of on-axis GFRP and off-axis CFRP plies at the beginning of bend-twist coupled region.

Present study envisages the bend-twist coupling potential of GFRP and CFRP materials through experiments and finite element analyses and the application of it on the wind turbine blades. Damage equivalent loads at several critical points, power production, tower clearance, and maximum stresses in the blades due to bend-twist coupling utilization are investigated.

In the future, in order to fully simulate the wind turbine operations under real working scenarios under-, over-, and rated wind profiles may be imposed. Reductions in damage equivalent loads and more importantly, power generation for underrated, rated, and overrated average hub height wind speeds for wind turbines with bend-twist coupled blades can be investigated. Additionally, optimum fiber angle and ply configuration at the bend-twist coupled sections of the blades, and the region of the bend-twist coupled sections along the blade span may be determined in order to maximize the efficiency of bend-twist coupling potential whilst keeping the power production as much as the baseline turbine configuration. It is shown that damage equivalent loads decrease with the increasing fiber angle. Nonetheless, especially for wind turbines with hybrid bend-twist coupled blades, power production reduces to

some extent as the fiber angle increases. Therefore, an optimum fiber angle can be implemented in the bend-twist coupled section of the blade to reduce damage equivalent loads whilst keeping the electrical power generation as high as possible. In addition, in the present study bend-twist coupling is implemented in the last 30 m of the wind turbine blade. The region of the bend-twist coupled section along the blade span can also be optimized for maximum load reduction at no power loss with respect to the baseline blade. Besides the fiber angle optimization, controller and sectional pretwist angle optimization may be studied to achieve reduction in damage equivalent loads and stresses in the blades while decreasing the power losses associated with the use of bending twisting coupling in wind turbine blades.

REFERENCES

[1] America's Climate Choices: Panel on Advancing the Science of Climate Change; National Research Council, Washington, D.C.: The National Academies Press, 2010.

[2] O. Ellabban, H. Abu-Rub and F. Blaabjerg, "Renewable energy resources: Current status, future prospects and their enabling technology," *Renewable and Sustainable Energy Reviews,* vol. 39, pp. 748-764, 2014.

[3] A. Brown, S. Müller and Z. Dobrotkova, "Renewable Energy: Markets and Prospects by Technology," International Energy Agency Information Paper, 2011.

[4] "Re-Thinking 2050: A 100% Renewable Energy Vision for the European Union," European Renewable Energy Council, 2010. [Online]. Available: www.erec.org. [Accessed 18 July 2016].

[5] "Global Cumulative Installed Wind Capacity," Global Wind Energy Council, 2015. [Online]. Available: http://www.gwec.net/global-figures/graphs/. [Accessed 18 July 2016].

[6] P. Purohit and A. Michaelowa, "Potential of wind power projects under the Clean Development Mechanism in India," *Carbon Balance and Management*, vol. 2:8, 2007.

[7] "Wind Energy Systems: Main Components of a Wind Turbine," Iowa Energy Center, [Online]. Available: http://www.iowaenergycenter.org/wind-energy-manual/wind-energy-systems/. [Accessed 20 July 2016].

[8] N. Karaolis, G. Jeronimidis and P. Mussgrove, "Active and Passive Aerodynamic Power Control Using Asymmetric Fibre Reinforced Laminates for Wind Turbine Blades," in *Proceedings 10th British Wind Energy Conference*, London, 1988.

[9] W. C. de Goeij, M. J. L. van Tooren and A. Beukers, "Implementation of bending-torsion coupling in the design of a wind-turbine rotor-blade," *Applied Energy,* vol. 63, no. 3, pp. 191-207, 1999.

[10] H. J. T. Kooijman, "Bending-Torsion Coupling of a Wind Turbine Rotor Blade," Netherlands Energy Research Foundation (ECN), 1996.

[11] D. W. Lobitz and P. S. Veers, "Load Mitigation with Bending/Twist-coupled Blades on Rotors Using Modern Control Strategies," *Wind Energy*, vol. 6, no. 2, pp. 105-117, 2003.

[12] J. Locke and U. Valencia, "Design Studies for Twist-Coupled Wind Turbine Blades," Sandia National Laboratories, Kansas, 2004.

[13] H. J. Lin and W. M. Lai, "A Study of Elastic Coupling to the Wind Turbine Blade by Combined Analytical and Finite Element Beam Model," *Journal of Composite Materials*, vol. 44(23), pp. 2643-2665, 2010.

[14] X. Zhou, L. An and Z. Wang, "Twist-Bend Coupling Analysis for 5MW Wind Turbine Blades," *Applied Mechanics and Materials*, Vols. 152-154, pp. 703-708, 2012.

[15] J. Jonkman, S. Butterfield, W. Musial and G. Scott, "Definition of a 5-MW Reference Wind Turbine for Offshore System Development," National Renewable Energy Laboratory, Colorado, 2009.

[16] M. Luczak, S. Manzato, B. Peeters, K. Branner, P. Berring and M. Kahsin, "Dynamic Investigation of Twist-Bend Coupling in a Wind Turbine Blade," *Journal of Theoretical and Applied Mechanics*, vol. 49(3), pp. 765-789, 2011.

[17] M. Capellaro, "Design Limits of Bend Twist Coupled Wind Turbine Blades," in *53rd AIAA/ASME/ASCE/AHS/ASC Structures, Structural Dynamics and Materials Conference, AIAA 2012-1501*, Honolulu, Hawaii, 2012.

[18] A. Thomas D., "Passive Load Control for Large Wind Turbines," in *51st AIAA/ASME/ASCE/AHS/ASC Structures, Structural Dynamics & Materials Conference*, Orlando, FL, 2010.

[19] M. Gözcü, Investigation of the Effect of Bending Twisting Coupling on the Loads in Wind Turbines with Superelement Blade Definition, 2014.

[20] V. Fedorov and C. Berggreen, "Bend-twist coupling potential of wind turbine blades," in *Journal of Physics: Conference Series 524(1), 012035*, 2014.

[21] S. Aziz, J. Gale, A. Ebrahimpour and M. P. Schoen, "Passive Control of a Wind Turbine Blade Using Composite Material," in *Proceedings of the ASME 2011 International Mechanical Engineering Congress & Exposition* , Denver, CO, 2011.

[22] V. A. Fedorov, N. Dimitrov, C. Berggreen, S. Krenk and K. Branner, "Investigation of structural behaviour due to bend-twist couplings in wind turbine blades," in *Proceedings of the NAFEMS Nordic Seminar of Simulating Composite Materials and Structures, NAFEMS*, Esbjerg, Denmark, 2010.

[23] ARAMIS Metrology Systems, "ARAMIS Professional," GOM mbH, 2016. [Online]. Available: http://www.gom.com/3d-software/gom-system-software/aramis-professional.html. [Accessed 05 09 2016].

[24] "ASTM D3039/D3039M-14, Standard Test Method for Tensile Properties of Polymer Matrix Composite Materials," ASTM International, West Conshohocken, PA, 2014.

[25] DIN EN 6031, "DIN EN 6031, Determination of In-Plane Shear Properties (± 45° Tensile Test)," Deutsches Institut für Normung e. V., Berlin, 1996.

[26] "ASTM D3518/D3518M−13, Standard Test Method for In-Plane Shear Response of Polymer Matrix Composite Materials by Tensile Test of a ±45° Laminate," ASTM International, West Conshohocken, PA, 2013.

[27] IEC 61400-1 3rd Edition 2005, "Wind Turbines - Part 1: Design Requirements," International Electrotechnical Commission (IEC), Geneva, Switzerland, 2005.

[28] Samcef Wind Turbines (SWT) User Help V 6.2.3, Siemens Inc. , 2013, pp. 234-236.

[29] B. J. Jonkman and L. Kilcher, "TurbSim User's Guide: Version 1.06.00," National Renewable Energy Laboratory (NREL), 2012.

[30] "ARAMIS v6.3 User Manual - Software," GOM mbH, Braunschweig, Germany, 2011.

[31] B. Pan and L. Kai, "A fast digital image correlation method for deformation measurement," *Optics and Lasers in Engineering*, vol. 49, no. 7, pp. 841-847, 2011.

[32] "ARAMIS User Information - Hardware," GOM mbH, Braunschweig, Germany, 2011.

[33] *Biresin CH80 Product Data Sheet,* Bad Urach, Germany: Sika Deutschland, 2016.

[34] *UC200TFX Fabrics Catalogue,* Venice, Italy: G.Angeloni s.r.l..

[35] *Interglas 92145 Product Information,* Erbach, Germany: Interglass Technologies GmbH.

[36] J. E. Locke and I. Contreras, "The Implementation of Braided Composite Materials in the Design of a Bend-Twist Coupled Blade," Sandia National Laboratories, Albuquerque, NM, 2002.

[37] "High-Force Axial/Torsional Test Systems," MTS Systems Corporation, [Online]. Available: https://www.mts.com/en/products/producttype/test-systems/load-frames-multiaxial/axial-torsional/high-force/index.htm. [Accessed 16 February 2017].

[38] "Operating Manual MGCplus with AB22A/AB32," Hottinger Baldwin Messtechnik GmbH , Darmstadt, Germany.

[39] "SAMCEF Mecano User Manual," Siemens PLM, 2014. [Online]. Available: https://www.plm.automation.siemens.com/. [Accessed 21 04 2017].

[40] H. Chen and Y. Wenbin, "Manual of PreVABS," 2008. [Online]. Available: http://analyswift.com/wp-content/uploads/2012/10/PreVABS-Manual.pdf. [Accessed 29 04 2017].

[41] M. Gözcü, T. Farsadi, Ö. Şener and A. Kayran, "Assessment of the Effect of Hybrid GFRP-CFRP Usage in Wind Turbine Blades on the Reduction of Fatigue Damage Equivalent Loads in the Wind Turbine System," in *AIAA Science and Technology Forum and Exposition, AIAA SciTech 2015, 33rd Wind Energy Symposium*, Kissimmee, FL, 2015.

[42] Ö. Şener, T. Farsadi and A. Kayran, "Effect of Fiber Orientation of Bend-Twist Coupled Blades on the Structural Performance of the Wind Turbine System," in *35th Wind Energy Symposium, AIAA SciTech Forum (AIAA 2017-1167)*, Grapevine, TX, 2017.

[43] "Samcef Field v8.4," Siemens PLM Software, [Online]. Available: http://www.lmsintl.com/samcef-field. [Accessed 14 01 2017].

[44] D. Kammer and M. Baker, "Comparison of the Craig-Bampton and Residual Flexibility Methods of Substructure Representation," *Journal of Aircraft*, vol. 24, no. 4, pp. 262-267, 1986.

[45] P. Bonnet, "SWT V3.3-02 Stationary Aerodynamics Validation," LMS Samtech Iberica Wind Turbine Expertise Centre, Barcelona, 2013.

[46] "Bladed Technical Brochure," DNV GL, Arnhem, 2015.

[47] P. L'ecuyer, "Efficient and Portable Combined Random Number Generators," *Communications of the ACM,*, vol. 31, pp. 742-751, 1988.

[48] Heege, A., et al., "Fatigue Damage Computation of a Composite Material Blade using a "Mixed non-linear FEM and Super Element Approach"," in *EWEA 2011*, Brussels, Belgium, 2011.

[49] B. Nivedh, "Major Failures in the Wind Turbine Components and the Importance of Periodic Inspections," Ul India Pvt. Ltd, WindInsider, 2014.

[50] S. Sheng, "Wind Turbine Gearbox Reliability Database, Condition Monitoring, and Operation and Maintenance Research Update," NREL Drivetrain Reliability Collaborative Workshop, 2016.